REDUCING ROAD WEAR WHILE ENSURING COMFORT AND CHARGING

CONSTRAINTS FOR DYNAMICALLY CHARGED PASSENGER VEHICLES

THROUGH NOISE SHAPED CONTROL INPUTS

by

Clint Jay Ferrin

A thesis submitted in partial fulfillment
of the requirements for the degree

of

MASTER OF SCIENCE

in

Electrical Engineering

Approved:

_____   _____
Randy Christensen, Ph.D.   Donald Cripps, Ph.D.
Major Professor   Committee Member

_____   _____
Regan Zane, Ph.D.   Richard S. Inouye, Ph.D.
Committee Member   Vice Provost for Graduate Studies

UTAH STATE UNIVERSITY
Logan, Utah

2019

ABSTRACT

REDUCING ROAD WEAR WHILE ENSURING COMFORT AND CHARGING

CONSTRAINTS FOR DYNAMICALLY CHARGED PASSENGER VEHICLES

THROUGH NOISE SHAPED CONTROL INPUTS

by

Clint Jay Ferrin, Master of Science

Utah State University, 2019

Major Professor: Randy Christensen, Ph.D.
Department: Electrical and Computer Engineering

Dynamically charged vehicles suffer from power-loss during wireless power transfer due to receiver and transmitter coil misalignment while driving. Autonomous dynamically charged vehicles can maximize wireless power transfer by following an optimal charging path, but the repeated high-precision increases road wear. To avoid unnecessary road wear and rutting, a noise shaping filter is proposed that adds acceleration, velocity, and position variability to a vehicle's trajectory that complies with passenger acceleration and position constraints. However, introducing variability into an optimal charging path also risks depleting battery life prior to destination arrival. Therefore, a path planner is proposed that guarantees average charge within a specified probability and ensures rider comfort while reducing road wear.

(140 pages)

PUBLIC ABSTRACT

REDUCING ROAD WEAR WHILE ENSURING COMFORT AND CHARGING
CONSTRAINTS FOR DYNAMICALLY CHARGED PASSENGER VEHICLES
THROUGH NOISE SHAPED CONTROL INPUTS

Clint Jay Ferrin

Dynamically charged vehicles suffer from power-loss during wireless power transfer due
to vehicle coil misalignment while driving. Autonomous dynamically charged vehicles can
maximize wireless power transfer by following an optimal charging path, but the repeated
precision increases road wear. To avoid unnecessary road wear and rutting, a path planner
can intentionally inject variability into an autonomous vehicle's path. However, introduc-
ing variability into an optimal charging path risks depleting battery life prior to destination
arrival, and it increases rider discomfort. Therefore, a path planner is proposed that guar-
antees average charging criteria and ensures rider comfort while reducing road wear.

This work is dedicated my wife Dakota and my daughter Kali Jo
for their countless hours of support.

ACKNOWLEDGMENTS

CONTENTS

LIST OF TABLES

LIST OF FIGURES

ACRONYMS

ADCV   Autonomous Dynamically Charged Vehicles

CCPath   Continuous Curvature Path

DCV   Dynamically Charged Vehicle

EKF   Extended Kalman filter

EV   Electric Vehicle

GPS   Global Positioning System

LGPR   Localizing Ground Penetrating Radar

LQR   Linear–Quadratic Regulator

PSD   Power Spectral Density

RTK   Real Time Kinematic

SOC   State of Charge

WPT   Wireless Power Transfer

CHAPTER 1

INTRODUCTION

1.1 Background

Electric vehicles (EVs) account for more than 1% of yearly vehicle sales in the United States, and they are rising in popularity world-wide [1]. Dynamic wireless charging EVs are gaining attention because they decrease weight and cost for EV batteries and eliminate inconvenient charging stops—especially in public transit routes. Lancaster City Park has already produced a fleet of dynamically charging vehicles (DCVs) that recharge wirelessly during stops [2], and four other pilot pilot programs are under development for dynamically charging bus systems in the United States [3].

Dynamically charging vehicles (DCVs) that charge during transit are gaining popularity in public transportation systems because they eliminate overhanging charging wires, improve air quality, and promote quiet transportation. Additionally, charging coils can be installed on public transportation routes to decrease the size, weight, and price of the batteries installed on public transportation fleets.

One challenge for DCVs is the power-loss that occurs due to coil misalignment in wireless power transfer. Approaches to address coil misalignment include altering the material and shapes [4, 5], or increasing the number and placement of WPT transmitter and receivers [6, 7]. As expressed in the review done by Zicheng, there exists a trade-off between the misalignment tolerance and the size of the charging system with its corresponding vehicle and infrastructure costs [8]. To reduce infrastructure costs, Autonomous Dynamic Charging Vehicles (ADCVs) can be used to autonomously control a vehicle with sufficient accuracy to reduce the allowable misalignment tolerance. However, using a vehicle control law that maximizes power transfer with small lateral misalignment has the potential to cause rapid road wear and ruts–especially around charging regions.

To avoid unnecessary road damage, it is proposed that the ADCV's path planner inject white Gaussian noise passed through a noise shaping filter into the control inputs of the vehicle. However, introducing variability into an optimal charging path risks depleting battery life prior to destination arrival and increases rider discomfort.

As a result, the noise must be carefully shaped to guarantee average vehicle battery charge within a desired probability interval while ensuring the vehicle stays within its traveling lane, maintains acceleration comfort constraints, and maximizes variability.

To guarantee the vehicle receives a specified average charge, Monte Carlo simulations are performed in Section 3.6.4 to model the nonlinear effect that the WPT equations have on the injected variability. From the Monte Carlo simulations, an estimated standard deviation is also computed and a corresponding average charge can be guaranteed within a specified probability interval.

The proposed noise shaping filter is analyzed in Section 3.6.1, which addresses how to statically bound the position and comfort path deviations introduced by the noise shaping filter.

To address meeting passenger comfort constraints, this research proposes creating a Continuous Curvature Path (CCPath) using Clothoids in Section 3.4. Clothoids allow the acceleration of the vehicle to be bounded by the path planner, and they ensure the desired path is drivable. Creating a drivable path prevents large controller errors that can result in large control inputs that violate passenger comfort constraints.

To address the precise vehicle tracking required for WPT, this research proposes using a Kalman Filter for vehicle navigation in Section 3.2, and a linear control law in Section 3.5. Using the Kalman Filter, a full-state feedback infinite horizon Linear–Quadratic Regulator (LQR) controller is proposed that can track the Clothoid CCPath with zero analytical tracking error.

The results of system performance are then presented in Chapter 4, where the noise shaping filter performance is validated.

CHAPTER 2

LITERATURE REVIEW

The following sections outline notable research that relates to ADCVs. Topics include current accuracy of autonomous vehicles, wearing of vehicle roads, how passenger comfort is measured, and current vehicle control algorithms.

2.1 Vehicle Estimation Accuracy

Autonomous vehicles can achieve a mean error of 3 cm estimation accuracy using magnetic markers and odometry [9] and 4.3 cm estimation accuracy at highway speeds using the Localizing Ground Penetrating Radar (LGPR) validated using RTK GPS [10]. Because the necessary localization technology exists for ADCVs to locate their position within 4 cm at highway speeds, this paper assumes ADCVs can rely on autonomous navigation for maximum power transfer. Therefore, if similar transit vehicles drive a path within ±4 cm, road wear will increase as described in Section 2.2.

2.2 Road Wear

Ruts in the road are costly to repair and pose safety concerns due to their significant effect on hydroplaning [11, 12]. Rutting is caused by densification and shear deformation from repeated vehicle history and vehicle weight as seen in Figure 2.1 [13]. Accurate path following ADCVs will contribute to the formation of ruts and road wear due to their exact paths and low variance. Hjort reports that lateral wander with large variance extends road life–especially with decreasing pavement thickness [14]. Because DCVs are primarily implemented on heavier buses for public transportation, the ADCVs will cause more damage to roads than commercial vehicles [14]. Therefore, it is desirable that a path planner inject path variability to the vehicle's trajectory to prevent unnecessary road wear.
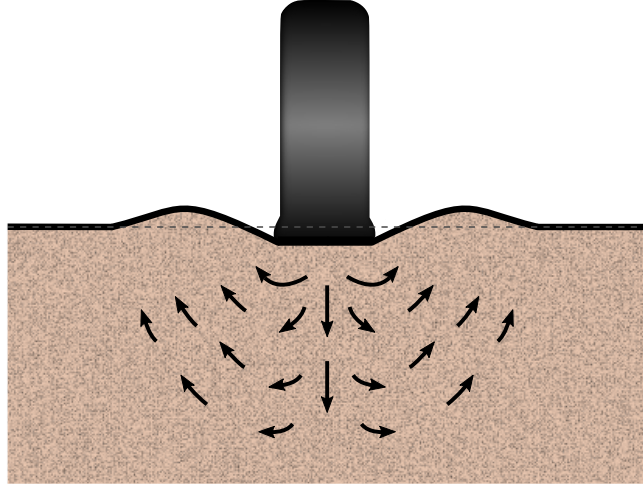
Fig. 2.1: Depiction of the formation of flow rutting based on repetitive vehicle travel.

2.3 Clothoid Smoothing

Fraichard rigorously defines how to use principles of minimum distance from the Reeds and Shepp's curves to form G^2 continuous paths and that have a linearly increasing curvature related to arc distance [15]. These paths are referred to as Clothoids—also known as the Euler Spiral. Clothoids are intrinsically drivable paths because they utilize the kinematic model of a vehicle to connect lines and arcs.

As described in [16], there are two basic approaches to forming continuous paths using the Clothoid. The first involves connecting way-points via lines, and smoothing the connection of the lines using Clothoid arcs.

The second approach is to directly connect connect way-points using mu-tangent circles connected with Clothoids, circular arcs, and lines [15]. Both approaches maintains G^2 continuity between the line segments and creates an intrinsically drivable path.

Because the Clothoid does not have a closed form solution it must be computed numerically. To avoid integration time, there are many approximation techniques for clothoids that include using Bezier curves, circular interpolation [17], or rotating and translating clothoid look-up tables [18]. Therefore, this research assumes Clothoids can be computed in real time to plan a drivable path that complies with passenger comfort constraints.

2.4 Passenger Comfort

Both acceleration and jerk affect passenger comfort in vehicles [19]. Intentionally adding variability to a vehicle path has the potential to cause passenger discomfort due to jerky motions and unnecessary accelerations. Acceleration discomfort levels are around $1.2 m/s^2$ for passengers, and jerk constraints are near $0.7 m/s^3$ [19, 20]. Villagra incorporates a global path planner that maintains curvature derivatives aimed at providing smooth driving, and it incorporates a "closed-form speed profile" to maintain acceleration and jerk constraints [21].

The frequency of acceleration also has an impact on motion sickness in passengers. Acceleration changes of 0.2 Hz are reported by Golding to increase the likelihood of motion sickness [22]. Therefore, a path planner that injects variability into a route must maintain constraints on the acceleration maximum and the frequency of acceleration changes.

2.5 Control Algorithms

Kinematic models are adequate for many control algorithms, and Snider reports that the pure pursuit controller method with an Ackermann bicycle steering model is well suited for slower driving vehicles. Snider also reports that a combination of control methods may be best depending on the speed and turn profile of the path [23].

Villagra shows that the pure kinematic bicycle model with an optimal path planner can be used to stay within comfort constraints and cross-track error constraints at speeds of $10 m/s$ [21].

CHAPTER 3

MATERIALS AND METHODS

This chapter presents the analysis used to produce the results in Chapter 4. The Sections contained in this chapter give the necessary background to both understand the methods and validate the results. Figure 3.1 represents the system diagram and presents topics that will be addressed.
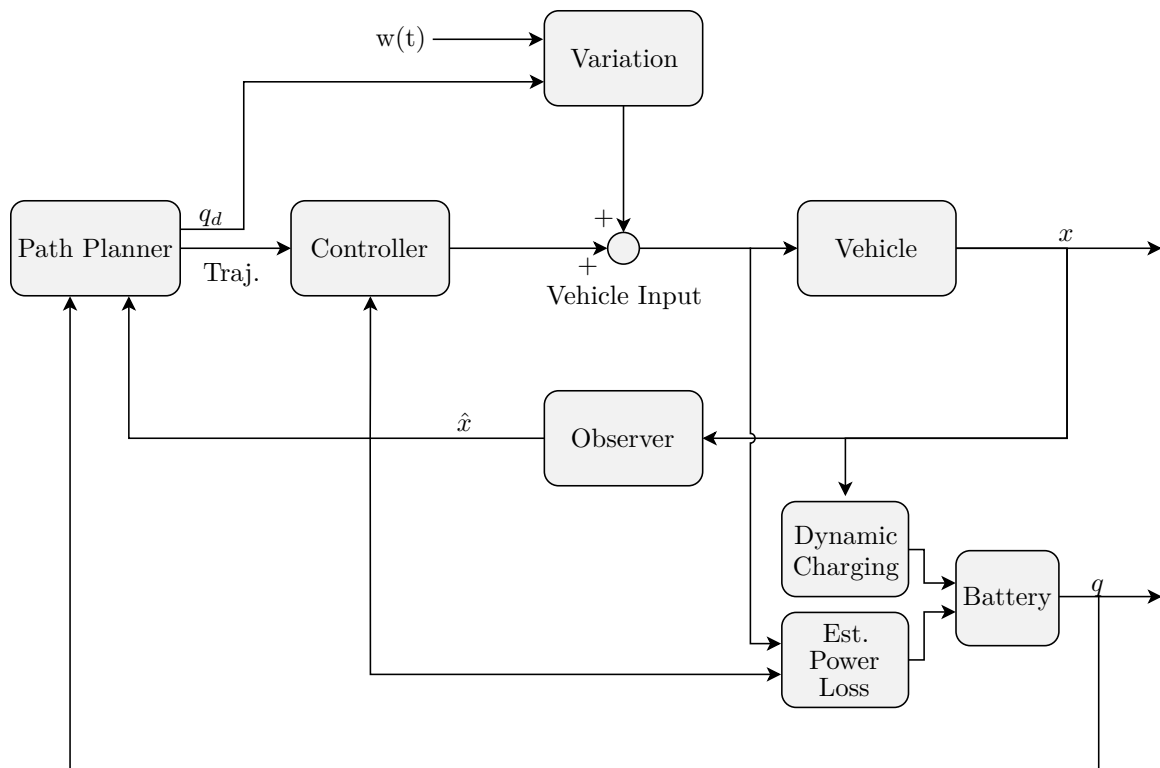
Fig. 3.1: High level block diagram of the control variation for a dynamically charged passenger vehicle.

The overall system goal depicted in Figure 3.1 is to arrive at the desired state x_d with a desired battery state of charge while maximizing path variation and complying with comfort and position constraints.

As a result, the Path Planner Node from Figure 3.1 receives both position and battery state of charge so that a driveable path and a desired average charge q_d can be calculated. Section 3.4 addresses the path planner and explores how the desired charge is calculated with a corresponding probability interval.

The Controller Node in Figure 3.1 is responsible for tracking a desired trajectory from the Path Planner. An infinite time horizon LQR controller is proposed in Section 3.5.

The Variation Node in Figure 3.1 is responsible for adding shaped noise to the vehicle path while ensuring the system and comfort constraints are met. The analysis of the comfort constraints and noise shaping filter to produce the variation are addressed in Section 3.6.

The Vehicle Node in Figure 3.1 simulates an Ackermann steering kinematic vehicle which is derived in Section 3.1.

The Observer Node in Figure 3.1 represents an Extended Kalman Filter based on continuous steering and velocity measurements with discrete position updates. The observer is derived and verified in Section 3.2.

The Dynamic Charging Node in Figure 3.1 addresses how the vehicle's battery charges via wireless power transfer (WPT) based on the lateral misalignment of the receiver and transmitters; the Dynamic Charging Node is analyzed in Section 3.3.

The Estimated Power Loss Node in Figure 3.1 is considered in Section 3.3, which addresses how the battery's state of charge is approximated based on the dynamics of the system for simulation purposes. The battery Node symbolizes the current state of the battery based on the sum of the estimated power loss and power gain through dynamic charging.

3.1 System Model

A system model is necessary for the system observer, controller, and path path planner of the autonomous vehicle. Depending on the speed and turn profile of a path, a combination of dynamic models and controllers may be necessary for best performance, but this research focuses on vehicles driving under $15m/s$ on urban paths.

As a result, kinematic models are well suited, and Snider cites that several champions of the DARPA Grand Challenge used simple kinematic vehicle models in their designs [23]. In addition, Villagra successfully shows that comfort constraints can be met using the ackermann's simplified bicycle model driving nominally at $10m/s$ [21]. This model is assumed because the algorithms included in this research are intended to be implemented on hardware at slower speeds first. Future research could include extending the models and algorithms to highway speed driving.

Therefore, the bicycle model is used for the system observer and controller commands as described in Sections 3.2 and 3.5 respectively. Figure 3.2 shows the geometric model, and its corresponding states can be seen in Equation 3.2. For completeness, the derivation of the equations of motion are completed in this section and are listed in Equation 3.17.

Assuming the vehicle is a rigid body with no air resistance or friction, the Ackermann Steering Model can be simplified to the bicycle model. The vehicle frame is referenced from the center of the back axle for several reasons. First there exists a geometric relationship between the steering angle ϕ and the curvature κ of the vehicle where

$$\kappa = \frac{v}{L} \tan \phi \tag{3.1}$$

at the center of the back axle. Additionally, establishing the reference point on the back axle allows the turning curvature to be smaller than on any other reference point of the vehicle, and the heading is aligned with the tangent of the direction of the path [24].
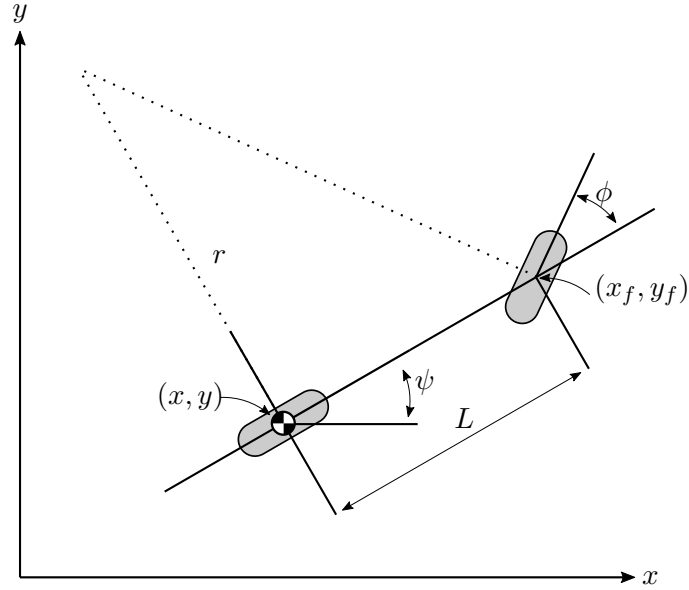
Fig. 3.2: Geometric relationships for the simplified Ackermann Steering Model referenced at the center of the back axle.

Assuming acceleration inputs, and by observation of Figure 3.2, the vehicle states can be described as

$$
\underline{x} = \begin{bmatrix} x \\ y \\ \psi \\ v \\ \phi \end{bmatrix}, \quad \underline{u} = \begin{bmatrix} a \\ \xi \end{bmatrix},
\tag{3.2}
$$

where ψ is heading, v is velocity, ϕ is steering angle. The inputs to the system are longitudinal acceleration a and steering angle change ξ.

The equations of motion are derived by first relating heading through small changes in x and y where

$$\tan \psi = \frac{\Delta y}{\Delta x}$$

$$\frac{\sin \psi}{\cos \psi} = \frac{\dot{y}}{\dot{x}}$$

$$\dot{x} \sin \psi - \dot{y} \cos \psi = 0. \qquad (3.3)$$

The point on the virtual front wheel can then be expressed as

$$\dot{x}_f \sin (\psi + \phi) - \dot{y}_f \cos (\psi + \phi) = 0. \qquad (3.4)$$

Any scalar multiple of Equations 3.3 and 3.4 is also a solution for each respective equation, therefore

$$v \cdot \dot{x} \sin \psi - v \cdot \dot{y} \cos \psi = 0 \qquad (3.5)$$

$$v \cdot \dot{x}_f \sin (\psi + \phi) - v \cdot \dot{y}_f \cos (\psi + \phi) = 0. \qquad (3.6)$$

Because Equations 3.7 and 3.8 satisfy Equation 3.5, the equations of motion for x and y can be written as

$$\dot{x} = v \cdot \cos \psi \text{ and} \qquad (3.7)$$

$$\dot{y} = v \cdot \sin \psi. \qquad (3.8)$$

The derivation continues by solving for the vehicle's change in heading $\dot{\psi}$ using the position of the front virtual wheel. The location of center of the virtual wheel in relation to the reference point is

$$x_f = x + L \cos \psi \qquad (3.9)$$

$$y_f = y + L \sin \psi. \qquad (3.10)$$

To eliminate the dependence of x_f and y_f on equation 3.6, Equations 3.9 and 3.10 are substituted into Equation 3.6 which results in

$$
\begin{aligned}
0 =& \frac{d}{dt} \left(x + L \cos \psi \right) \sin \left(\psi + \phi \right) - \frac{d}{dt} \left(y + L \sin \psi \right) \cos \left(\psi + \phi \right) \\
0 =& \left(\dot{x} - \dot{\psi} L \sin \psi \right) \sin \left(\psi + \phi \right) - \left(\dot{y} + \dot{\psi} L \cos \psi \right) \cos \left(\psi + \phi \right) \\
0 =& \dot{x} \sin \left(\psi + \phi \right) - \dot{y} \cos \left(\psi + \phi \right) \\
& - \dot{\psi} L \sin \psi \sin \left(\psi + \phi \right) - \dot{\psi} L \cos \psi \cos \left(\psi + \phi \right) \\
0 =& \dot{x} \sin \left(\psi + \phi \right) - \dot{y} \cos \left(\psi + \phi \right) \\
& - \dot{\psi} L \sin \psi \left(\sin \psi \cos \phi + \cos \psi \sin \phi \right) - \dot{\psi} L \cos \psi \left(\cos \psi \cos \phi - \sin \psi \sin \phi \right) \\
0 =& \dot{x} \sin \left(\psi + \phi \right) - \dot{y} \cos \left(\psi + \phi \right) - \dot{\psi} L \sin^2 \psi \cos \phi \\
& - \dot{\psi} L \cos^2 \psi \cos \phi + \dot{\psi} L \sin \psi \cos \psi \sin \phi - \dot{\psi} L \cos \psi \sin \psi \sin \phi \\
0 =& \dot{x} \sin \left(\psi + \phi \right) - \dot{y} \cos \left(\psi + \phi \right) - \dot{\psi} L \left(\sin^2 + \cos^2 \psi \right) \cos \phi \\
& + \dot{\psi} L \cos \psi \sin \psi \sin \phi - \dot{\psi} L \cos \psi \sin \psi \sin \phi \\
0 =& \dot{x} \sin \left(\psi + \phi \right) - \dot{y} \cos \left(\psi + \phi \right) - \dot{\psi} L \left(\sin^2 + \cos^2 \psi \right) \cos \phi \\
0 =& \dot{x} \sin \left(\psi + \phi \right) - \dot{y} \cos \left(\psi + \phi \right) - \dot{\psi} L \cos \phi. \tag{3.11}
\end{aligned}
$$

Solving for $\dot{\psi}$ yields,

$$
\begin{aligned}
0 &= \dot{x} \sin \left(\psi + \phi \right) - \dot{y} \cos \left(\psi + \phi \right) - \dot{\psi} L \cos \phi \\
\dot{\psi} L \cos \phi &= \dot{x} \sin \left(\psi + \phi \right) - \dot{y} \cos \left(\psi + \phi \right) \\
\dot{\psi} &= \frac{\dot{x} \sin \left(\psi + \phi \right) - \dot{y} \cos \left(\psi + \phi \right)}{L \cos \phi}. \tag{3.12}
\end{aligned}
$$

Now substituting the definition of $\dot{x}$ and $\dot{y}$ produces

$$\dot{\psi} = \frac{v \cdot \cos\psi \sin(\psi + \phi) - v \cdot \sin\psi \cos(\psi + \phi)}{L \cos\phi}$$

$$\dot{\psi} = \frac{v \cdot \cos\psi (\sin\psi \cos\phi + \cos\psi \sin\phi) - v \cdot \sin\psi (\cos\psi \cos\phi - \sin\psi \sin\phi)}{L \cos\phi}$$

$$\dot{\psi} = \frac{v \cdot \cos^2\psi \sin\phi + v \cdot \cos\psi \sin\psi \cos\phi - v \cdot \sin\psi \cos\psi \cos\phi + v \cdot \sin^2\psi \sin\phi}{L \cos\phi}$$

$$\dot{\psi} = \frac{v \cdot (\cos^2\psi + \sin^2\psi) \sin\phi + v \cdot \sin\psi \cos\psi \cos\phi - v \cdot \sin\psi \cos\psi \cos\phi}{L \cos\phi}$$

$$\dot{\psi} = \frac{v \cdot (\cos^2\psi + \sin^2\psi) \sin\phi}{L \cos\phi}$$

$$\dot{\psi} = \frac{v \cdot \sin\phi}{L \cos\phi}$$

$$\dot{\psi} = \frac{v}{L} \tan\phi. \tag{3.13}$$

Writing the combined equations of motions yields

$$\dot{x} = v \cdot \cos\psi$$

$$\dot{y} = v \cdot \sin\psi$$

$$\dot{\psi} = \frac{v}{L} \tan\phi. \tag{3.14}$$

By definition,

$$\dot{v} = a \tag{3.15}$$

$$\dot{\phi} = \xi, \tag{3.16}$$

Therefore the state space representation for the equations of motion is

$$\underline{\dot{x}} = \begin{bmatrix} \dot{x} \\ \dot{y} \\ \dot{\psi} \\ \dot{v} \\ \dot{\phi} \end{bmatrix} = \begin{bmatrix} v \cdot \cos\psi \\ v \cdot \sin\psi \\ \frac{v}{L}\tan\phi \\ 0 \\ 0 \end{bmatrix} + \begin{bmatrix} 0 & 0 \\ 0 & 0 \\ 0 & 0 \\ 1 & 0 \\ 0 & 1 \end{bmatrix} \begin{bmatrix} a \\ \xi \end{bmatrix}. \tag{3.17}$$

Equation 3.17 defines the equations of motion for the kinematic vehicle which are used for simulation propagation and vehicle control.

3.2   Extended Kalman Filter

A system observer is necessary to localize the autonomous vehicle and track the desired path. Due to the required high levels of precision for dynamic charging, the position estimate must be within ± 10 cm. To achieve the high level of precision, an Extended Kalman Filter (EKF) is a natural choice for the the observer due to the well defined kinematic equations from Section 3.1 and for fusing both continuous and discrete sensor measurements. Additionally, the EKF is used commonly for autonomous vehicles as seen in [25–27].

Possibilities for the discrete measurements vary widely, but two high accuracy positioning sensors include RTK GPS and magnetic markers. Byun shows that magnetic markers can be used to produce an error that averages 3 cm accuracy, but there exist surveying and installation costs for the magnets [28]. An RTK GPS system can produce up to 2 cm accuracy with 5 hz updates. To avoid the infrastructure costs of the magnetic slugs, the RTK GPS was selected for the discrete measurement for this project.

Possibilities for the continuous position and heading measurements are also varied, but velocity sensors, gyroscopes, and accelerometers are utilized between discrete updates as described in [25–27]. Interestingly, vehicle steering angle is not commonly used for position propagation even though the well defined model equations utilize steering angle, and the steering angle is often available on the CAN-bus. This research therefore proposes an EKF

that uses steering angle and velocity sensors as continuous measurements when the vehicle is in motion. It should be noted that the wheel speed sensor is likely to become less accurate at low velocities due to the limitations of wheel encoders, and that the initial heading of the vehicle can not be determined using only wheel speed and velocity sensors. The vehicle must be in motion for the EKF to produce an acceptable estimates for heading.

3.2.1 Navigation Filter

The navigation filter is used to estimate the current state of the vehicle, and the states for the navigation filter design model is

$$
\underline{\mathbf{x}} = \begin{bmatrix} x_1 \\ x_2 \\ \psi \\ b_v \\ b_\psi \end{bmatrix}, \tag{3.18}
$$

where x_1, x_2, and ψ correspond to x-position, y-positions, and heading respectively. Two new states b_v and b_ψ, have been introduced to the driving model derived in Equation 3.17 to estimate the bias terms in the velocity and steering angle sensors respectively.

Velocity and steering angle are no longer states in the navigation filter because they are sensor measurements with corresponding errors described in Section 3.2.1. The dynamics of the navigation state vector are

$$
\underline{\dot{\mathbf{x}}} = \begin{bmatrix} \dot{x}_1 \\ \dot{x}_2 \\ \dot{\psi} \\ \dot{b}_v \\ \dot{b}_\phi \end{bmatrix} = \begin{bmatrix} (\tilde{v} - b_v - n_v)\cos(\psi) \\ (\tilde{v} - b_v - n_v)\sin(\psi) \\ \frac{\tilde{v}-b_v-n_v}{L}\tan(\tilde{\phi} - b_\phi - n_\phi) \\ -\frac{1}{\tau_v}\hat{b}_v + w_v \\ -\frac{1}{\tau_\phi}\hat{b}_\phi + w_\phi \end{bmatrix}, \tag{3.19}
$$

and the measurement model is

$$
\tilde{\underline{y}} = \begin{bmatrix} \tilde{v} \\ \tilde{\phi} \end{bmatrix} = \begin{bmatrix} v + b_v + n_v \\ \phi + b_\phi + n_\phi \end{bmatrix}
\tag{3.20}
$$

where the variables $\tilde{v}$ and $\tilde{\phi}$ are the velocity and wheel angle sensors respectively.

State Propagation

The truth state propagation equation is depicted by Equation 3.21, and the propagation of the navigation filter is shown in Equation 3.22. The truth state propagation equation is used primarily for simulation, and it is not generally needed for implementation of the Kalman Filter.

A pictorial representation of the states can be seen in Figure 3.2 where x_1 and x_2 are the reference point of the vehicle on the back axel, and L is the wheel base length. The variable ϕ is the wheel angle and ψ is the vehicle orientation from the x_1 axis. The input variables are throttle a and the change in wheel angle ξ. The bias inherent in the velocity and steer angle sensors are b_v and b_ϕ respectively.

$$
\dot{\underline{x}} = \begin{bmatrix} \dot{x_1} \\ \dot{x_2} \\ \dot{\psi} \\ \dot{v} \\ \dot{\phi} \\ \dot{b_v} \\ \dot{b_\phi} \end{bmatrix} = \begin{bmatrix} v\,cos(\psi) \\ v\,sin(\psi) \\ \frac{v}{L}\,tan(\phi) \\ a \\ \xi \\ -\frac{1}{\tau_v}b_v + w_v \\ -\frac{1}{\tau_\phi}b_v + w_\phi \end{bmatrix}
\tag{3.21}
$$

The navigation states are propagated similar to the navigation filter design model, but without knowledge of the process noise where

$$\dot{\underline{\hat{x}}} = \begin{bmatrix} \dot{\hat{x}}_1 \\ \dot{\hat{x}}_2 \\ \dot{\hat{\psi}} \\ \dot{\hat{b}}_v \\ \dot{\hat{b}}_\phi \end{bmatrix} = \begin{bmatrix} (\tilde{v} - \hat{b}_v)\, cos(\hat{\psi}) \\ (\tilde{v} - \hat{b}_v)\, sin(\hat{\psi}) \\ \frac{\tilde{v} - \hat{b}_v}{L}\, tan(\tilde{\phi} - \hat{b}_\phi) \\ -\frac{1}{\tau_v}\hat{b}_v \\ -\frac{1}{\tau_\phi}\hat{b}_\phi \end{bmatrix} . \tag{3.22}$$

Results that show the correct implementation of the state propagation using Monte Carlo simulations are shown in Section 4.1.2.

3.2.2   Covariance Propagation

To propagate the covariance, the nonlinear navigation state matrix is linearized using the small angle approximation and taylor series expansion in the section titled Navigation Model Linearization. Then, the process noise in the Kalman filter is defined in the section titled Process Noise.

Navigation Model Linearization

The EKF requires linear equations to propagate the covariance. The linearized form of the navigation model can be expressed as a linear differential equation driven by white noise as seen in Equation 3.23. The covariance is propagated using the F and G matrices in the linearized form as shown in Equation 3.24, and values of matrices F and G are shown in Equation 3.25.

$$\delta\dot{\underline{x}} = F\left(\underline{x}, \tilde{\underline{y}}, t\right)\delta\underline{x} + G\left(\underline{x}, \tilde{\underline{y}}, t\right)\underline{w} \tag{3.23}$$

$$\dot{P} = FP + PF^T + GQG^T \tag{3.24}$$

$$
\begin{bmatrix} \delta\dot{x}_1 \\ \delta\dot{x}_2 \\ \delta\dot{\psi} \\ \delta\dot{b}_v \\ \delta\dot{b}_\phi \end{bmatrix} = \begin{bmatrix} 0 & 0 & -(\tilde{v}-b_v)\sin\hat{\psi} & -\cos\hat{\psi} & 0 \\ 0 & 0 & (\tilde{v}-b_v)\cos\hat{\psi} & -\sin\hat{\psi} & 0 \\ 0 & 0 & 0 & \frac{1}{L}\left(\tilde{\phi}-b_\phi\right) & -\frac{\tilde{v}-b_v}{L} \\ 0 & 0 & 0 & -\frac{1}{\tau_v} & 0 \\ 0 & 0 & 0 & 0 & -\frac{1}{\tau_\phi} \end{bmatrix} \begin{bmatrix} \delta x_1 \\ \delta x_2 \\ \delta\psi \\ \delta b_v \\ \delta b_\phi \end{bmatrix}
$$

$$
+ \begin{bmatrix} -\cos\hat{\psi} & 0 & 0 & 0 \\ -\sin\hat{\psi} & 0 & 0 & 0 \\ \frac{1}{L}(-\tilde{\phi}+b_\phi) & \frac{1}{L}(-\tilde{v}+b_v) & 0 & 0 \\ 0 & 0 & 1 & 0 \\ 0 & 0 & 0 & 1 \end{bmatrix} \begin{bmatrix} n_v \\ n_\phi \\ w_v \\ w_\phi \end{bmatrix} \qquad (3.25)
$$

For detailed steps regarding the derivation of the linearized F and G matrices, see Appendix .

Process Noise

Process noise is defined in this section to propagate the covariance of the estimate. The process noise vector is

$$
\underline{w} = \begin{bmatrix} n_v \\ n_\phi \\ w_v \\ w_\phi \end{bmatrix} . \qquad (3.26)
$$

The Power Spectral Density of $\underline{w}$ is

$$
E\left[\underline{w}\left(t\right)\underline{w}\left(t'\right)^T\right] = \hat{Q}_w \delta\left(t-t'\right), \qquad (3.27)
$$

and $\hat{Q}_w$ is equal to

$$\hat{Q}_w = \text{diag}\left[\begin{array}{cccc} Q_v & Q_\phi & Q_{bv} & Q_{b\phi} \end{array} \right], \tag{3.28}$$

where

$$Q_v = m^2_{\text{desired}}/t_{\text{desired}} \tag{3.29}$$

$$Q_\phi = rad^2_{\text{desired}}/t_{\text{desired}} \cdot \frac{L^2}{v^2_{\text{nom}}} \tag{3.30}$$

$$Q_{bv} = \frac{2\sigma_{v,ss}}{\tau_v} \tag{3.31}$$

$$Q_{b\phi} = \frac{2\sigma_{\phi,ss}}{\tau_\phi}. \tag{3.32}$$

For verification that the process noise is accurately predicted by the Kalman Filter, see Section 4.1.3.

3.2.3   Position Measurement

Equation 3.33 is used to propagate the Kalman filter co-variance matrix P^+, where the Kalman Gain is defined in the a posteriori by Equation 3.34, and $\mathbf{R}_p$ can be calculated using Equation 3.35.

$$\mathbf{P}^+ = \mathbf{P}^- - \mathbf{K}\mathbf{H}\mathbf{P}^- \tag{3.33}$$

$$\mathbf{K} = \mathbf{P}^-\mathbf{H}^\mathbf{T}\left(\mathbf{H}\mathbf{P}^-\mathbf{H}^\mathbf{T} + \mathbf{R_p}\right)^{-1} \tag{3.34}$$

$$\mathbf{R}_p\delta[n-m] = \mathrm{E}\left[\mathbf{v}[n]\mathbf{v}[m]^T\right] \tag{3.35}$$

The matrix $\mathbf{H}$ must be in a linearized form for the Kalman Gain a posteriori Equation, and it is computed by finding

$$\delta\mathbf{z}[k] = \mathbf{H}(\hat{\mathbf{x}}[k], k)\delta\mathbf{x}[k] + \nu[k], \tag{3.36}$$

where the matrix $\mathbf{H}$ is

$$\mathbf{H}_p = \begin{bmatrix} 1 & 0 & -L_\mathrm{ref}\sin\left(\hat{\psi}[k]\right) & 0 & 0 \\ 0 & 1 & L_\mathrm{ref}\cos\left(\hat{\psi}[k]\right) & 0 & 0 \end{bmatrix}. \tag{3.37}$$

For details regarding the measurement linearization, see Appendix A.1. For verification of the correct implementation of the discrete measurement update, see Section 4.1.4.

3.2.4   State and Covariance Update

The update portion of the Kalman Filter requires an apriori estimate from the propagation equation shown in Section 3.2.1 and a discrete measurement as derived in Section 3.2.3.

Given an incoming discrete measurement $\tilde{\underline{z}}$, the residual is computed by

$$\delta \hat{\underline{x}}^{+}[k] = \mathbf{K} \left(\tilde{\underline{z}}[k] - \hat{\tilde{\underline{z}}}[k] \right), \tag{3.38}$$

where $\hat{\tilde{\underline{z}}}[k]$ is the predicted measurement from the propagation equations.

The updated $\hat{\underline{x}}$ estimate is computed using the perturbation definitions of the error from Appendix A.1 by

$$\hat{\underline{x}}^{+} = \hat{\underline{x}}^{-} + \delta \hat{\underline{x}}^{+}[k]. \tag{3.39}$$

The Kalman Gain is computed by

$$\mathbf{K} = \mathbf{P}^{-}\mathbf{H}^{T} \left(\mathbf{H}\mathbf{P}^{-}\mathbf{H}^{T} + \mathbf{R} \right)^{-1}, \tag{3.40}$$

where $\mathbf{P}^{-}$ is the apriori covariance matrix obtained through continuous propagation from Section 3.2.1, $\mathbf{H}$ is the measurement matrix, and $\mathbf{R}$ is the measurement noise covariance defined in Section 3.2.3.

The Kalman Gain is also used for the covariance update which is computed as

$$\mathbf{P}^{+} = \left(\mathbf{I} - \mathbf{K}\mathbf{H} \right) \mathbf{P}^{-} \left(\mathbf{I} - \mathbf{K}\mathbf{H} \right)^{T} + \mathbf{K}\mathbf{R}\mathbf{K}^{T}. \tag{3.41}$$

For the results of simulations with the state and covariance updates, see Section 4.1.4.

3.3 State of Charge Model

A battery state of charge (SOC) model is necessary to ensure to ensure sufficient Wireless Power Transfer (WPT) levels are obtained with a specified probability after introducing path variability. The SOC model must estimate battery usage resulting from control input and physical forces acting on the vehicle. Additionally, the SOC model must estimate WPT based on the cross-track error between the receiver and transmitter coils. A model for lateral charging error is necessary to compare how different control variation affects the vehicle's SOC. In addition, the battery usage is reported in kilowatt hours (kWh) so that the battery power consumption can be verified using figures provided by vehicle manufactures.

The estimated SOC for battery usage is developed in Section 3.3.1 using Newtonian equations and verified in Section 4.2 using a Ford Focus 2012 vehicle profile. Section 3.3.2 then develops the dynamic charging model.

3.3.1 Battery Usage

The basic Newtonian equations that describe the forces acting on a vehicle can be seen in Figure 3.3.
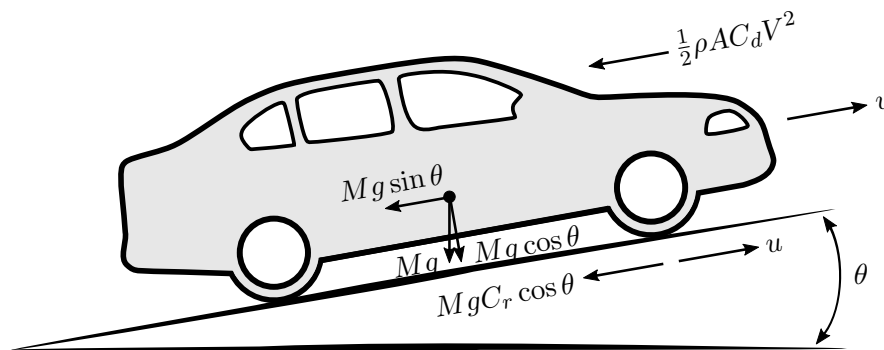
Fig. 3.3: Figure presenting the Newtonionan forces acting on a moving vehicle used to approximate battery usage.

The forces from Figure 3.3 can be expressed using the definition of force as

$$F = Ma \tag{3.42}$$

$$u - \sum F_r = f_m Ma, \tag{3.43}$$

where u is the input force, $\sum F_r$ is the sum of all resistive forces, f_m is the mass factor which converts rotational forces into longitudinal forces, M is the mass, and a is the vehicle acceleration [29].

The defined resistive forces are

$$F_{\text{rolling}} = MgC_r \cos\theta \tag{3.44}$$

$$F_{\text{air}} = \frac{1}{2}\rho AC_d v^2 \tag{3.45}$$

$$F_{\text{grade}} = Mg \sin\theta, \tag{3.46}$$

where the coefficient of rolling resistance is

$$C_r = 0.005 + \left(\frac{1}{p}\right)\left(0.01 + 0.0095\left(\frac{v}{100}\right)^2\right), \tag{3.47}$$

p is tire pressure (bar), and v is velocity (km/h) [30]. Power can then be calculated by

$$u - \sum F_r = f_m Ma$$

$$u = f_m Ma + \sum F_r$$

$$u = f_m Ma + F_{\text{rolling}} + F_{\text{air}} + F_{\text{grade}}$$

$$uv = \left(f_m Ma + F_{\text{rolling}} + F_{\text{air}} + F_{\text{grade}}\right) v$$

$$P = \left(f_m Ma + F_{\text{rolling}} + F_{\text{air}} + F_{\text{grade}}\right) v. \tag{3.48}$$

In addition to the battery usage, regenerative breaking can also be estimated by

$$P_r = \left(f_m Ma - F_{\text{rolling}} - F_{\text{air}} - F_{\text{grade}}\right) v, \tag{3.49}$$

where a is now the deceleration of the vehicle. Note that a scale factor should be included to reduce the regenerative braking power delivery due to the non-ideal transfer of power [29]. The proposed battery usage model can now be approximated for acceleration and nominal driving speed profiles.

3.3.2 Dynamic Charging

A first order approximation of dynamic charging is necessary to test the noise shaping filter's ability to produce a desired average charge. The model is split into two charging regions: the Full Charge Region and the Charge Transition Region as seen in Figure 3.4.
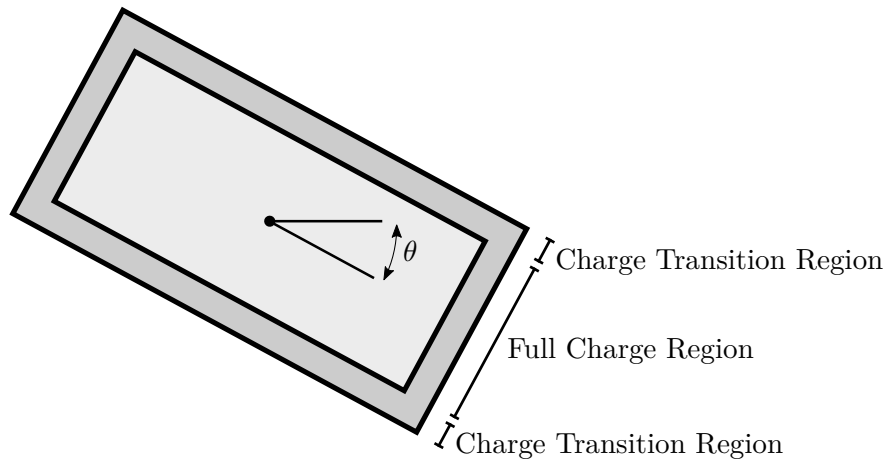
Fig. 3.4: Geometric properties of the dynamic charging model. When the center of the receiver coil is within the Full Charge Region, the WPT delivers a continuous 60 Watts. When the center of the receiver coil is within The Charge Transition Region, the WPT experinces a Sigmoid transition from 60 Watts to zeros Watts.

Figure 3.4 shows a rectangular Full Charge Region where the WPT transmitters deliver a continuous 60Watts. This is a reasonable approximation because the WPT power regulator is able to compensate for misalignment between the receiver and the transmitters. The Charge Transition Region is where the WPT power regulator is not able to compensate for the amount of misalignment, and a sharp power roll-off occurs; the roll-off can be approximated using a scaled Sigmoid function which creates a smooth transition between

the maximum and minimum values.

The section Sigmoid Transition Charging analyzes how to smooth the Zero Charge Region between the Full Charge Region. Then, the section Calculating Charge Based on Distance δ analyzes how to implement the charging regions based on distance from the center of the charging coil.

Sigmoid Transition Charging

The Charge Transition Region is approximated using a Sigmoid function to smooth the Zero Charge Region with the Full Charge Region. The definition of the Sigmoid function is

$$s\left(x\right) = \frac{1}{1 + e^{-x}}, \tag{3.50}$$

and a visual representation of the basic Sigmoid can be seen in Figure 3.5.
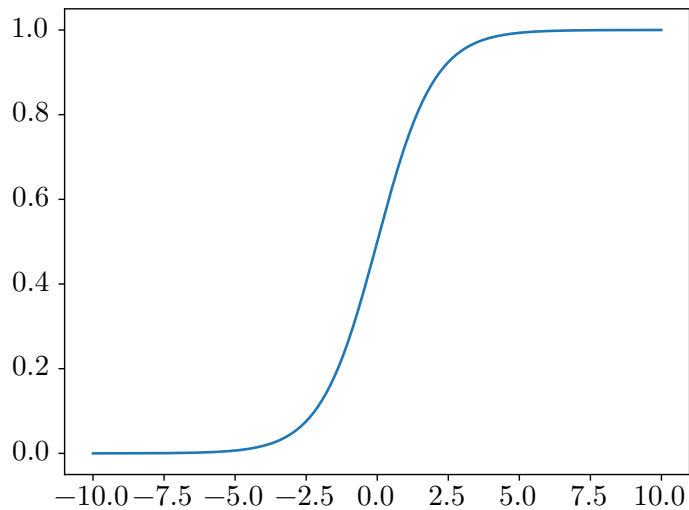
Fig. 3.5: Plot showing the basic Sigmoid Function used to create a smooth connection between zero charge and maximum charge.

Figure 3.5 shows that the Sigmoid is centered at 0 and makes an "s" shape. For the modeled charging pad, the Sigmoid is modified in two ways. First it is mirrored so that

an absolute value of the distance from the center of the charging pad δ will result in less charge. Second the Sigmoid is generalized to include additional parameters for its center and the scaling of its width transition. The altered Sigmoid function is

$$y = \frac{1}{1 + e^{w(x-c)}}, \tag{3.51}$$

where c is the new center and w is the width of the Sigmoid. For simulation purposes, c is equal to

$$c = (\text{full charge width}) + \frac{1}{2}(\text{transition width}), \tag{3.52}$$

and the width of the transition band is

$$w = 12/(\text{transition charge width}). \tag{3.53}$$

Calculating Charge Based on Distance δ

The absolute value of the longitudinal error from the center of the charging pad is used to determine the input charge to the battery. Using the description of the WPT charging model described in Section 3.3.2, the unscaled, nonlinear charging function relating longitudinal error and total charge received can be seen in Figure 3.6.
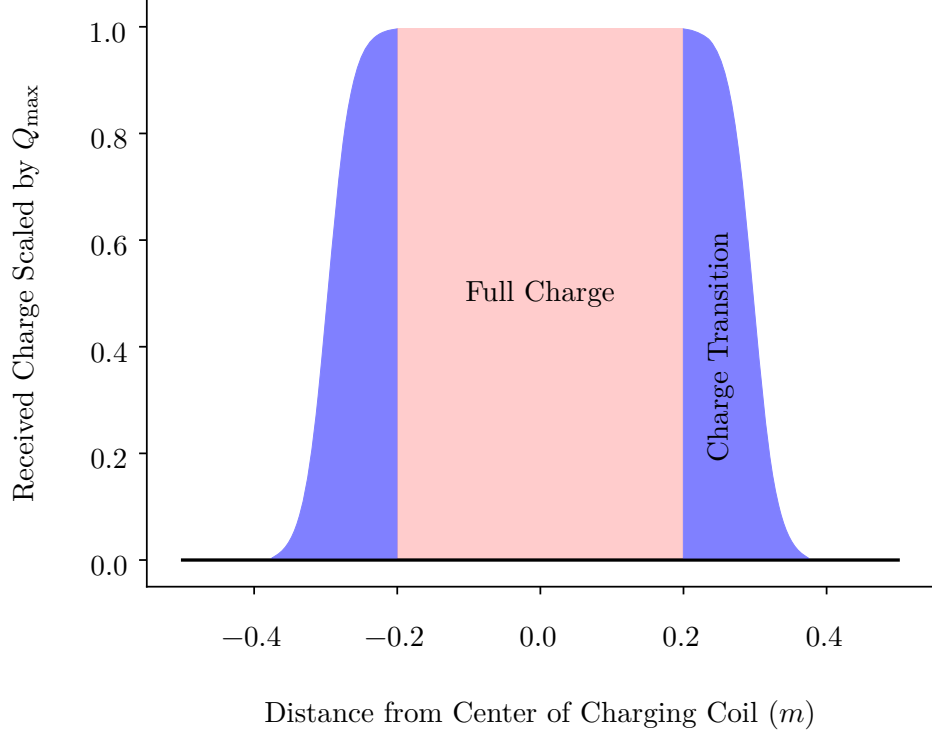
Fig. 3.6: Unscaled, nonlinear charging function relating distance from the center of the charging coil to the received WPT charge. Full Charge Region width $R_f = 0.4m$ and the Charge Transition Region width $R_t = 0.2m$.

The piece-wise equations used for calculating charge based on longitudinal error δ is

$$
f\left(\delta\right) = \begin{cases} Q_{\max} & |\delta| \leq R_f/2 \\[2mm] \frac{1}{1+e^{w(x-c)}} & R_f/2 < |\delta| < R_t \\[2mm] 0 & |\delta| \geq R_f/2 + R_t \end{cases}, \tag{3.54}
$$

where $Q_{\max}$ is the maximum WPT charge, R_f is the width of the Full Charge Region, R_t is the width of the charge transition region, $w = 12/R_t$, and $c = R_f/2 + R_t/2$.

3.4   Path Planner

A path planner is necessary to ensure the vehicle is given a drivable path that complies

with the comfort constraints outlined in Section 3.6, and that the vehicle arrives at its desired location with a specified charge. To maintain comfort constraints the path planner must solve for the necessary feed-forward terms to minimize vehicle tracking error. To arrive with a specified charge, the path planner must predict the vehicle's state of charge by the end of the journey and size the noise shaping filter to ensure the desired charge.

Section 3.4.1 compares way-point following techniques, and proposes that Clothoid way-point following is the best-suited solution for the system acceleration constraints.

Section 3.4.2 explores useful properties of the clothoid for solving feed-forward terms for the vehicle controller, and Section 3.4.3 outlines how the curvature of the path is bounded to ensure comfort constraints.

Finally, Section 3.4.4 proposes a method to size the noise shaping filter by calculating a desired average based on the estimated power consumption and WPT charge availability.

3.4.1 Way-point Following

Dubins paths and Continuous Curvature Paths (CCPaths) are two path planning schemes considered for creating a drivable path for a vehicle. Dubins paths connect way-points using circular arcs and lines in the optimal length given a curvature constraint, but they lack curvature continuity. The basic Dubins path implies that a vehicle can change steering angle instantaneously—which is an unreasonable assumption in many cases. The instantaneous change in curvature can result in wheel slip or violate jerk and acceleration comfort constraints.

Several techniques exist to smooth the discontinuities of the Dubins paths via look-ahead reference points [31], or Clothoid Smoothing [18]. However, such approaches make analyzing the path acceleration properties more difficult, or may not ensure a drivable path between way-points.

CCPaths are an extension to the Dubins driving model with an additional curvature state. The linearly changing curvature creates a continuous curvature trajectory profile [15] that matches a Clothoid. Villagra shows that CCPaths using Clothoids can be used to meet comfort constraints while optimizing the length of a trajectory [21].

Because the acceleration profile of a trajectory can be analyzed more accurately using a CCPath, it is a natural selection for compliance with the comfort constraints in Section 3.6.

3.4.2 Defining the CCPath Using Clothoids

The Clothoid, also referred to as the Euler Spiral, is described by a path whose curvature increases linearly with arc length. Because Clothoids maintain curvature continuity, they approximate the kinematic curvature change limits imposed by physical actuators and can be used to approximate a vehicle turn at a constant velocity.

Equation 3.55 shows the parametric equations to form a clothoid, where κ_0 is the initial turn radius, θ_0 is the initial heading, and σ is the change in turn radius.

$$x = C_f = x_0 + \int_0^s \cos\left(\frac{1}{2}\sigma(\xi^2 + \kappa_0\xi + \theta_0)\right) d\xi \tag{3.55}$$

$$y = S_f = y_0 + \int_0^s \sin\left(\frac{1}{2}\sigma(\xi^2 + \kappa_0\xi + \theta_0)\right) d\xi \tag{3.56}$$

As seen in Equation 3.55, Clothoids do not have a closed form. As a result, Clothoids are often precomputed and stored in a look-up table, or approximated in order to be used in real-time.

Integrating the Fresnel integrals produces the spiral seen in Figure 3.7 (a), and the corresponding linearly increasing curvature κ can be seen in Figure 3.7 (b).
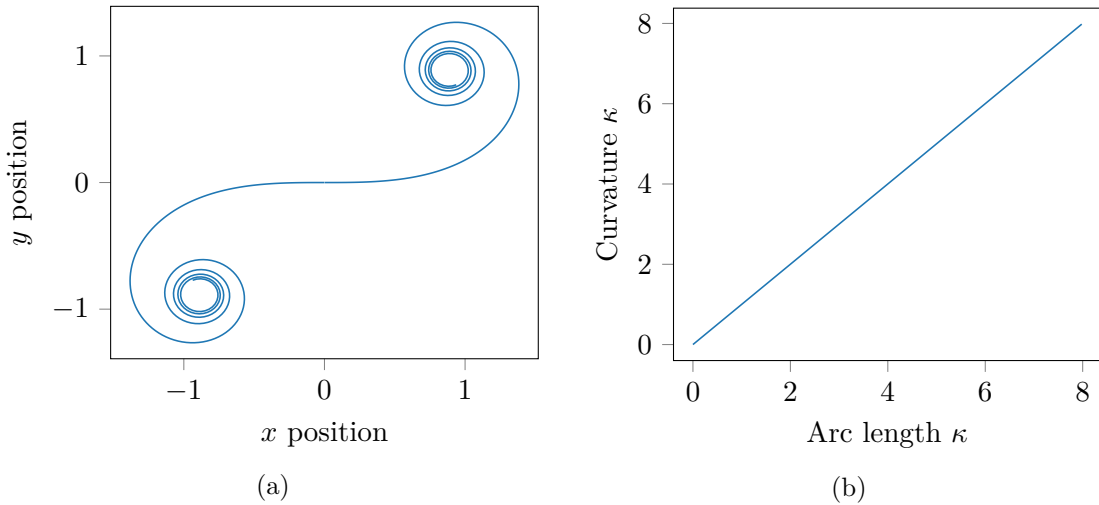
Fig. 3.7: (a) Fresnel Integral starting at 0 degrees and zero curvature moving in both the positive and negative direction. (b) Comparison of arc length to curvature for Fresnel integration.

An alternate form to produce the the Fresnel integral in Figure 3.7, is proposed by Fraichard by extending Dubins model to include a curvature state [15].

The equations of motion for the extended Dubins model are

$$
\underline{\dot{x}} = \begin{bmatrix} \dot{x} \\ \dot{y} \\ \dot{\theta} \\ \dot{\kappa} \end{bmatrix} = \begin{bmatrix} v \cdot \cos\theta \\ v \cdot \sin\theta \\ v \cdot \kappa \\ 0 \end{bmatrix} + \begin{bmatrix} 0 \\ 0 \\ 0 \\ 1 \end{bmatrix} \sigma,
\tag{3.57}
$$

where x and y are position, θ is heading, and κ is curvature. Using Equation 3.57, A CCTurn is created when the extended Dubins model reaches κ_{max}, and the vehicle transitions from driving a clothoid path to a circular arc. Therefore, a path can be computed by connecting way-points via Clothoids, straight lines, and circular arcs as seen in Figure 3.8.
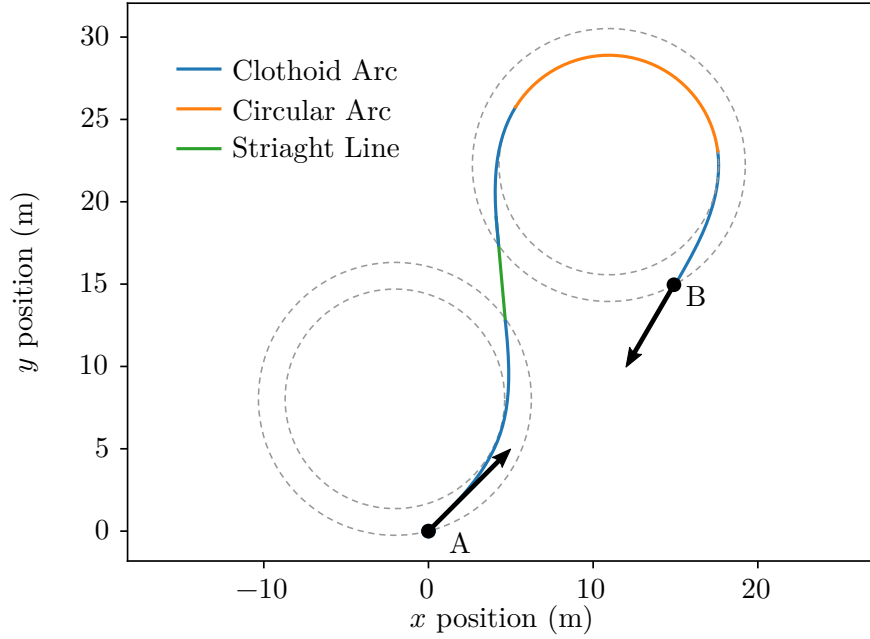
Fig. 3.8: Connecting directional way-points A and B using Clothoids, straight lines and circular arcs.

Because the points connected in figure 3.8 utilize the kinematic equations of motion from Equation 3.57, the acceleration comfort constraints of the vehicle can be analyzed using the CCPath.

3.4.3 Implementing Maximum Curvature Constraints

In order to maintain the comfort constraints outlined in Section 3.6, the maximum allowable curvature for a given velocity must be calculated. Assuming a vehicle is traveling at a constant longitudinal velocity, the normal acceleration is

$$\alpha_n = \frac{v^2}{r} = \kappa v^2, \tag{3.58}$$

where r is the radius of the turn and κ is curvature. Therefore, the allowable maximum curvature is

$$\kappa_{\max} = \frac{\alpha_{n\max}}{v^2}. \tag{3.59}$$

Additionally, the maximum allowable curvature is bounded by the slipping constraints of the wheel. Assuming the coefficient of friction between the wheels and the road is μ, the maximum allowable normal acceleration before slipping is

$$\alpha_{n\max} = \mu g \tag{3.60}$$

$$\kappa v^2 = \mu g \tag{3.61}$$

$$\kappa_{\max} = \frac{\mu g}{v^2} \tag{3.62}$$

where g is gravity. Which implies that the allowable curvature for a vehicle is

$$\kappa \leq \min\left(\frac{\alpha_{n\max}}{v^2}, \frac{\mu g}{v^2}\right). \tag{3.63}$$

To extend the curvature model from Section 3.57 to the bicycle model, a relationship between steering angle and curvature must be defined. Using the kinematic system model from Section 3.1, the steering angle of a vehicle relates to the curvature through

$$\kappa = r^{-1} = \frac{\tan\phi}{L}, \tag{3.64}$$

where ϕ is the steering angle. Therefore, the maximum allowable steering angle to stay within system constraints is

$$\phi \leq \min\left(\arctan\left(\frac{L\alpha_{n\max}}{v^2}\right), \arctan\left(\frac{L\mu g}{v^2}\right)\right). \tag{3.65}$$

To comply with jerk constraints, it is assumed that the system is driving at a constant velocity, and that the maximum allowable jerk is near $j = 0.5\,m/s^3$ [19,20]. Consider again the definition of normal acceleration. Taking the derivative yields that jerk is equal to

$$\dot{\alpha}_n = \frac{d}{dt}\left(\kappa v^2\right) \tag{3.66}$$

$$j = 2v\dot{v}\kappa + v^2\dot{\kappa}. \tag{3.67}$$

Assuming longitudinal acceleration is zero, the maximum change in curvature can be computed as

$$j = v^2 \dot{\kappa} \tag{3.68}$$

$$\dot{\kappa}_{\mathrm{max}} = \frac{j_{\mathrm{max}}}{v^2}. \tag{3.69}$$

Therefore, the clothoid way-point path planner can be used to ensure the desired trajectory is within specified comfort constraints using Equation 3.63 and 3.69.

3.4.4 Ensuring Destination State of Charge

A key role of the path planner is to calculate the desired average charge q_d for the noise shaping filter that ensures a desired battery charge at a vehicle's destination.

One method to determine the estimated change of battery state of charge Q_{wH} in watt-hours is to subtract the average expected power used r_e of the battery from the average expected power gained q_e over their respective time periods

$$Q_{\mathrm{wH}} = q_e t_q - r_e t_r, \tag{3.70}$$

where t_q is the amount of time the battery is receiving power, and t_r is the amount of time the battery is using power. It then follows that the desired average charge q_d to achieve a desired Q_{wH} given t_r, t_q and r_e is

$$q_d = \frac{Q_{\mathrm{wH}}}{t_q} + r_e t_r. \tag{3.71}$$

Therefore, to ensure a final battery charge in watt-hours at a final destination, the variables t_r, t_q, and r_e must be estimated.

The time required to reach the destination can be computed as a function of the distance d and velocity v. For this anlysis, it is assumed that v is constant, therefore

$$t_r = \frac{d}{v},$$

where d is the distance from the current position to the destination.

The amount of time the vehicle can charge is a function of the charging region's length d_q and velocity

$$t_q = \frac{d_q}{v},$$

where d_q is the length of the sum of all charging regions between the current position and the destination.

One approach for calculating r_e is to periodically use the average consumed power over a recent time period. This approach accounts for unknown resistive forces by assuming that future conditions will be similar to the conditions over a recent time period.

3.5 Feedback Controller Design

A controller that tracks a trajectory within ± 10 cm is desirable due to the narrow charging region of the WPT coils. Additionally, the controller must stay within the outlined comfort constraints proposed in Section 3.6, and therefore an acceleration or jerk controller is suited for comfortable driving.

Because both high tracking precision and low input controls are needed to comply with system constraints, an emphasis is placed on developing a completely drivable path in Section 3.4. The Path Planner also solves corresponding feed-forward terms to reduce trajectory error. The controller, therefore should interface well with the path planner and avoid violating the comfort constraints outlined in Section 3.6.

Model Predictive Control (MPC) is a natural control candidate that fits the system constraints; using MPC, a cost function can be generated that weighs vehicle safety, cross-

track error, acceleration input size, and battery consumption. However, due to the Monte Carlo testing simulation platform, a less computational alternative using linear control methods is utilized.

A linear point control method proposed by Olfati-Saber uses a diffeomorphism to transform a mobile robot with non-holonomic constraints into a completely controllable point. The new control point is a distance ϵ in front of the vehicle reference point, and it does not share the non-holonomic constraints of the vehicle [32]. Olfati-Saber uses nonlinear analysis to show that zero-tracking error can be achieved by allowing ϵ to go to zero as time goes to infinity.

However, in implementation the sensor noise in real systems does not allow ϵ go to zero, which introduces an analytical steady state error using the point control method.

Therefore, a modification of the ϵ-Tracking controller is proposed in Section 3.5.2.

Section 3.5.1 derives a linear ϵ-Tracking control to for the Ackermann Steering Model proposed in Section 3.1 so that full-state linear feedback can be applied to the vehicle.

3.5.1   Feedback Linearization

The Kinematic Ackermann Steering Model derived in Section 3.1 has non-holonomic constraints that restricts the system from being completely controllable. The non-holonomic constraint exists because the vehicle reference point at the center of the rear axle can not move orthogonal to the direction of the vehicle motion [33].

To make the system controllable, a diffeomorphism can be employed to control a new reference point $\underline{y}_\epsilon$ that is distance ϵ in front of the vehicle. Such a point does not share the non-holonomic constraints of the Ackermann Steering Model, and the point is completely controllable. A depiction of this approach as seen in Figure 3.9.
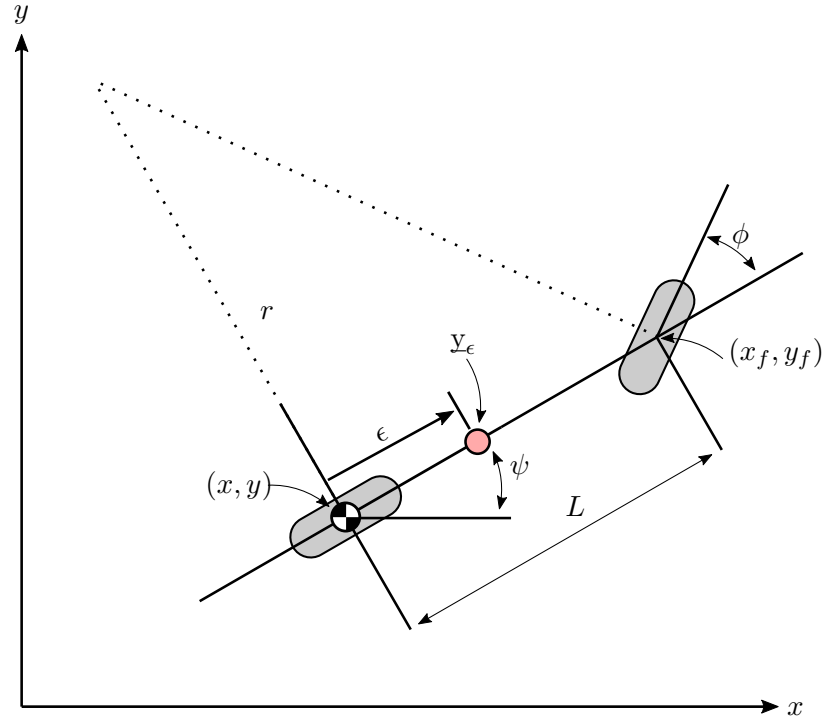
Fig. 3.9: Figure depicting the proposed control reference point y_ϵ used to linearize the Ackermann Steering Model.

Figure 3.9 shows that the new control point $\underline{y}_\epsilon$ does not share the same non-holonomic constraint as the rear axle reference point. The remainder of this section derives how to control the reference point $\underline{y}_\epsilon$ using the vehicle acceleration inputs.

The function for the new control point $\underline{y}_\epsilon$ as seen in figure 3.9 is defined as

$$\underline{y}_\epsilon = \begin{bmatrix} x \\ y \end{bmatrix} + \epsilon \begin{bmatrix} \cos\psi \\ \sin\psi \end{bmatrix}. \tag{3.72}$$

Taking the first derivative of $\underline{y}_\epsilon$ yields

$$\dot{\underline{y}}_\epsilon = \begin{bmatrix} \dot{x} \\ \dot{y} \end{bmatrix} + \epsilon \begin{bmatrix} -\dot{\psi}\sin\psi \\ \dot{\psi}\cos\psi \end{bmatrix}. \tag{3.73}$$

Making the following substitutions

$$\dot{x} = v \cos \psi \tag{3.74}$$

$$\dot{y} = v \sin \psi \tag{3.75}$$

$$\dot{\psi} = \omega \tag{3.76}$$

where ω is angular rotation of the system, then

$$\dot{\underline{Y}}_\epsilon = \begin{bmatrix} \dot{x} \\ \dot{y} \end{bmatrix} + \epsilon \begin{bmatrix} -\dot{\psi} \sin \psi \\ \dot{\psi} \cos \psi \end{bmatrix}$$

$$\dot{\underline{Y}}_\epsilon = \begin{bmatrix} v \cos \psi \\ v \sin \psi \end{bmatrix} + \epsilon \begin{bmatrix} -\omega \sin \psi \\ \omega \cos \psi \end{bmatrix}$$

$$\dot{\underline{Y}}_\epsilon = \begin{bmatrix} \cos \psi \\ \sin \psi \end{bmatrix} v + \begin{bmatrix} -\epsilon \sin \psi \\ \epsilon \cos \psi \end{bmatrix} \omega$$

$$\dot{\underline{Y}}_\epsilon = \begin{bmatrix} \cos \psi & -\epsilon \sin \psi \\ \sin \psi & \epsilon \cos \psi \end{bmatrix} \begin{bmatrix} v \\ \omega \end{bmatrix}. \tag{3.77}$$

Let, $R_\epsilon = \begin{bmatrix} \cos \psi & -\epsilon \sin \psi \\ \sin \psi & \epsilon \cos \psi \end{bmatrix}$ and $\underline{v} = \begin{bmatrix} v \\ \omega \end{bmatrix}$. Therefore,

$$\dot{\underline{Y}}_\epsilon = R_\epsilon \underline{v}. \tag{3.78}$$

The second derivative of $\underline{y}_\epsilon$ is

$$\ddot{\underline{y}}_\epsilon = \frac{d}{dt}\left(\begin{bmatrix} v\cos\psi \\ v\sin\psi \end{bmatrix} + \epsilon \begin{bmatrix} -\omega\sin\psi \\ \omega\cos\psi \end{bmatrix}\right)$$

$$\ddot{\underline{y}}_\epsilon = \begin{bmatrix} \dot{v}\cos\psi - \dot{\psi}v\sin\psi \\ \dot{v}\sin\psi + \dot{\psi}v\cos\psi \end{bmatrix} + \epsilon \begin{bmatrix} -\dot{\omega}\sin\psi - \omega\dot{\psi}\cos\psi \\ \dot{\omega}\cos\psi - \omega\dot{\psi}\sin\psi \end{bmatrix}$$

$$\ddot{\underline{y}}_\epsilon = \begin{bmatrix} \dot{v}\cos\psi - \omega v\sin\psi \\ \dot{v}\sin\psi + \omega v\cos\psi \end{bmatrix} + \epsilon \begin{bmatrix} -\dot{\omega}\sin\psi - \omega^2\cos\psi \\ \dot{\omega}\cos\psi - \omega^2\sin\psi \end{bmatrix}. \tag{3.79}$$

Let $\dot{v} = a$ and $\dot{\omega} = \sigma$. Then

$$\ddot{\underline{y}}_\epsilon = \begin{bmatrix} a\cos\psi - \omega v\sin\psi \\ a\sin\psi + \omega v\cos\psi \end{bmatrix} + \epsilon \begin{bmatrix} -\sigma\sin\psi - \omega^2\cos\psi \\ \sigma\cos\psi - \omega^2\sin\psi \end{bmatrix}$$

$$\ddot{\underline{y}}_\epsilon = \begin{bmatrix} a\cos\psi - \omega v\sin\psi \\ a\sin\psi + \omega v\cos\psi \end{bmatrix} + \begin{bmatrix} -\epsilon\sigma\sin\psi - \epsilon\omega^2\cos\psi \\ \epsilon\sigma\cos\psi - \epsilon\omega^2\sin\psi \end{bmatrix}$$

$$\ddot{\underline{y}}_\epsilon = \begin{bmatrix} -\omega v\sin\psi - \epsilon\omega^2\cos\psi \\ \omega v\cos\psi - \epsilon\omega^2\sin\psi \end{bmatrix} + \begin{bmatrix} a\cos\psi - \epsilon\sigma\sin\psi \\ a\sin\psi + \epsilon\sigma\cos\psi \end{bmatrix}$$

$$\ddot{\underline{y}}_\epsilon = \begin{bmatrix} -\omega v\sin\psi - \epsilon\omega^2\cos\psi \\ \omega v\cos\psi - \epsilon\omega^2\sin\psi \end{bmatrix} + \begin{bmatrix} \cos\psi & -\epsilon\sin\psi \\ \sin\psi & \epsilon\cos\psi \end{bmatrix}\begin{bmatrix} a \\ \sigma \end{bmatrix}$$

$$\ddot{\underline{y}}_\epsilon = \begin{bmatrix} \cos\psi & -\epsilon\sin\psi \\ \sin\psi & \epsilon\cos\psi \end{bmatrix}\begin{bmatrix} 0 & \epsilon\omega \\ \omega/\epsilon & 0 \end{bmatrix}\begin{bmatrix} v \\ \omega \end{bmatrix} + \begin{bmatrix} \cos\psi & -\epsilon\sin\psi \\ \sin\psi & \epsilon\cos\psi \end{bmatrix}\begin{bmatrix} a \\ \sigma \end{bmatrix}. \tag{3.80}$$

$$\ddot{\underline{y}}_\epsilon = R_\epsilon \begin{bmatrix} 0 & \epsilon\omega \\ \omega/\epsilon & 0 \end{bmatrix}\underline{v} + R_\epsilon \begin{bmatrix} a \\ \sigma \end{bmatrix}. \tag{3.81}$$

Now let $\hat{\omega} = \begin{bmatrix} 0 & \epsilon\omega \\ \omega/\epsilon & 0 \end{bmatrix}$, and $\underline{a} = \begin{bmatrix} a \\ \sigma \end{bmatrix}$. Then

$$\ddot{\underline{y}}_\epsilon = R_\epsilon\hat{\omega}\underline{v} + R_\epsilon\underline{a}. \tag{3.82}$$

The equations of motion for the point $\underline{y}_\epsilon$ can now be written compactly as

$$\underline{y}_\epsilon = \begin{bmatrix} x \\ y \end{bmatrix} + \epsilon \begin{bmatrix} \cos\psi \\ \sin\psi \end{bmatrix}, \tag{3.83}$$

$$\dot{\underline{y}}_\epsilon = \begin{bmatrix} \cos\psi & -\epsilon\sin\psi \\ \sin\psi & \epsilon\cos\psi \end{bmatrix} \begin{bmatrix} v \\ \omega \end{bmatrix} = R_\epsilon \underline{v}, \tag{3.84}$$

$$\ddot{\underline{y}}_\epsilon = \begin{bmatrix} \cos\psi & -\epsilon\sin\psi \\ \sin\psi & \epsilon\cos\psi \end{bmatrix} \begin{bmatrix} 0 & \epsilon\omega \\ \omega/\epsilon & 0 \end{bmatrix} \begin{bmatrix} v \\ \omega \end{bmatrix} + \begin{bmatrix} \cos\psi & -\epsilon\sin\psi \\ \sin\psi & \epsilon\cos\psi \end{bmatrix} \begin{bmatrix} a \\ \sigma \end{bmatrix} = R_\epsilon \hat{\omega} \underline{v} + R_\epsilon \underline{a}. \tag{3.85}$$

where

$$\dot{\psi} = \omega = \frac{v}{L}\tan\phi \tag{3.86}$$

$$a = \text{longitudinal acceleration} \tag{3.87}$$

$$\sigma = \text{angular acceleration.} \tag{3.88}$$

The control for the point $\underline{y}_\epsilon$ can now be placed into a state Equation where $\underline{u}_\epsilon$ is the input required to control the point $\underline{y}_\epsilon$. The linear state space equations for controlling $\underline{y}_\epsilon$ are

$$\dot{\underline{y}}_\epsilon = \mathbf{A}\underline{y}_\epsilon + \mathbf{B}\underline{u}_\epsilon \tag{3.89}$$

$$\begin{bmatrix} \dot{\underline{y}}_\epsilon \\ \ddot{\underline{y}}_\epsilon \end{bmatrix} = \begin{bmatrix} 0 & \mathbf{I} \\ 0 & 0 \end{bmatrix} \begin{bmatrix} \underline{y}_\epsilon \\ \dot{\underline{y}}_\epsilon \end{bmatrix} + \begin{bmatrix} 0 \\ \mathbf{I} \end{bmatrix} \underline{u}_\epsilon. \tag{3.90}$$

The input $\underline{u}$ to the linear system in Equation 3.89 can be related to the original system input by using the information from Equation 3.85 to solve for $\underline{a}$, the input to the vehicle (in terms of longitudinal velocity and rotational velocity). Therefore, the input from the

vehicle to control the point $\underline{y}_\epsilon$ is

$$\ddot{\underline{y}}_\epsilon = \underline{u}_\epsilon$$

$$R_\epsilon \hat{\omega} \underline{v} + R_\epsilon \underline{a} = \underline{u}_\epsilon$$

$$R_\epsilon \underline{a} = \underline{u}_\epsilon - R_\epsilon \hat{\omega} \underline{v}$$

$$\underline{a} = R_\epsilon^{-1} \left(\underline{u}_\epsilon - R_\epsilon \hat{\omega} \underline{v} \right)$$

$$\underline{a} = R_\epsilon^{-1} \underline{u}_\epsilon - \hat{\omega} \underline{v}. \tag{3.91}$$

Because the vehicle system input has been related to the $\underline{y}_\epsilon$, a traditional linear control law can be used to control the $\underline{y}_\epsilon$ system. Therefore, let $\underline{y}_{\epsilon d}$ be a desired trajectory point, then the zero steady state error can be represented as

$$\underline{z} = \underline{y}_\epsilon - \underline{y}_{\epsilon d} \tag{3.92}$$

$$\dot{\underline{z}} = \dot{\underline{y}}_\epsilon - \dot{\underline{y}}_{\epsilon d}. \tag{3.93}$$

Putting the system in terms of the new variable results in

$$\dot{\underline{z}} = \mathbf{A} \underline{y}_\epsilon + \mathbf{B} \underline{u}_\epsilon - \dot{\underline{y}}_{\epsilon d}. \tag{3.94}$$

Solving $\underline{y}$ from equation 3.92 produces

$$\underline{y}_\epsilon = \underline{z} + \underline{y}_{\epsilon d}$$

$$\dot{\underline{y}}_\epsilon = \dot{\underline{z}} + \dot{\underline{y}}_{\epsilon d}.$$

Continuing the change of variables results in

$$\dot{\underline{z}} = \mathbf{A} \underline{y}_\epsilon + \mathbf{B} \underline{u} - \dot{\underline{y}}_{\epsilon d}$$

$$\dot{\underline{z}} = \mathbf{A} \left(\underline{z} + \underline{y}_{\epsilon d} \right) + \mathbf{B} \underline{u} - \dot{\underline{y}}_{\epsilon d}$$

$$\dot{\underline{z}} = \mathbf{A} \underline{z} + \mathbf{B} \underline{u} + \mathbf{A} \underline{y}_{\epsilon d} - \dot{\underline{y}}_{\epsilon d}. \tag{3.95}$$

Solving for the steady state feed forward term $\underline{u}_{ff}$ is

$$\dot{\underline{z}} = \mathbf{A}\underline{z} + \mathbf{B}\underline{u} + \mathbf{A}\underline{y}_{\epsilon d} - \dot{\underline{y}}_{\epsilon d}$$

$$\mathbf{0} = \mathbf{0} + \mathbf{B}\underline{u} + \mathbf{A}\underline{y}_{\epsilon d} - \dot{\underline{y}}_{\epsilon d}$$

$$\begin{bmatrix} 0 \\ 0 \end{bmatrix} = \begin{bmatrix} 0 \\ \mathbf{I} \end{bmatrix} \underline{u}_{ff} + \begin{bmatrix} 0 & \mathbf{I} \\ 0 & 0 \end{bmatrix} \begin{bmatrix} \underline{y}_{\epsilon d} \\ \dot{\underline{y}}_{\epsilon d} \end{bmatrix} - \begin{bmatrix} \dot{\underline{y}}_{\epsilon d} \\ \ddot{\underline{y}}_{\epsilon d} \end{bmatrix}$$

$$\begin{bmatrix} 0 \\ 0 \end{bmatrix} = \begin{bmatrix} 0 \\ \underline{u}_{ff} \end{bmatrix} + \begin{bmatrix} \dot{\underline{y}}_{\epsilon d} \\ 0 \end{bmatrix} - \begin{bmatrix} \dot{\underline{y}}_{\epsilon d} \\ \ddot{\underline{y}}_{\epsilon d} \end{bmatrix}$$

$$0 = \underline{u}_{ff} - \ddot{\underline{y}}_{\epsilon d}$$

$$\underline{u}_{ff} = \ddot{\underline{y}}_{\epsilon d}. \tag{3.96}$$

Because the vehicle system input is not angular acceleration σ, but rather change in steering angle ξ, the algebraic relationship between angular acceleration and change in steering angle is

$$\sigma = \dot{\omega}$$

$$\sigma = \frac{d}{dt}\left(\frac{v}{L}\tan\phi\right)$$

$$\sigma = \frac{\dot{v}}{L}\tan\phi + \frac{v}{L}\frac{d}{dt}\left(\tan\phi\right)$$

$$\sigma = \frac{a}{L}\cdot\tan\phi + \frac{v}{L}\cdot\frac{\xi}{\cos^2\phi}$$

$$-\frac{v}{L}\cdot\frac{\xi}{\cos^2\phi} = \frac{a}{L}\cdot\tan\phi - \sigma$$

$$\xi = -\frac{L}{v}\cos^2\phi\left(\frac{a}{L}\cdot\tan\phi - \sigma\right)$$

$$\xi = \frac{1}{v}\cos^2\phi\left(L\sigma - a\cdot\tan\phi\right). \tag{3.97}$$

The new control law can now be written as

$$\begin{bmatrix} a \\ \sigma \end{bmatrix} = R_\epsilon^{-1}\left(\ddot{\underline{y}}_{\epsilon d} - K\left(\begin{bmatrix} \underline{y}_\epsilon \\ \dot{\underline{y}}_\epsilon \end{bmatrix} - \begin{bmatrix} \underline{y}_{\epsilon d} \\ \dot{\underline{y}}_{\epsilon d} \end{bmatrix}\right)\right) - \hat{\omega}\underline{v}. \tag{3.98}$$

Where the system input is

$$
\begin{bmatrix} a \\ \xi \end{bmatrix} = \begin{bmatrix} a \\ \frac{1}{v} \cos^2 \phi \left(L\sigma - a \cdot \tan \phi \right) \end{bmatrix}. \tag{3.99}
$$

3.5.2 Calculating an ϵ-Tracking Control Path

Using the ϵ-Tracking linearization approach introduced in Section 3.5.1 produces a steady state error the length of ϵ. The error is introduced because most path planners develop trajectories for the rear axle of the vehicle, not a point ϵ in front of the rear axle. The center of the back axle is usually selected as the vehicle reference point for two reasons. First, the back axle reference point corresponds to the minimum turning radius for the maximum steering angle of an Ackermann Vehicle [34]. Second, the heading of the vehicle is always aligned with the tangent direction of the path of the center of the back axle [24].

To eliminate the steady state error, the same transformation that was used to linearize the steering model in Section 3.5.1 can be used on the desired trajectory. Figure 3.10 demonstrates visually how the ϵ-Tracking Control Path is created for the ϵ-Tracking Control Point.
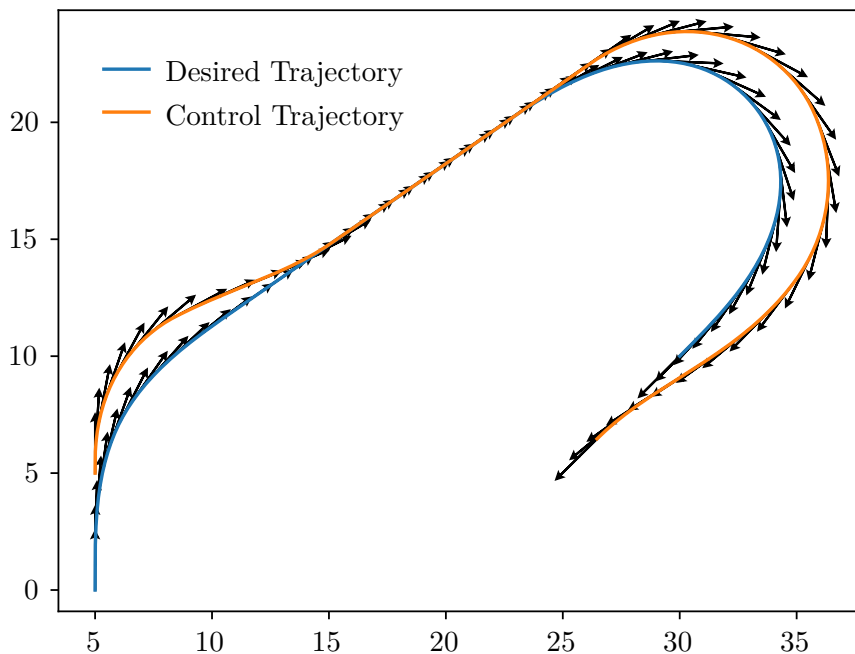
Fig. 3.10: Demonstration of the generation of a control path for the point y_ϵ from a continuous curvature path built from Clothoids, lines, and circular arcs for the infinite time horizon LQR controller. The distance of the control point y_ϵ from the back axle is $\epsilon = 5m$.

Figure 3.10 depicts that the control path always leads the reference trajectory with a distance ϵ in the direction of the CCPath heading. Generating the y_ϵ path makes the infinite horizon LQR controller derived in the Section 3.5.1 have a zero error tracking law. Additionally, because the control point y_ϵ is ϵ meters in front of the vehicle reference point, it acts as a smoothing agent when errors are generated from sensor noise.

To calculate the ϵ-Tracking Control Path, the desired trajectory must have the variables outlined in Table 3.1.

Table 3.1: Necessary trajectory variables required to build an ϵ-Tracking Control Path.

State	Description
x	x-position
y	y-position
ψ	heading
v	velocity
ω	angular velocity
a	acceleration
σ	angular acceleration

The states listed Table 3.1 for the desired trajectory are then transformed using the Equations 3.83 through 3.85 to produce a ϵ-Tracking Control Path. Because the continuous curvature path planner presented in Section 3.4 calculates every variable outlined in Table 3.1, an ϵ-Tracking Control Path can be created to produce an analytical zero-error linear control law.

3.6 Control Variation

This section proposes a method to inject white Gaussian noise into a vehicle's controller to reduce road wear while driving over dynamic charging regions. The injected noise must be carefully shaped to ensure the following criteria:

- **Position Constraint:** Position from the center of the lane δ must be less than or equal to $\delta_{\max}$ meters.

- **Acceleration Constraint:** Vehicle acceleration inputs α must be less than or equal to $\alpha_{\max}\, m/s^2$.

- **Acceleration Frequency Constraint:** Acceleration changes must be less than or equal to $f_{\alpha\max}$ Hertz.

- **Controller Constraint:** Filter must produce variations in position, velocity, and acceleration to interface with the vehicle's controller.

- **Average Charge Constraint:** Average charge q_d must be attained within a specified probability interval p.

Section 3.6.1 begins by giving an overview of the shaping filter properties and introduces challenges that arise from complying with the outlined constraints in Section 3.6.1.

Then, Section 3.6.2 outlines the numerical values calculated for $\delta_{\max}$, $\alpha_{\max}$, and $f_{\alpha\max}$ by statistically bounding their occurrence. After numerical values are set for the constraints, Section 3.6.3 characterizes relationships between $\delta_{\max}$, $\alpha_{\max}$, and $f_{\alpha\max}$ to solve for the noise shaping filter parameters.

Next, Section 3.6.4 extends Section 3.6.3 by determining the scale factor K for the injected noise based on nonlinear equations for wireless power transfer. Finally Section 3.6.5 outlines the the propagation equations for implementation and explains how to add the noise shaping filter outputs to the vehicle's control input.

3.6.1 Noise Shaping Filter

The objective of this section is to determine the appropriate form of the noise shaping filter. The block diagram for the proposed form can be seen in Figure 3.11, where α is the variation in acceleration, v is the variation in velocity, and δ is the variation from a nominal trajectory.
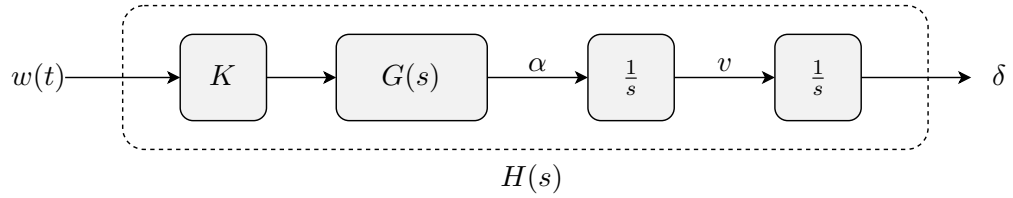
Fig. 3.11: Block diagram for the noise shaping filter $H(s)$, where $\omega(t)$, α, v, and δ are white Gaussian noise, acceleration, velocity, and position respectively.

The objective of the noise shaping filter shown in Figure 3.11 is to bound a 1-dimensional point δ driven by white Gaussian noise without violating the acceleration constraints outlined in Section 3.6. The random variable δ will be added to the control inputs to reduce road rutting, while ensuring expected charging statistics. Additionally, because the system controller accepts a trajectory with position, velocity, and acceleration (see Section 3.5), the noise shaping filter must also produce position, velocity, and acceleration outputs. The following discussion addresses why the form proposed in Figure 3.11 was proposed.

A natural approach to bound the random process δ that is not proposed in Figure 3.11 is to use a second order Markov driven by white Gaussian noise. The variance of δ becomes

$$\sigma_\delta^2 = \Psi(0) = \frac{1}{2\pi} \int_{-\infty}^{\infty} \bar{\Psi}_\delta(\omega) \, d\omega, \tag{3.100}$$

where $\bar{\Psi}_\delta(\omega)$ is the Power Spectral Density (PSD) defined by

$$\bar{\Psi}_\delta(\omega) = |G_{\text{lp}}(\omega)|^2 \, \Psi_{nn}(\omega). \tag{3.101}$$

Assuming white Gaussian noise with unity strength and a damping ratio of $\zeta = \frac{1}{\sqrt{2}}$, the Power Spectral Density of the point δ becomes

$$\bar{\Psi}_\delta(\omega) = |G_{\mathrm{lp}}(\omega)|^2 \, \Psi_{nn}(\omega) \tag{3.102}$$

$$\bar{\Psi}_\delta(\omega) = |G_{\mathrm{lp}}(\omega)|^2 \, (1) \tag{3.103}$$

$$|G_{\mathrm{lp}}(\omega)|^2 = \frac{\omega_l^4}{\omega^4 + \omega_l^4}. \tag{3.104}$$

Figure 3.12 shows the power spectral density of a second order low-pass filter with a cut-off frequency of $\omega_l = 1$ that could be used to bound δ.
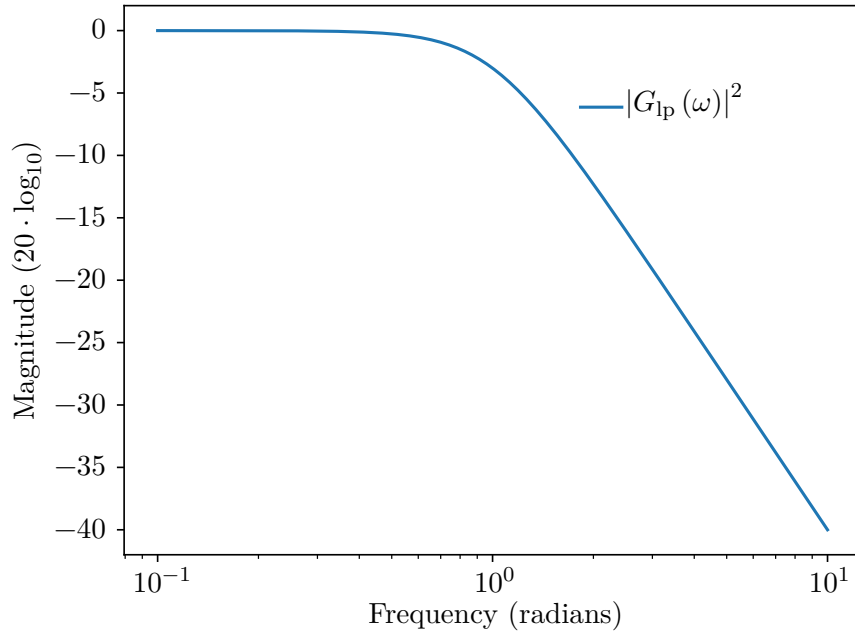
Fig. 3.12: Power spectral density for a second order low-pass filter in the frequency domain with $\omega_l = 1$ that could be used to bound variation in distance from a nominal path.

Figure 3.12 has a -40dB/dec roll-off which will cause the acceleration constraint to be violated when finding the second derivative of the system. When two derivatives of the system are taken to find the the corresponding acceleration variation α, the resulting system

magnitude squared is

$$\bar{\Psi}\left(\omega\right)_{\alpha} = \left|G_{\mathrm{lp}}\left(\omega\right)\right|^{2} = \frac{\omega_{l}^{4}\omega^{4}}{\omega^{4} + \omega_{l}^{4}}. \tag{3.105}$$

The variance of Equation 3.105 is

$$\sigma_{\alpha}^{2} = \frac{1}{2\pi}\int_{-\infty}^{\infty} \bar{\Psi}_{\alpha}\left(\omega\right)d\omega = \infty, \tag{3.106}$$

which implies that the variance of acceleration can not be have a $3\sigma_{\alpha}$ bound. Figure 3.13 displays graphically why the integral of $\bar{\Psi}_{\alpha}\left(\omega\right)$ if infinite.
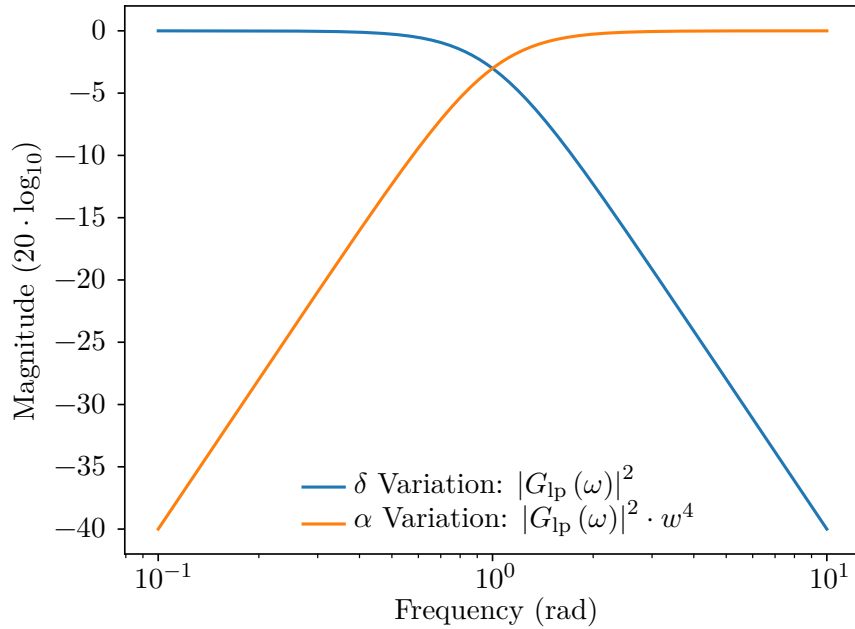
Fig. 3.13: Plot displaying that integral for the power spectral density of the magnitude squared of a second order low-pass filter differentiated two times in the frequency domain is infinite. This plot shows that a second order low-pass filter used to bound δ can not compy with acceleration constraints.

Notice in Figure 3.13 that $\left|G_{\mathrm{lp}}\left(\omega\right)\right|^{2} \cdot \omega^{4}$ does not attenuate as $\omega \to \infty$, which results in $\sigma_{\alpha}^{2} \to \infty$. Therefore, using a low-pass filter to bound δ will not meet the necessary acceleration criteria.

Instead, a feasible approach to ensure the constraints outlined in Section 3.6 is to shape

the PSD for the acceleration with a band-pass filter, then integrate the noise to find the corresponding bound for the distance σ_δ^2. Consider a band-pass filter composed of a second order low-pass filter and a second order high-pass filter. The resulting system magnitude squared is

$$|G(\omega)|^2 = \frac{\omega_l^4 \omega^4}{\left(\omega^4 + \omega_l^4\right)\left(\omega^4 + \omega_h^4\right)}.$$

(3.107)

For details on how Equation 3.107 is derived see Appendix B.3. A representation of the combined filters in the frequency domain is depicted in Figure 3.14.
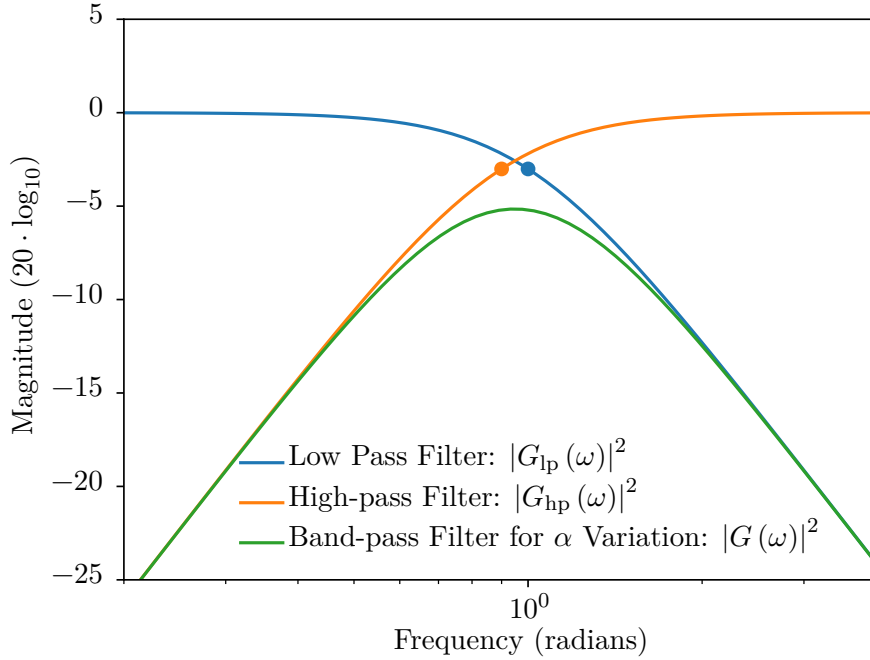
Fig. 3.14: Power spectral density of a band-pass second order filter $|G(\omega)|^2$ with $\omega_l = 1$ and $\omega_h = 0.9$ in the frequency domain. The band-pass filter $|G(\omega)|^2$ is comprised of a low-pass filter $|G_{lp}(j\omega)|^2$ multiplied by a high-pass filter $|G_{hp}(\omega)|^2$. The values for ω_l and ω_h can be selected to comply with acceleration comfort constraints.

Figure 3.14 shows that the integral of $|G(\omega)|^2$ is finite which bounds σ_α^2, and the -3dB cutoff can be set to ensure that acceleration changes are less than $f_{\alpha\max}$. Additionally, when the system is integrated twice, the resulting integral of the PSD is also finite, which allows bounds to be placed on position variance. This relationship can be seen in Figure 3.15.
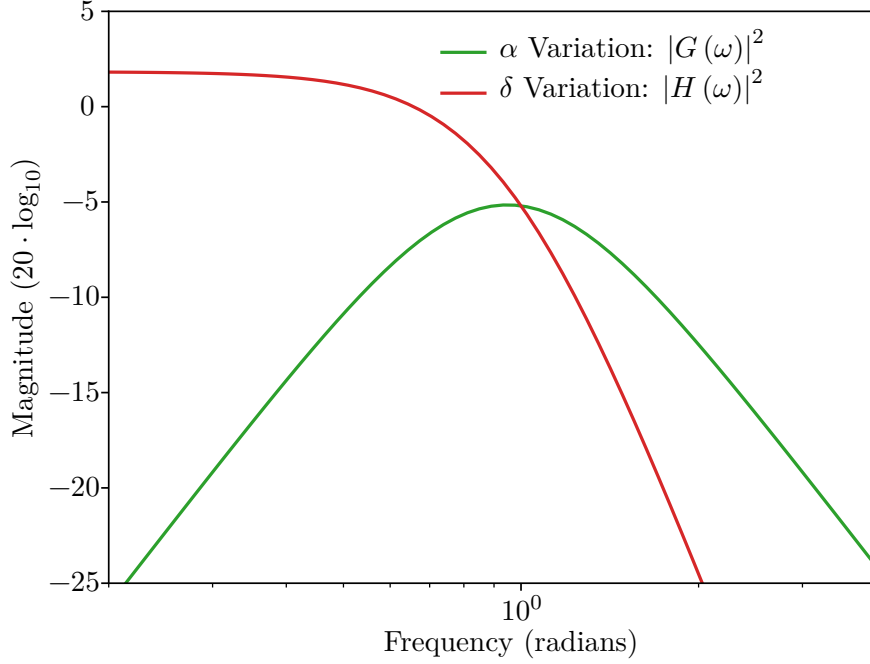
Fig. 3.15: Power spectral density (PSD) in the frequency domain of the band-pass filter $|G(\omega)|^2$ used to produce acceleration variation and its second integral $|H(\omega)|^2$ used to produce position variation. Both PSDs are finite, which implies the Noise Shaping Filter can be designed to comply with acceleration and position comfort constraints.

In Figure 3.15, the PSD of $|H(\omega)|^2$ appears to be a scaled low-pass filter, which implies that the variance of δ can be bounded. Therefore, the system can be shaped to comply with all of the constraints outlined in Section 3.6 by carefully selecting values for ω_l, ω_h, and K.

Therefore, the architecture outlined in Figure 3.11 can be used to comply with position and acceleration comfort constraints, and Equations 3.108, 3.109, and 3.110 characterize the relationship of the comfort constraints to the frequency domain of the noise shaping filter.

$$\sigma_\alpha^2 = \Psi_\alpha(0) = \frac{1}{2\pi} \int_{-\infty}^{\infty} |G(\omega)|^2 \, d\omega \tag{3.108}$$

$$\sigma_\delta^2 = \Psi_\delta(0) = \frac{1}{2\pi} \int_{-\infty}^{\infty} |H(\omega)|^2 \, d\omega \tag{3.109}$$

$$f_{\alpha\max} = |G(\omega)|_{-3\text{dB}}^2 \tag{3.110}$$

Equation 3.108 is used to bound the acceleration of the system, and Equation 3.109 is used

to bound the distance of the vehicle from the center of the trajectory. Both equations will be solved for in Section 3.6.4. Equation 3.110 is the cut-off value that ensures that the frequency changes of acceleration are not violated, and Section 3.6.3 analyses the system parameters needed to set the cut-off frequency.

3.6.2 Constraint Sizing

Section 3.6.2 addresses how the constraints on lane error, acceleration, and acceleration frequency are set. This section does not address selecting parameters for the noise shaping filter, but rather sets the bounds that the noise shaping filter must comply with.

Lane Error Constraint

The allowable error from the center of the road depends on the width and length of the vehicle, nominal heading error, and the width of the lane. For this analysis, it is assumed that the vehicle stays inside the lane if the center of the back axle is within $1.76m$ of the center of the lane. This is an estimate taken from the geometry of a Ford Focus 2012 vehicle, and a $3m$ estimated lane width.

The maximum allowable distance of the vehicle reference point from the center of the lane is

$$3/2m - 1.824/2m = 0.588\,m. \tag{3.111}$$

Therefore, the the 3σ boundary can be set to

$$3\sigma_{\delta\mathrm{max}} = 0.588\,m, \tag{3.112}$$

which implies, the maximum variance σ_δ^2 for δ is

$$\sigma_{\delta\mathrm{max}} = \frac{0.588}{3}$$
$$\sigma_{\delta\mathrm{max}}^2 = 0.3457\,m. \tag{3.113}$$

In addition to the maximum variance σ_δ^2, additional precautions should be taken to eliminate the possibility that the output of $H(s)$ is outside $3\sigma_{\max}$. This can be achieved by clamping the output of $G(s)$ to only accelerate towards the center of the lane when the vehicle is at the $3\sigma_{\delta\max}$.

Acceleration Constraint

Comfort constraints on acceleration α are bounded by the acceleration level that passengers feel discomfort. Eriksson shows that passengers feel discomfort around $1.2m/s^2$ [19]. Therefore, the acceleration can be bounded by a standard deviation of

$$3\sigma_{\alpha\max} = 1.2$$
$$\sigma_{\alpha\max} = \frac{1.2}{3}$$
$$\sigma_{\alpha\max} = .4\,m/s^2, \tag{3.114}$$

which implies that the maximum variance σ_α^2 for α is

$$\sigma_{\alpha\max}^2 = .4^2$$
$$\sigma_{\alpha\max}^2 = .16\,m/s^2. \tag{3.115}$$

When controlling the vehicle, additional measures can be taken to clamp the output of $G(s)$ to ensure that $G(s)$ does not produce system inputs that violate the $3\sigma_{\alpha\max}$ constraint if desired.

Acceleration Frequency Constraint

It is shown by Kilinc that acceleration constraints should not happen more frequently than .2Hz [20]. Therefore, the -3dB cut-off maximum of $G(s)$ is

$$f_{\alpha\max} = .2\text{Hz} \tag{3.116}$$

$$|G(\omega)|^2_{-3\text{dBmax}} = .2\text{Hz} \cdot \frac{2\pi\,\text{rad}}{\text{Hz}} \tag{3.117}$$

$$|G(\omega)|^2_{-3\text{dBmax}} = 1.2566\,\text{rad}. \tag{3.118}$$

For brevity, the -3dB cut-off maximum in radians is referred to as

$$\omega_c = 1.2566\,\text{rad}. \tag{3.119}$$

3.6.3 Solving for shaping filter parameters

Section 3.6.3 analyzes which parameters should be selected for the noise shaping filter to comply with the criteria outlined in Section 3.6. The three constraint equations for α, δ, $|G(\omega)|^2_{-3\text{dB}}$ are found in the section Relating Constraint Values, and the corresponding variables ω_l, ω_h, and K are solved for in the section Selecting ω_l and ω_h, and the section Calculating K from σ^2_δ Desired respectively.

Relating Constraint Values

Assuming that $\zeta = \frac{1}{\sqrt{2}}$, the equations that relate the system parameters to the desired constraints are

$$\sigma^2_\alpha = \frac{1}{2\pi} \int_{-\infty}^{\infty} \frac{K^2 \omega_l^4 \omega^4}{\left(\omega^4 + \omega_l^4\right)\left(\omega^4 + \omega_h^4\right)} d\omega \tag{3.120}$$

$$\sigma^2_\delta = \frac{1}{2\pi} \int_{-\infty}^{\infty} \frac{K^2 \omega_l^4}{\left(\omega^4 + \omega_l^4\right)\left(\omega^4 + \omega_h^4\right)} d\omega \tag{3.121}$$

$$\frac{1}{\sqrt{2}} = \frac{K \omega_l^2 \omega_c^2}{\sqrt{\left(\omega_c^4 + \omega_l^4\right)\left(\omega_c^4 + \omega_h^4\right)}}, \tag{3.122}$$

where ω_c is the cut-off frequency solved for in Section 3.6.2. For details regarding how each equation is derived, see Appendix B.

There are three equations (3.120, 3.121, 3.122) and three variables (ω_l, ω_h, K), which presents several approaches for selecting desired values for ω_l, ω_h, and K. One approach is to solve the indefinite integrals for σ_α^2 and σ_δ^2, then to solve for ω_l, ω_h, K. This approach proves to be non-trivial because the denominator of the integrand is an 8th order polynomial.

Another approach is to estimate the integrals for both σ_α^2 and σ_δ^2 using rectangles with corners positioned at the cutoff frequencies to simply the relationships between the three equations. This approach also proves to be non-trivial because the equation for the band-pass filter upper -3dB cutoff and the lower -3dB cutoff have an inverse relationship; this results in solving equations that have fractional order polynomials. Though the equations can be solved numerically, an additional approach is presented that yields a more exact solution.

Because the constraints are inequalities, it is not required to find a unique solution. Instead, the problem can be simplified by fixing the values of ω_l and ω_h to satisfy the cutoff frequency $f_{\alpha\text{max}}$, then scaling the incoming noise by K to meet the other system constraints. The section **Selecting ω_l and ω_h** analyzes how to select ω_l and ω_h, and the section **Calculating K from σ_δ^2 Desired** analyzes how to change K to ensure that position and acceleration constraints are not violated.

Selecting ω_l and ω_h

To begin the discussion on choosing values for ω_l and ω_h, a few properties of the band-pass filter should be analyzed. The first property, is that different values of ω_l, ω_h, and K can yield the same band-pass filter. Take for example the case when $\omega_l = \frac{\omega_h}{10}$. The band-pass filter maximum cut-off frequency is located at ω_l, and the band-pass filter minimum cut-off frequency is located at ω_h as seen in Figure 3.16 (a). In another case, if $\omega_h = \frac{\omega_l}{10}$, the same scaled band-pass filter can be created as seen in Figure 3.16 (b).
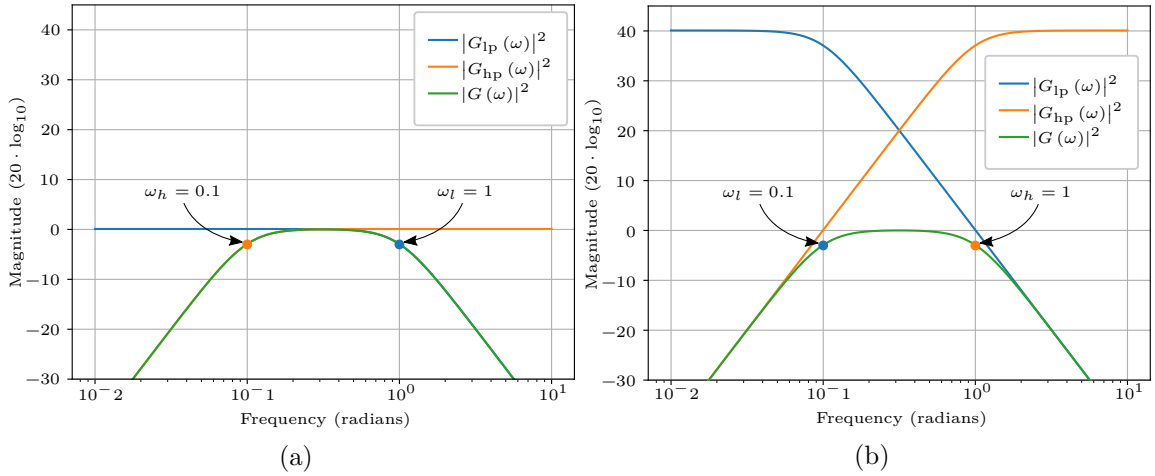
Fig. 3.16: Example plot showing that the band-pass filter does not have a unique representation when both figures are scaled by K to match highest peak magnitude. (a) Band-pass filter with $\zeta = 1/\sqrt{2}$, $\omega_l = 1$, and $\omega_h = 0.1$. (b) Band-pass filter with $\zeta = 1/\sqrt{2}$, $\omega_l = 0.1$, and $\omega_h = 1$.

Figure 3.16 shows that the band-pass filter $|G(\omega)|^2$ is not unique for values of ω_l, ω_h, and K. Therefore, only the case when $\omega_l = \kappa \omega_h$ such that $\kappa \geq 1$ will be considered for the remaining analysis.

Another notable property of the band-pass filter, is that the width of $|G(\omega)|^2$ changes the cut-off frequency for $|H(\omega)|^2$. For example, the smaller ω_h is, the lower the cut-off frequency will be for $|H(\omega)|^2$, as seen in Figure 3.17.
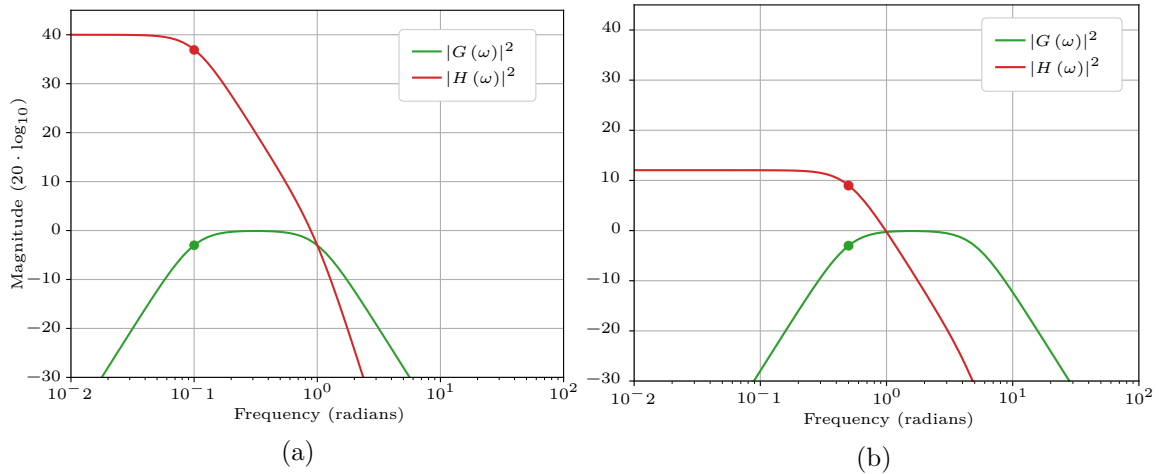
Fig. 3.17: Plot demonstrating that the cut-off frequency for $|H(\omega)|^2$ is determined by the low cut-off frequency of $|G(\omega)|^2$. (a) $|H(\omega)|^2$ cut-off frequency with $\omega_h = 0.1$. (b) $|H(\omega)|^2$ cut-off frequency with $\omega_h = 0.5$

In Figure 3.17 (a), the lower cut-off frequency of $|G(\omega)|^2$ is at 0.1 radians, and the cut-off frequency of $|H(\omega)|^2$ is correspondingly at 0.1 radians. In Figure 3.17 (b), the cut-off frequency of $|H(\omega)|^2$ is also determined by the lower cut-off frequency of $|G(\omega)|^2$. Figure 3.17 shows that the larger the width of the band-pass filter $|G(\omega)|^2$, the slower the frequency changes of $|H(\omega)|^2$.

Therefore, with a fixed ω_l the maximum cut-off frequency of $|H(\omega)|^2$ is obtained when $\omega_h = \omega_l$. However, there exists a trade-off for minimizing the pass-band filter. A narrower pass-band results in a noise pattern that tends towards oscillatory accelerations with a frequency at ω_l, which may be an undesirable side-effect. Because the noise filter variation is both within project constraints and maximizes cut-off frequency of $|H(\omega)|^2$, the testing and results assumes $\omega_l = \omega_h$. With the bass-band width set, the selection of ω_l will now be analyzed.

The parameter ω_l should be selected such that the -3dB upper cut-off frequency of $|G(\omega)|^2$ occurs at ω_c—the cut-off frequency solved for in Section 3.6.2. Give a desired ω_c,

the equation to solve for ω_l when $\omega_h = \kappa\omega_l$ is

$$\omega_l = \left(-\sqrt{-\frac{\omega_c^8}{\kappa^4} + \frac{1}{4}\Omega^2} - \frac{1}{2}\Omega\right)^{1/4}, \tag{3.123}$$

where

$$\Omega = \omega_c^4\left(1 + \frac{1}{\kappa^4} - \frac{\left(\alpha^2 + 1\right)^2}{\kappa^4\rho^2}\right), \tag{3.124}$$

and ρ is the desired attenuation at ω_c. For details regarding the derivation of the -3dB cutoff, see Appendix B.3.

Calculating K from σ_δ^2 Desired

As was discussed in Section 3.6.3, the integral values for σ_δ^2 and σ_α^2 are difficult to relate when trying to solve for K, ω_l, and ω_h. However, with ω_l and ω_h fixed, the relationship between σ_δ^2 and σ_α^2 can be easily computed using K. By numerically computing σ_δ^2 and σ_α^2, there exists a quadratic relationship that for both σ_δ^2 and σ_α^2 based on K. Figure 3.18 shows the relationship between σ_δ^2 and σ_α^2 as a function of K when $\omega_l = \omega_h = 0.81\,\text{rad}$, $\sigma_{\delta\text{max}}^2 = 0.34$, and $\sigma_{\alpha\text{max}}^2 = 0.16$
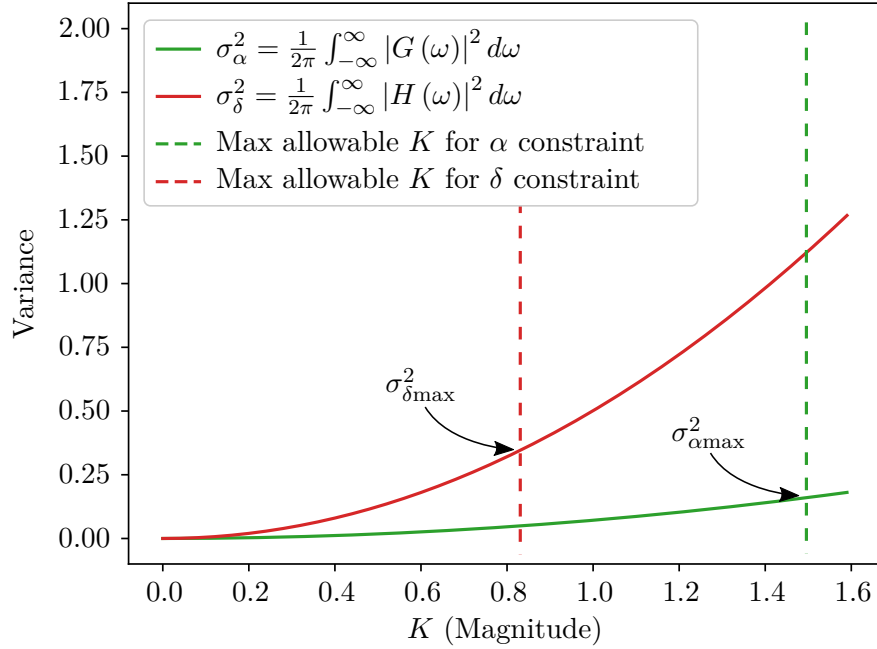
Fig. 3.18: Plot relating the maximum allowable K when $\omega_l = \omega_h = 0.81$ radians based on the maximum computed values for $\sigma_{\delta\max}^2 = 0.34$ and $\sigma_{\alpha\max}^2 = 0.16$. The maximum allowable K value is $K = 0.83$ because that is the first value of K that violates a system constraint.

Figure 3.18 shows that the value $\sigma_{\delta\max}^2$ calculated in Section 3.6.2 occurs at a lower value of K than $\sigma_{\alpha\max}^2$. Therefore, the maximum value of K is bounded by $\sigma_{\delta\max}^2$.

The quadratic equations in Figure 3.18 that are fit to σ_δ^2 and σ_α^2 are

$$\sigma_\delta^2 = 0.5012K^2 \tag{3.125}$$

$$\sigma_\alpha^2 = 0.0715K^2, \tag{3.126}$$

and the maximum value of K for the configuration of ω_l and ω_h is,

$$K_{\max} = \sqrt{\sigma_{\delta\max}^2/0.5012} = 0.83. \tag{3.127}$$

With the selection that $\omega_l = \omega_h = 0.81\,\mathrm{rad}$, any desired σ_δ^2 can be selected within $\sigma_{\delta\max}^2$. If however, the allowable $\sigma_{\delta\max}^2$ is limited by $\sigma_{\alpha\max}^2$, then the pass-band width must be increased to allow larger values of σ_δ^2 at the cost of reducing the cutoff frequency for $|H(\omega)|^2$.

This analysis shows that a desired scale factor K can be selected that complies with all comfort comfort constraints outlined in Section 3.6.

3.6.4 Calculating Noise Scaling Size K Based on a Desired Charge q_d and a Probability Interval p

Section 3.6.3 shows that a quadratic relationship exists which relates the variation from the center of the lane δ to the scaling coefficient K. However, to comply with the charging constraints outlined in Section 3.6, a relationship must be found between the average charge of the vehicle's battery q as a function of K with an associated standard deviation.

If the battery charging profile were linear, the relationship between q and K could be found as a function of δ, and the analysis from Section 3.6.3 could be utilized for charging. Because the charging profile is a two-sided Sigmoid function as proposed in Section 3.3.2, sample-based statistical methods must be employed to handle the nonlinear charging profile..

The nonlinear function that relates charge q to K is addressed in Section 3.6.4, and Section 3.6.4 analyzes how to achieve a desired charge within a specified probability interval.

Finding the Nonlinear Charging Profile

To find a nonlinear function that relates average desired charge q_d and the noise scaling coefficient K, a Monte Carlo simulation of 250 runs was performed for incremental values of K on a straight charging path of 200 meters. The Full Charge Region width was set to $.4\,m$ and the Transition Charge Region width was set to $.2\,m$. The results for the average expected charge and standard deviation can be seen in Figure 3.19 (a) and (b) respectively.
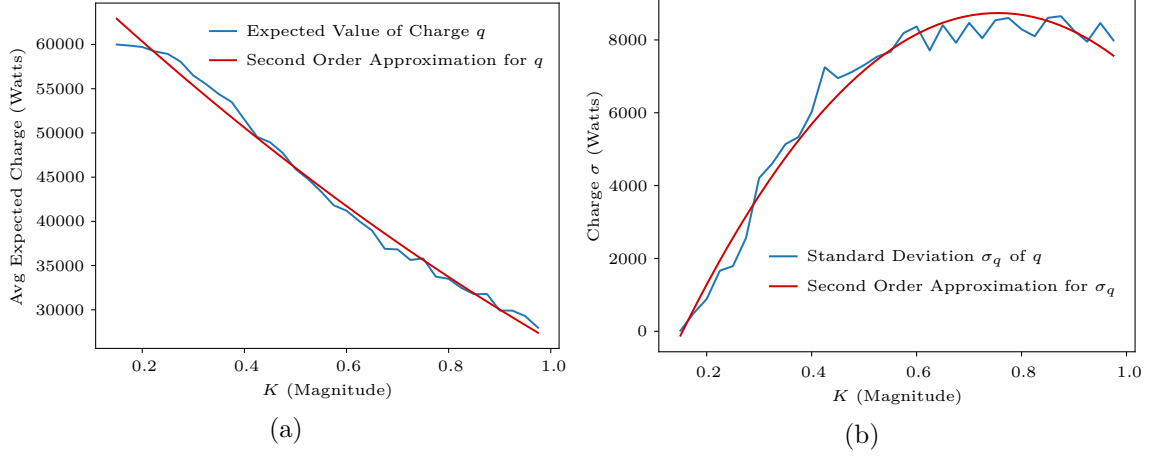
Fig. 3.19: Nonlinear approximation of charge and standard deviation fitted with second order polynomials taken from a Monte Carlo Simulation of 250 runs on a straight charging path of 200 meters. (a) Nonlinear approximation for the expected value of charge fitted with a second order polynomial. (b) Nonlinear approximation for the standard deviation of expected charge fitted with a second order polynomial.

As seen in Figure 3.19 the average expected charge based on K and its standard deviation can both be approximated by second order polynomials. The polynomial equation for the average expected charge q_e is

$$q_e = a_\mu K^2 + b_\mu K + c_\mu \tag{3.128}$$

$$q_e = 10796.0K^2 - 55177.8K + 70945.6, \tag{3.129}$$

and the polynomial equation for the standard deviation of the expected charge average σ_{q_e} is

$$\sigma_{q_e} = a_\sigma K^2 + b_\sigma K + c_\sigma \tag{3.130}$$

$$\sigma_{q_e} = -24195.9K^2 + 36538.7K - 5055.5. \tag{3.131}$$

Equation 3.130 can be extended to be the equation of any desired z-score (standard deviation from the mean) by multiplying the equation by the desired z-score

$$z_{\sigma q_e} = z\left(a_\sigma K^2 + b_\sigma K + c_\sigma\right) \tag{3.132}$$

Calculating K from the Nonlinear Charging Profile and Probability Interval

This section uses nonlinear charging equations to find the average expected charge as a function of K with an associated standard deviation. The standard deviation can be used to specify the likelihood of achieving a desired average expected charge q_d with probability p, where p is the upper tail integral of the z-score. The function for the z-score boundary that returns the desired charge with a desired probability q_{dp} is

$$q_{dp} = (a_\mu - za_\sigma)\, K^2 + (b_\mu - zb_\sigma)\, K + (c_\mu - zc_\sigma)\,, \tag{3.133}$$

where the variables for Equation 3.133 are specified in the previous section. The corresponding K value can be solved for by completing the square. The desired K value is

$$K = -\sqrt{\frac{q_{dp} - (c_\mu - zc_\sigma)}{(a_\mu - za_\sigma)} + \frac{1}{4}\frac{(b_\mu - zb_\sigma)^2}{(a_\mu - za_\sigma)^2}} - \frac{1}{2}\frac{(b_\mu - zb_\sigma)}{(a_\mu - za_\sigma)}. \tag{3.134}$$

For example, if a vehicle desires to receive an average charge of $q_d = 40\text{kW}$ with 97% probability, a z-score of 1.88 can be selected, which corresponds to a .97 upper tail integral amount of the Cumulative Distribution Function. To relate the z-score to the actual problem, the equation for the z-score line can be plotted with the average expected charge, as seen in Figure 3.20.
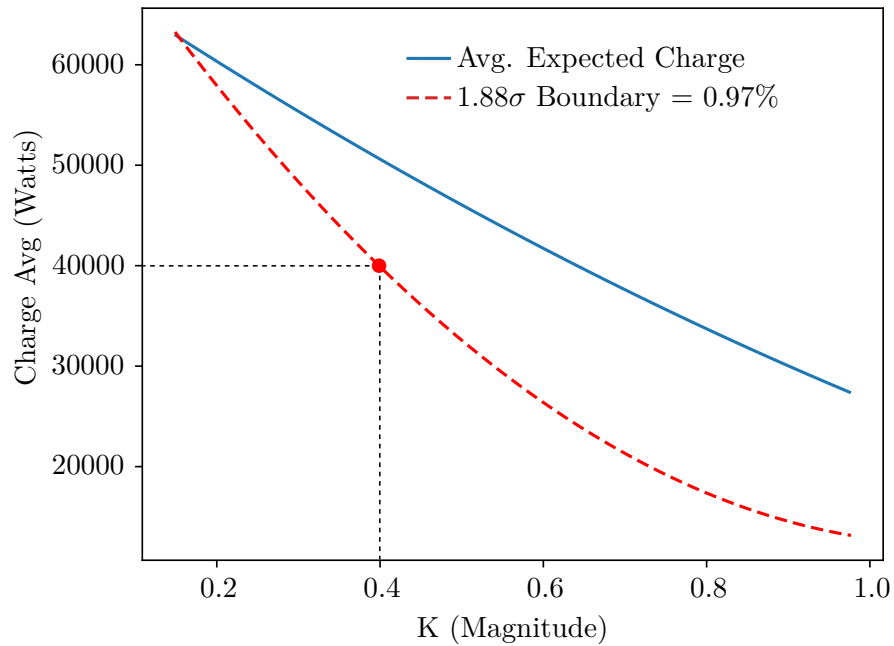
Fig. 3.20: Example plot for finding a K value that yeilds an expected charge $q_d = 40$kW with a probability of $p = 0.97$. The red-dotted line represents 1.88 standard deviations from average charge, which cooresponds to a 97% upper tail probility interval.

As seen in Figure 3.20, to obtain an average expected charge of 40kW, a value of $K \approx 4.0$ should be selected.

3.6.5 Implementing Noise Shaping Filter

For the noise shaping filter to be implemented in real time, the state space equations are developed in the section Propagation Equations for the Noise Shaping Filter. Next, the section Adding Variation from the Noise Shaping Filter to a Desired Trajectory explores how the states from the shaping filter are incorporated into the vehicle's trajectory.

Propagation Equations for the Noise Shaping Filter

The noise shaping filter can be put into standard canonical form by first grouping s terms in the Laplace domain. The system $G(s)$ becomes

$$G(s) = \frac{K\omega_l^2 s^2}{s^4 + (2\omega_h\zeta + 2\omega_l\zeta) s^3 + (\omega_h^2 + 4\omega_h\omega_l\zeta^2 + \omega_l^2) s^2 + (2\omega_h^2\omega_l + 2\omega_h\omega_l^2) s + \omega_h^2\omega_l^2}.$$

(3.135)

Making the following substitutions

$$a_1 = 2\omega_h\zeta + 2\omega_l\zeta \tag{3.136}$$

$$a_2 = \omega_h^2 + 4\omega_h\omega_l\zeta^2 + \omega_l^2 \tag{3.137}$$

$$a_3 = 2\omega_h^2\omega_l + 2\omega_h\omega_l^2 \tag{3.138}$$

$$a_4 = \omega_h^2\omega_l^2 \tag{3.139}$$

$$b = \omega_l^2, \tag{3.140}$$

allows Equation 3.135 to be put into Controllable Canonical Form where

$$\mathbf{A} = \begin{bmatrix} 0 & 1 & 0 & 0 \\ 0 & 0 & 1 & 0 \\ 0 & 0 & 0 & 1 \\ -a_4 & -a_3 & -a_2 & -a_1 \end{bmatrix} \tag{3.141}$$

$$\mathbf{B} = \begin{bmatrix} 0 \\ 0 \\ 0 \\ 1 \end{bmatrix} \tag{3.142}$$

$$\mathbf{C}_\alpha = \begin{bmatrix} 0 & 0 & Kb & 0 \end{bmatrix} \tag{3.143}$$

$$\mathbf{D} = \mathbf{0}. \tag{3.144}$$

Equations 3.141 through 3.144 form the state space matrices to return acceleration variation α from the noise shaping filter. To find velocity variations v from the noise shaping filter, make the following substitution for $\mathbf{C}$,

$$\mathbf{C}_v = \left[\begin{array}{cccc} 0 & Kb & 0 & 0 \end{array}\right]. \tag{3.145}$$

To find position variations α from the noise shaping filter, make the following substitution to $\mathbf{C}$,

$$\mathbf{C}_\delta = \left[\begin{array}{cccc} Kb & 0 & 0 & 0 \end{array}\right]. \tag{3.146}$$

Adding Variation from the Noise Shaping Filter to a Desired Trajectory

When a trajectory is built in compliance with the path planner analyzed in Section 3.4 and the linear feedback controller in Section 3.5, every time step in the trajectory has a valid position, velocity, and acceleration input for a 2-dimensional point. The variation from the noise shaping filter must have corresponding states that are added to the desired trajectory as seen in Figure 3.21.
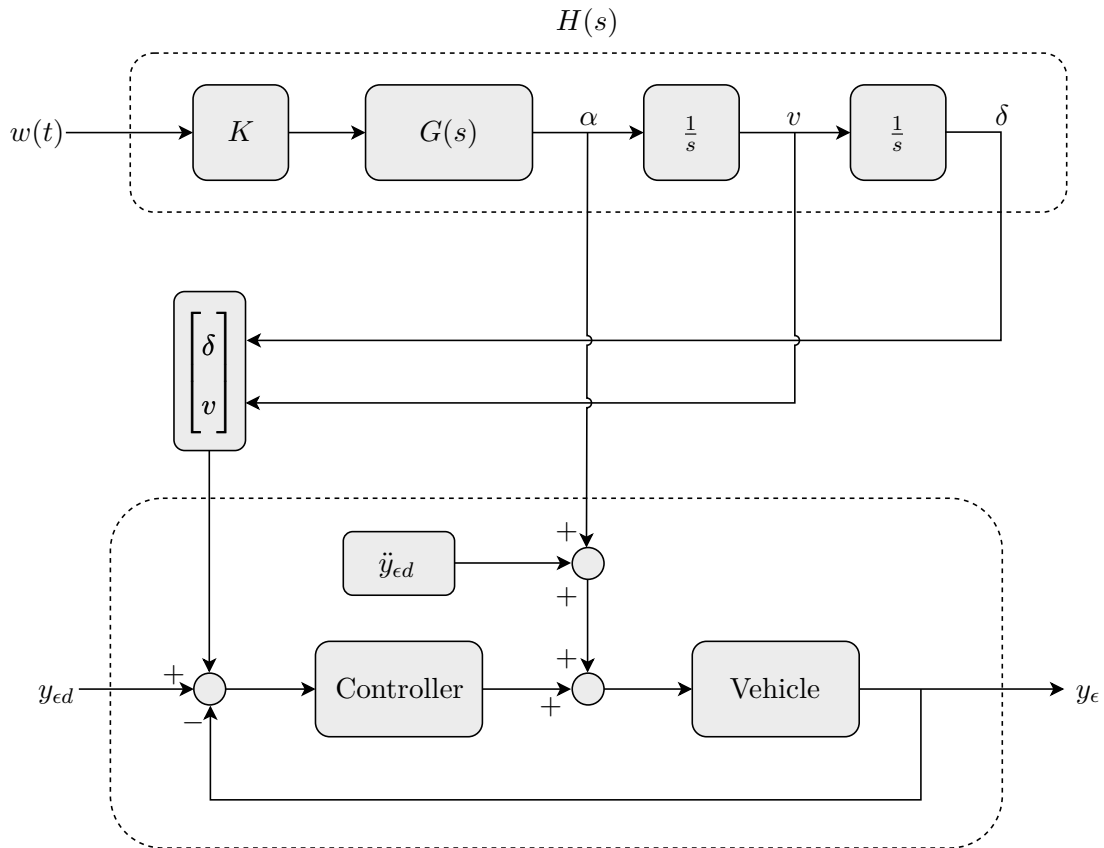
Fig. 3.21: Block diagram depicting how the noise shaping filter output is incorporated into the vehicle control input.

In Figure 3.21 it can be seen how the output of the noise shaping filter is to be added to the controller trajectory. However, the output of noise shaping filter is 1-dimensional for each states, where-as the input to the controller requires a 2-dimensinoal trajectory. Therefore, the noise shaping filter outputs must be transformed into the trajectory reference frame.

The heading at each point on the desired trajectory can be used as the x-axis of the reference frame, and the states from the noise shaping filter can be added in the y-axis direction.

Therefore, given a 1-dimensional position error x_{error}, the orthogonal position to the reference frame point p_r can be calculated by rotating the vector $\begin{bmatrix} x_{\text{error}} & 0 \end{bmatrix}^T$ by $\theta_{\text{ref}} + \frac{\pi}{2}$.

The new point with added variation p_v is

$$p_v = p_r + R\left(\theta_{\text{ref}} + \frac{\pi}{2}\right)\begin{bmatrix} x_{\text{error}} \\ 0 \end{bmatrix} \tag{3.147}$$

$$\begin{bmatrix} x_v \\ y_v \end{bmatrix} = p_r + \begin{bmatrix} \cos\theta_{\text{ref}} & -\sin\theta_{\text{ref}} \\ \sin\theta_{\text{ref}} & \cos\theta_{\text{ref}} \end{bmatrix}\begin{bmatrix} x_{\text{error}} \\ 0 \end{bmatrix} \tag{3.148}$$

$$\begin{bmatrix} x_v \\ y_v \end{bmatrix} = p_r + \begin{bmatrix} x_{\text{error}}\cos\theta_{\text{ref}} \\ x_{\text{error}}\sin\theta_{\text{ref}} \end{bmatrix} \tag{3.149}$$

$$\begin{bmatrix} x_v \\ y_v \end{bmatrix} = p_r + x_{\text{error}}\begin{bmatrix} \cos\theta_{\text{ref}} \\ \sin\theta_{\text{ref}} \end{bmatrix}. \tag{3.150}$$

The same approach can be used to transform α and v into the reference frame, and the variation from the noise shaping filter can be added to the desired trajectory as seen in Figure 3.21.

CHAPTER 4

RESULTS AND ANALYSIS

The contribution of this Chapter 4 is to validate the proposed theory in Chapter 3 through simulations. The end of each section addresses any unexpected results and presents a corresponding anlysis.

4.1   Extended Kalman Filter Results

The purpose of this section is to ensure that the EKF designed in Section 3.2 was implemented correctly. Section 4.1.1 outlines the parameters used for all simulation results, and the remaining sections verify the corresponding analysis outlined in Section 3.2.

4.1.1   Simulation Parameters

The purpose of this section is to outline simulation parameters utilized for testing purposes. Any deviations from the parameter tables listed below, will be specified in the corresponding section.

Process noise parameters are presented in Table 4.1.

Table 4.1: Process noise covariance parameters used for the state propagation results for the Extended Kalman Filter.

Parameter	Value
Q_v	$0.025\,m^2/s$
Q_ϕ	$6.85e^{-8}\,rad^2 \cdot s$
Q_{bv}	$0.0002\,m^2/s$
$Q_{b\phi}$	$0.00002\,rad^2 \cdot s$
$\sigma_{v,ss}$	$.1\,m/s$
$\sigma_{\phi,ss}$	$0.0349\,rad/s$
Noise Scaling	$\sqrt{Q/dt}$

Discrete measurement parameters are specified in Table tab:covUpdateMeasurementUpdate. The reason the noise variance for the discrete x and y position updates is within centimeters is because the use of an RTK GPS is assumed.

Table 4.2: Measurement noise covariance parameters used for state and covariance update verification.

Parameter	Value
$R_{\mathrm{gps\_}x_1}$	$0.03^2\,m^2$
$R_{\mathrm{gps\_}x_2}$	$0.03^2\,m^2$

Initial covariance conditions are seen in Table 4.3.

Table 4.3: Initial covariance conditions for GPS sensor, steering angle sensor, and velocity sensor for the Extended Kalman Filter Verifications

Parameter	Value
$x_{1\sigma}$	$R_{\text{gps}\_x_1}$
$x_{2\sigma}$	$R_{\text{gps}\_x_2}$
ψ_σ	0.0175 rad
$b_{v\sigma}$	$\sigma_{v,ss}$
$b_{\phi\sigma}$	$\sigma_{\phi,ss}$

Applicable simulation run-time parameters are in Table 4.4.

Table 4.4: Run-time paramaters for the Extended Kalman Filter Monte Carlo simulation verifications.

Parameter	Value
Integrator	Runge-Kutta45
Start Time	0
End Time	10
Time Step (dt)	0.01
Monte Carlo Runs	100
Discrete GPS Update	5 Hz

Initial vehicle conditions are seen in Table 4.5.

Table 4.5: Vehicle's initial parameters and conditions for the Extended Kalman Filter verifications.

Parameter	Value
Steering Angle (θ) Limit	$0.5236\,rad$
$\dot{\theta}$ Limit	$1.5708\,rad/sec$
Wheel Base L	$3\,m$
GPS Lever Arm Length L_{ref}	$1.5\,m$
Position x	$0\,m$
Position y	$0\,m$
Initial heading ψ	$0\,rad$
Initial steering angle ϕ	$.2\,rad$
Initial velocity v	$5\,m/s$
Initial velocity sensor time const τ_v	$100\,s$
Initial angle sensor time const τ_ϕ	$100\,s$

4.1.2 State Propagation Results

This section verifies the correct state propagation of the EKF (Extended Kalman Filter). All noise values were set to zero, and the error of each state was plotted in time. Figure 4.1 shows the error of each state between the navigation model and truth model.
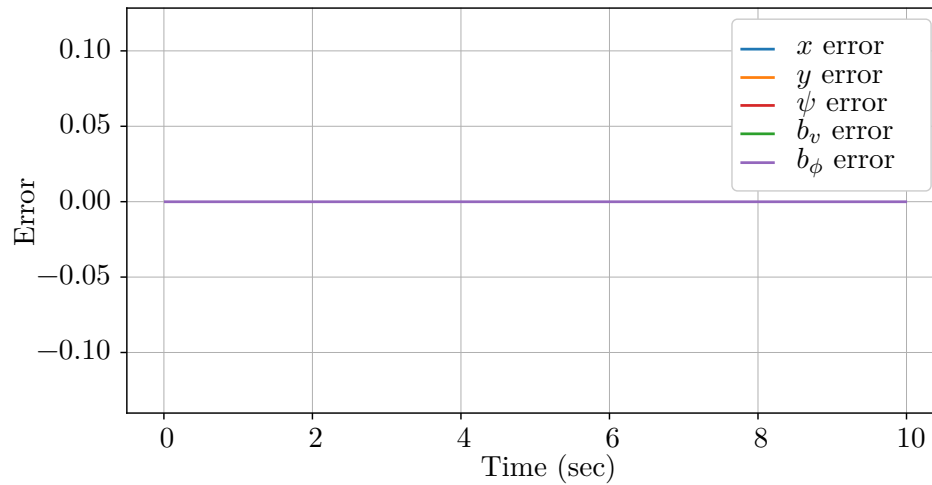
Fig. 4.1: Plot verifying the accurate state propagation between the Estimated Kalman Filter and the truth model with zero noise. Plot returns zero error for all states which verifies the correct state propagation of the Navigation Filter.

Figure 4.1 verifies that each state between the EKF and the truth state has zero error, which indicates the accurate propagation of the estimated navigation filter with to the truth model.

4.1.3 Process Noise Results

This section verifies that the process noise of the EKF is propagated correctly. To verify the process noise, a Monte Carlo run of 100 iterations was performed with the discrete update turned off. The results can be seen for each state in Figures 4.2—4.6. Because the estimated covariance matches the simulated covariance for every state, the EKF is updating the process noise covariance correctly.
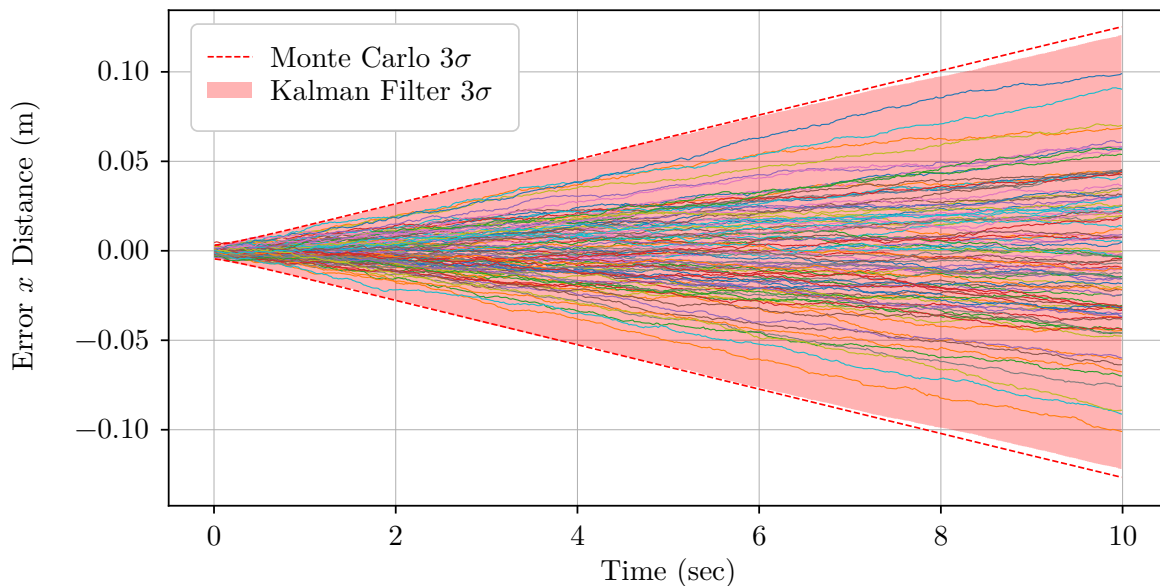
Fig. 4.2: Error plot for the x position state verifying the 3σ Extended Kalman Filter propagation compares to the true Monte Carlo 3σ boundary. The plot verifies the correct propagation covariance update for the Extended Kalman Filter.
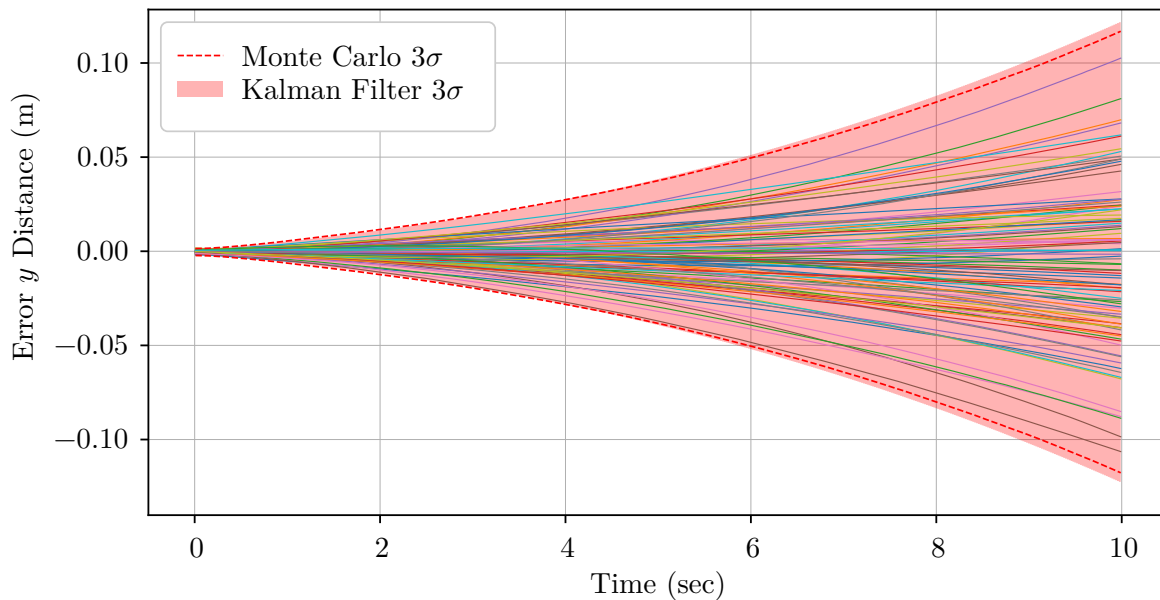
Fig. 4.3: Error plot for the y position state verifying the 3σ Extended Kalman Filter propagation compares to the true Monte Carlo 3σ boundary. The plot verifies the correct propagation covariance update for the Extended Kalman Filter.
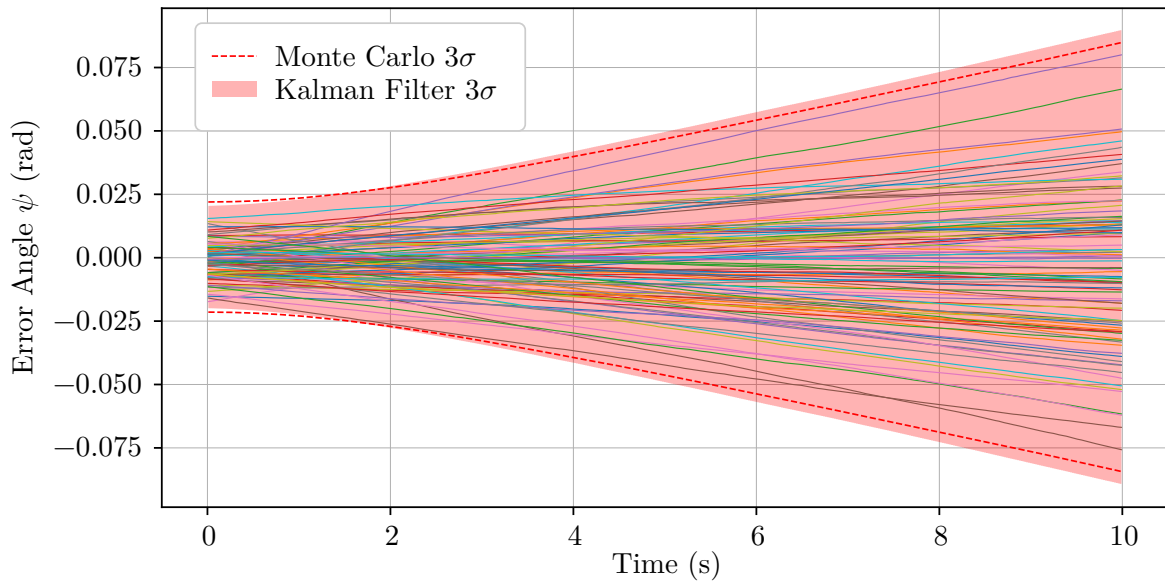
Fig. 4.4: Error plot for the heading ψ state verifying the 3σ Extended Kalman Filter propagation compares to the true Monte Carlo 3σ boundary. The plot verifies the correct propagation covariance update for the Extended Kalman Filter.
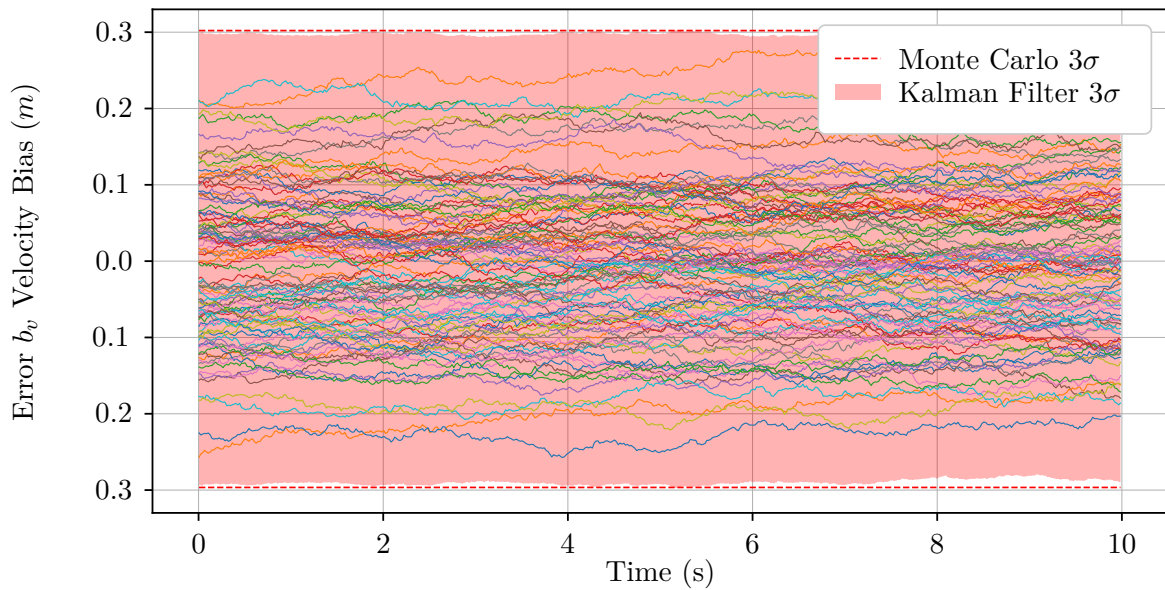
Fig. 4.5: Error plot verifying that the velocity angle sensor bias b_v 3σ Extended Kalman Filter propagation compares to the true Monte Carlo 3σ boundary. The plot verifies the correct propagation covariance update for the Extended Kalman Filter.
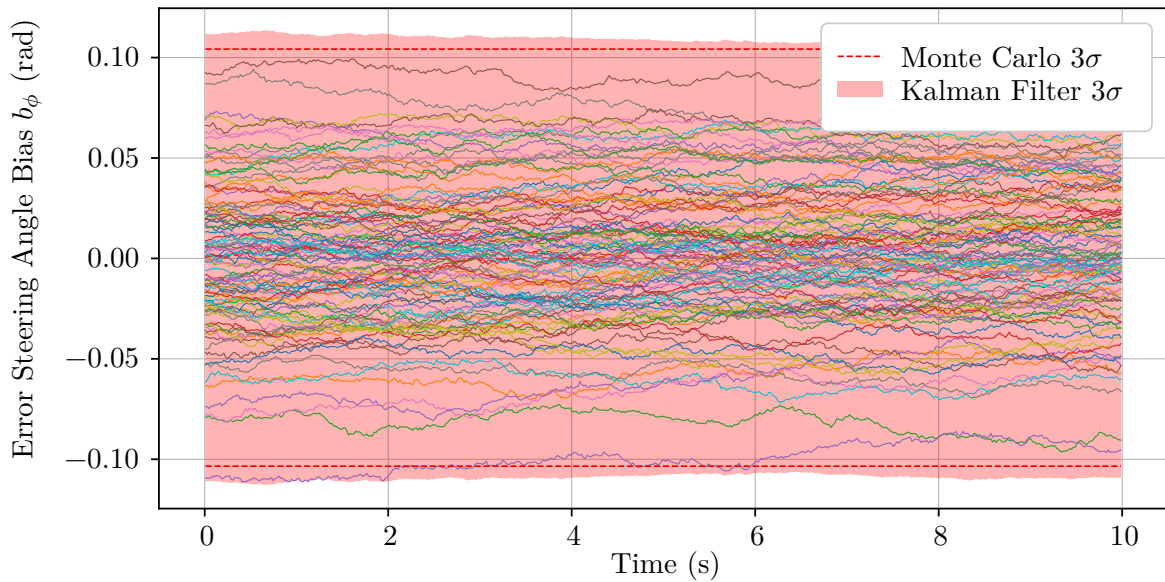
Fig. 4.6: Error plot for verifying that the steering angle sensor bias b_ϕ 3σ Extended Kalman Filter propagation compares to the true Monte Carlo 3σ boundary. The plot verifies the correct propagation covariance update for the Extended Kalman Filter.

4.1.4 State and Covariance Update Verification

The purpose of this section is to verify that the state and covariance update steps were implemented properly. To verify the update step, a Monte Carlo run with 100 simulations was performed for 10 seconds, and the Kalman Filter covariance limits were verified.

Figures 4.7—4.11 show that all of the estimated states are near the 3σ boundaries of the Kalman Filter's Covariance prediction. The red dotted line is the calculated 3σ prediction from the Kalman Filter, and the red filled region is the true 3σ value for each ensemble. Because all states are within the Kalman Filter 3σ prediction, the state and covariance update steps are valid.
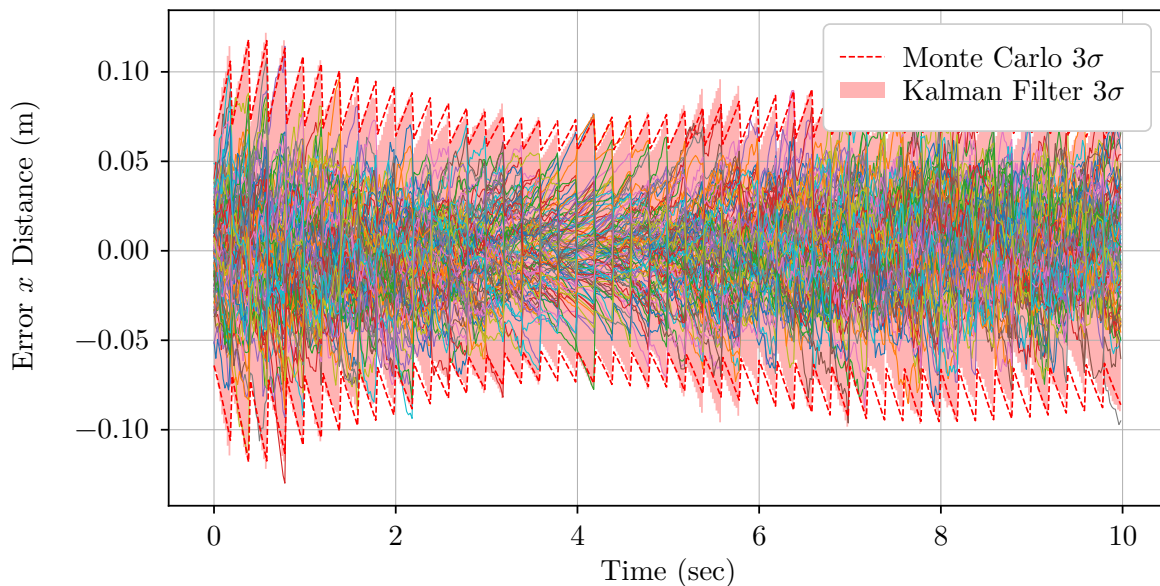
Fig. 4.7: Error plot for the vehicle x position verifying the 3σ Extended Kalman Filter covariance 3σ propagation compares to the true Monte Carlo 3σ boundary. The plot verifies the correct covariance update for the Extended Kalman Filter.
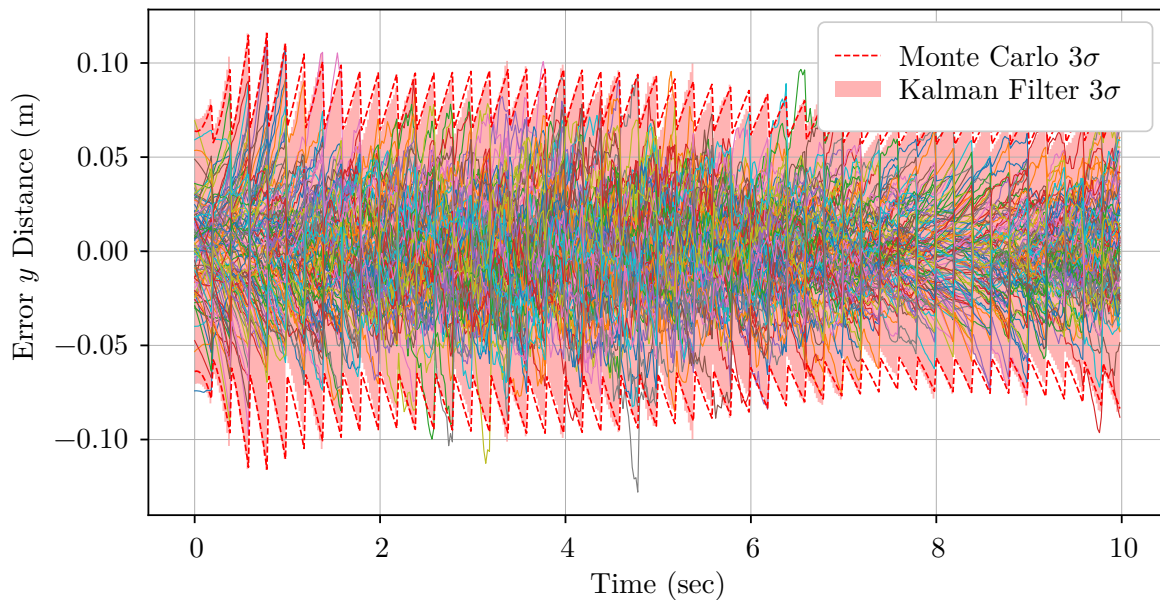
Fig. 4.8: Error plot for the vehicle y position verifying the 3σ Extended Kalman Filter covariance 3σ propagation compares to the true Monte Carlo 3σ boundary. The plot verifies the correct covariance update for the Extended Kalman Filter.
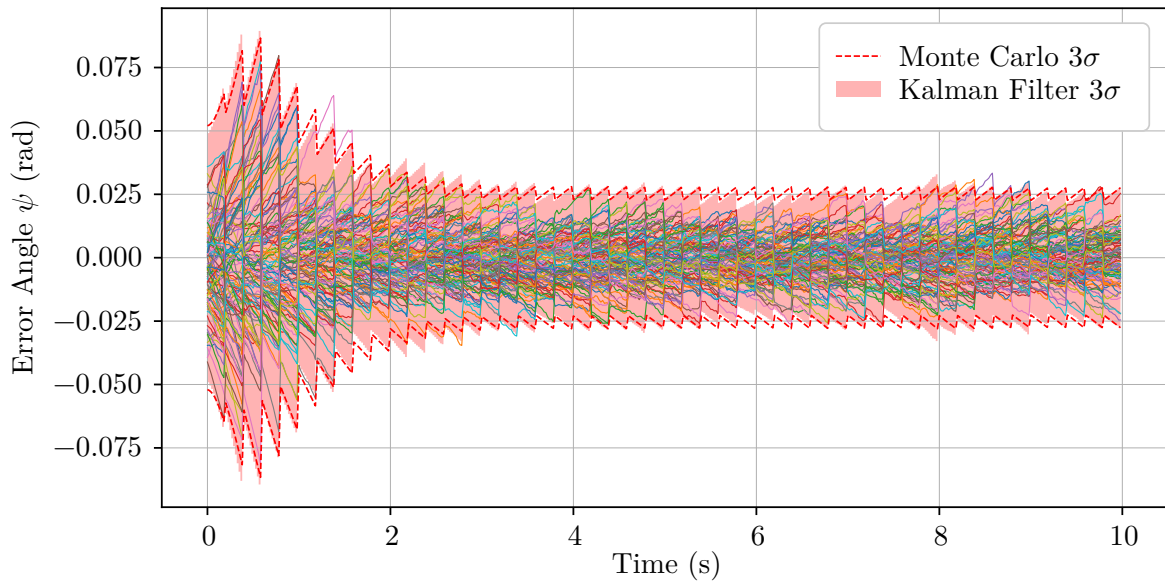
Fig. 4.9: Error plot for the vehicle heading state verifying the 3σ Extended Kalman Filter covariance 3σ propagation compares to the true Monte Carlo 3σ boundary. The plot verifies the correct covariance update for the Extended Kalman Filter.
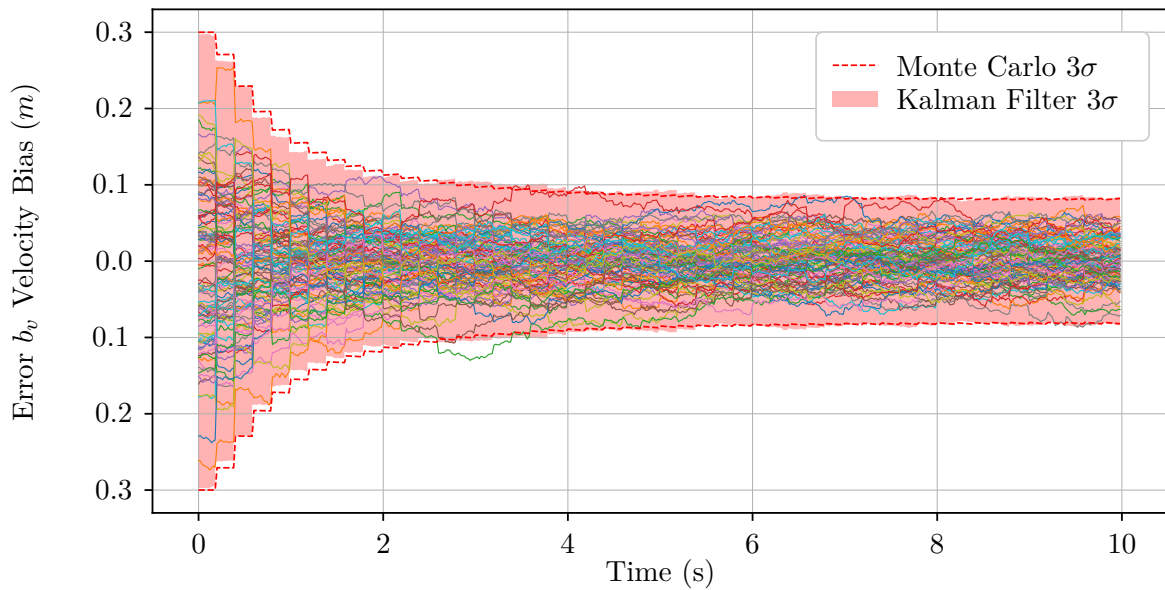
Fig. 4.10: Error plot for the velocity sensor bias state verifying the 3σ Extended Kalman Filter covariance 3σ propagation compares to the true Monte Carlo 3σ boundary. The plot verifies the correct covariance update for the Extended Kalman Filter.
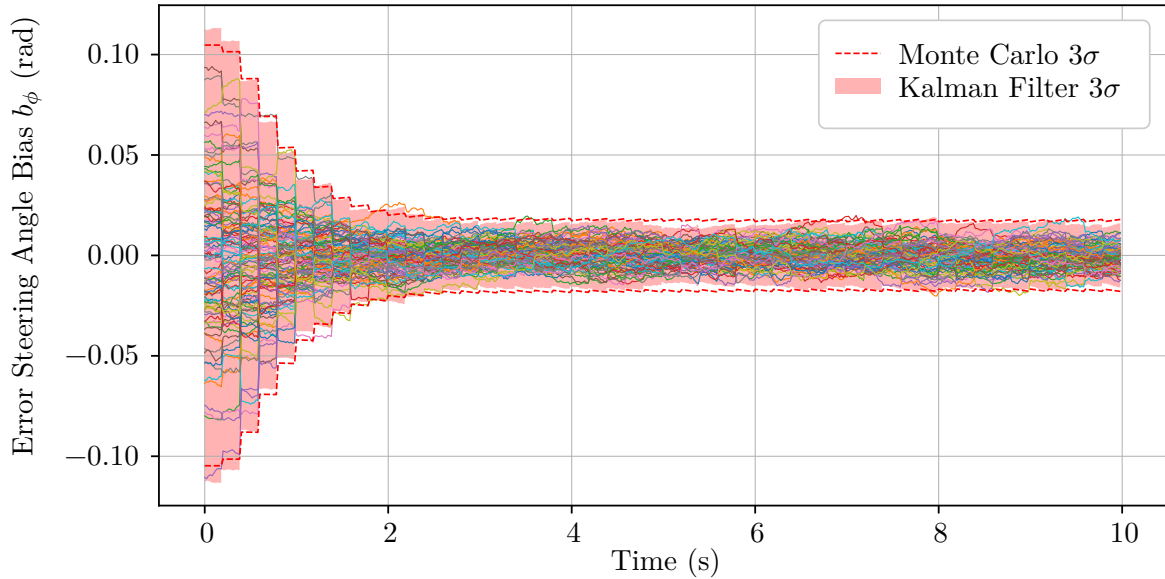
Fig. 4.11: Error plot for the steering angle sensor bias state verifying the 3σ Extended Kalman Filter covariance 3σ propagation compares to the true Monte Carlo 3σ boundary. The plot verifies the correct covariance update for the Extended Kalman Filter.

4.1.5 Residual Verification

This section validates the residual of the incoming discrete measurements. The residual is the difference between the expected measurement and actual measurement. It is calculated by

$$\left(\underline{\tilde{z}}\left[k \right] - \underline{\hat{\tilde{z}}}\left[k \right] \right). \tag{4.1}$$

The covariance of the residual is equal to

$$\mathbf{HPH}^T + \mathbf{R}. \tag{4.2}$$

To verify if the residual values are correct, a hair plot of the residuals during the discrete updates can be seen in Figure 4.12, where the red dotted line is the 3σ value of the residual calculated by the Kalman Filter using Equation 4.2. Note that the 3σ value captures an

expected number of incoming measurements.
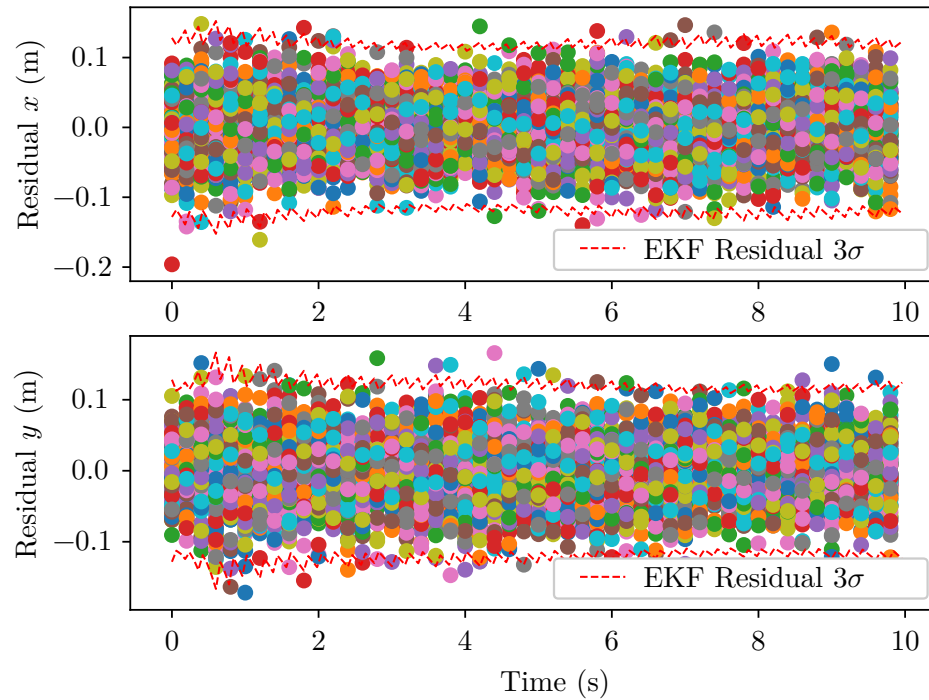
Fig. 4.12: Residual plots for the discrete GPS measurements on both x and y position. The plot verifies that the residuals are within the Extended Kalman Filter's 3σ prediction.

The mean of the residual at each ensemble can be seen in Figure 4.13. The residual should near zero mean as the number of simulations is increased, and Figure 4.13 shows that the expected value of the GPS measurement residual is tending towards zero.
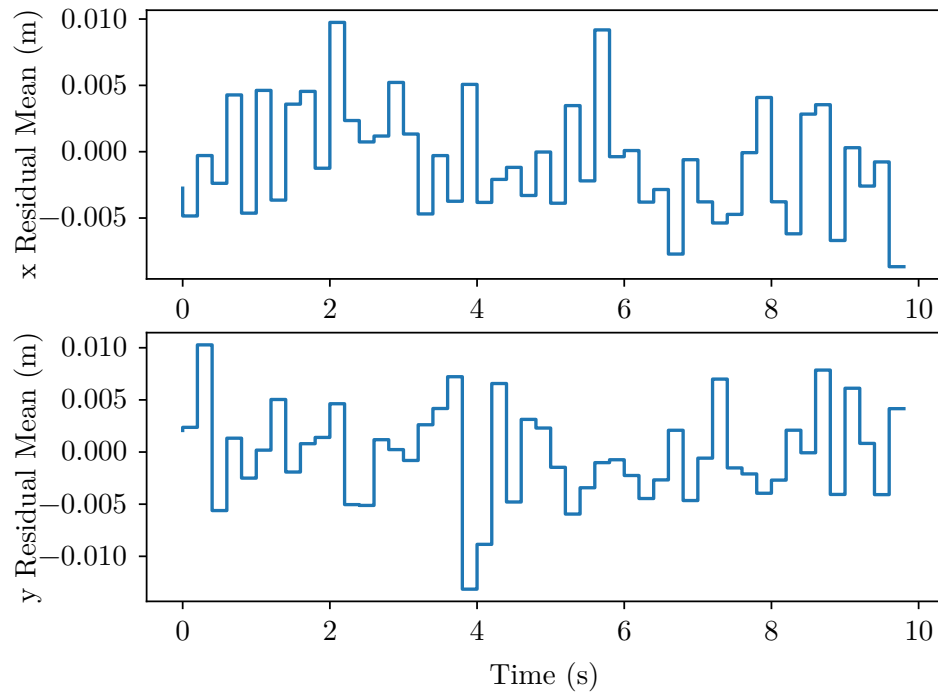
Fig. 4.13: Plot verifying that the ensemble expected value of the residual. The plot verifies the the residual property that the mean of the residual tends tends towards zero as the number of simulations is increased.

Because Figure 4.12 shows a valid number of residuals captured inside the 3σ boundary, and because the residual mean is zero, the implementation of the discrete update is correct.

4.2 State of Charge Results

The purpose of this section is compare the proposed state of charge model developed in Section 3.3 to known results. To test the results, an aggressive acceleration profile and a long distance highway driving profile were used as benchmarks. Section 4.2.1 addresses the aggressive acceleration profile of driving 0 to 60 miles per hour in 10 seconds, and Section 4.2.2 tests how many kilometers a vehicle can drive on a full charge.

4.2.1 Simulated Aggressive Acceleration Results

To verify the state of charge estimates during an acceleration period, the vehicle profile from Chapter 2 of Young's book was utilized [29] to calculate the average charge required

to accelerate a vehicle from 0 to 60 miles per hour in 10 seconds.

Using the derived model for force from Section 3.3, the average required power to accelerate from zero to 60 miles per hour was 55.7kW. Chapter 2 of Young's book reported an average of 60.8kW for the acceleration profile. The discrepancy is due to a difference in the fixed rolling coefficient and drag used from Section 3.3 as apposed to the rolling and drag coefficient proposed in Chapter 2 of Young's book [29].

Figure 4.14 shows the results of the power consumption required to accelerate from 0 to 60 miles per hour in 10 seconds.
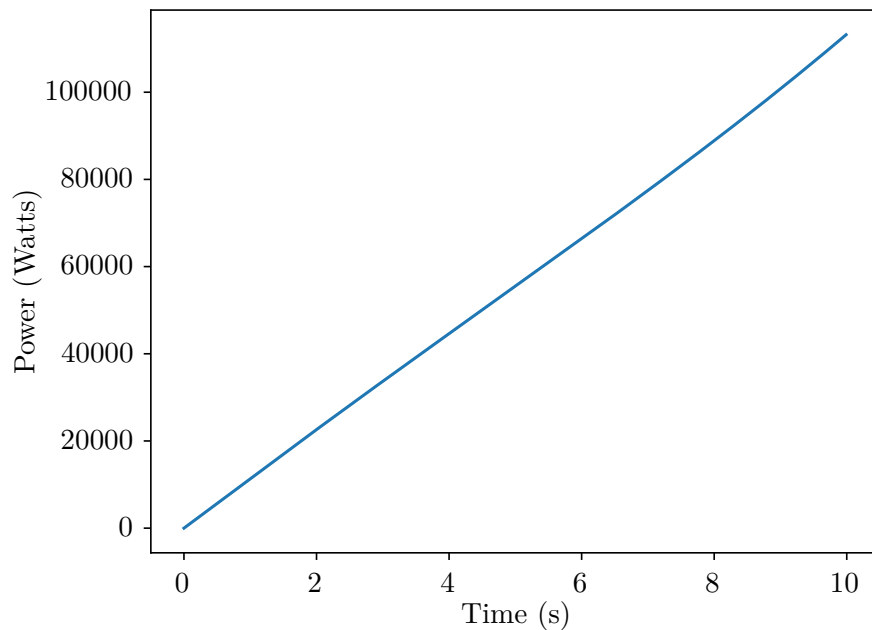
Fig. 4.14: Results of the power consumption due to acceleration from 0 to 60 miles per hour in 10 seconds.

Because the average of Figure 4.14 is within 8.5 percent error of the aggressive acceleration profile proposed in [29], the acceleration estimates will give an adequate approximation of the current state of charge.

4.2.2 Simulated Highway Driving Results

To verify the state of charge estimate for long distances, the vehicle profile for the Ford Focus 2012 was utilized with the parameters outlined in Table 4.6.

Table 4.6: Parameter list to simulate average watt-hours per kilometer for the Ford Focus 2012 Electric Vehicle driving at highway speeds.

Parameter	Value
Front Area (m)	2.24546551
Mass (kg)	1643.819
Tire Pressure (PSI)	35
Mass Factor	1.05
Drag Coefficient	0.274
Air Density (kg/m^2)	1.225
Driving Incline (degrees)	0
Tire Friction Coefficient	0.5
Regenerative Charging Coefficient	.85

According to the United States Environmental Protection Agency, the Ford Focus 2012 travels 122km using a 23kWh battery [35]. The number of watt hours per kilometer is estimated as

$$\left(122 \cdot \frac{\text{km}}{23\text{kWh}} \cdot \frac{\text{kWh}}{1000\text{Wh}} \right)^{-1} \approx 188.5 \frac{\text{wh}}{\text{km}}$$

Performing a simulation of the vehicle driving with one passenger at a constant 65 miles-per-hour for 5 minutes resulted in an estimated $155.1 \frac{\text{wh}}{\text{km}}$. Because the estimate does not include critical electronic usage, and acceleration, it is an adequate estimate for vehicle battery usage based on motor demands.

4.3   Noise Shaping Filter Results without Sensor Noise

This Section verifies all system constraints outlined in Section 3.6 and gives a brief analysis of the results.

Section 4.3.1 establishes the simulation parameters for the result validation, Section 4.3.2 demonstrates the filter's ability to keep variations within distance constraints, Section 4.3.3 validates all acceleration constraints, and Section 4.3.4 confirms the desired average charge of the system.

4.3.1   Simulation Parameters

For all the results in Section 4.3, the parameters in Table 4.7 are utilized unless otherwise specified.

Table 4.7: Parameter list for simulation verification of the noise shaping filter without control sensor noise.

Parameter	Value
ω_l (rad)	0.809
ω_h (rad)	0.809
K	0.38
Time (s)	40
Analysis Start Time (s)	10
Simulations	250
Desired Charge (Watts)	40000
Desired Probability Interval	0.97
Maximum δ (m)	1.76
Maximum α (m/s^2)	1.2
Maximum alpha frequency (Hz)	0.2
Trajectory Length (m)	200
Trajectory Velocity (m/s)	10
Control Sensor Noise	False

4.3.2 Noise Position Constraint Results

This section tests the position constraint of the noise shaping filter outlined in Section 3.6. The position constraint is position variation δ must be less than or equal to $\delta_{\max} = 1.76\,m$. The results of the vehicle's trajectory after 250 simulations can be seen in Figure 4.15.
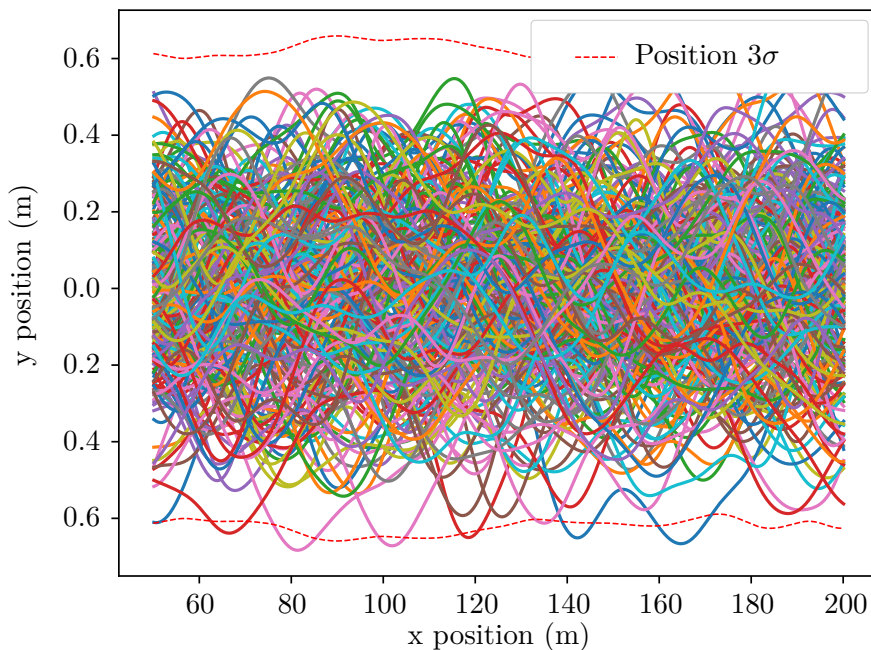
Fig. 4.15: Plot verifying that the position maximum constraint $\delta_{\max}$ is not violated for the noise variation. This Figure Demonstrates that all Monte Carlo simulations are successfully within the $\delta_{\max}$ of $1.76m$ for the case that $K = 0.38$

Figure 4.15 shows the trajectories of the 250 simulations and plots the standard deviation at each ensemble. None of the trajectories are beyond the $\sigma_{\max}$ boundary, therefore the system complies with the position constraints.

4.3.3   Acceleration Comfort Constraint Results

This section tests the acceleration constraints of the noise shaping filter outlined in Section 3.6. The acceleration constraints outlined in Section 3.6 are that acceleration inputs α must be less than or equal to $\alpha_{\max} = 1.2\,m/s^2$, and that the -3dB cut-off of the acceleration filter should be at $f_{\max} = .2$Hz. Figure 4.16 verifies that the acceleration variation does not extend past $1.2\,m/s^2$.
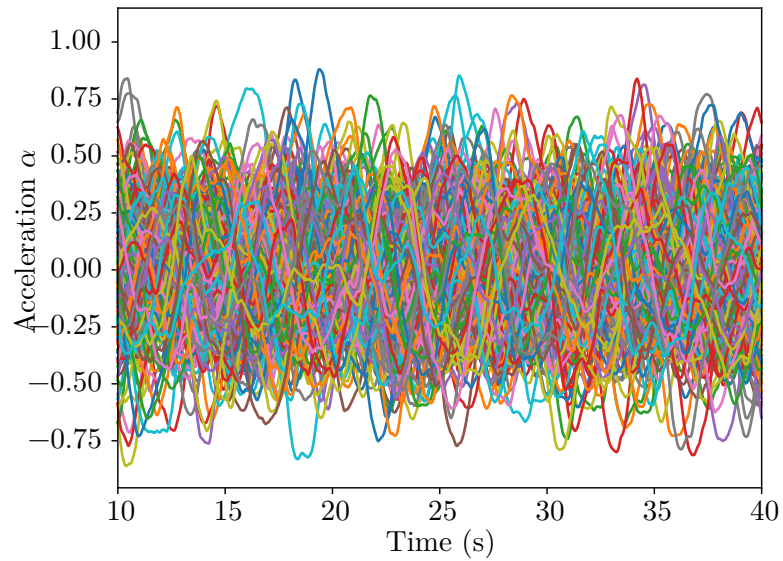
Fig. 4.16: Plot verifying that the acceleration maximum constraint $\alpha_{\max}$ is not violated for the noise variation. This Figure Demonstrates that all Monte Carlo simulations are successfully within the $\delta_{\max}$ of $1.2 m/s^2$ for the case that $K = 0.38$.

Because Figure 4.16 shows that the maximum acceleration threshold is not violated, the value of $K = 3.99$ is within the system specifications.

To comply with the cut-off frequency constraint, the -3dB cut-off frequency is set to $f_{\max} = .2\text{Hz} = 1.2566\,\text{rad}$ when the the band-pass filter's maximum value is at 1. Figure 4.17 shows the verification of the cut-off frequency constraint.
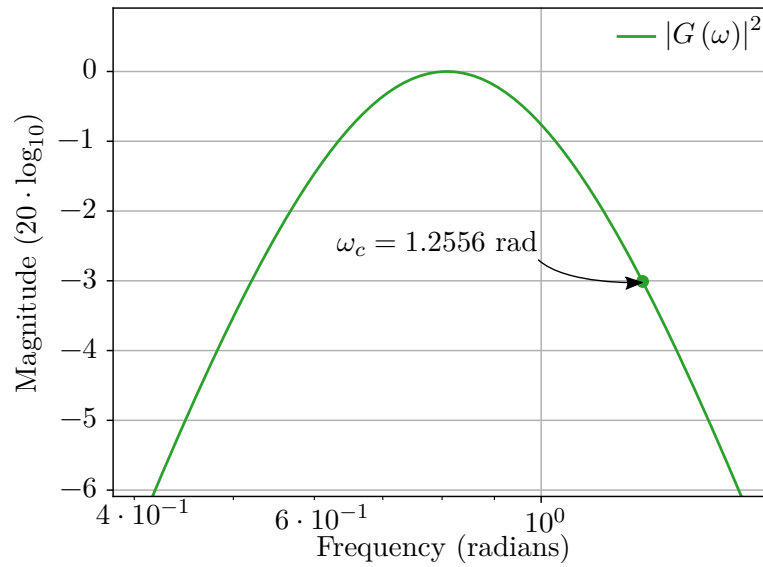
Fig. 4.17: Plot verifying that the maximum cut-off frequency of acceleration noise variation is less than or equal to $1.2566\,\mathrm{rad}$

Figure 4.17 shows that the maximum acceleration frequency constraint is met.

4.3.4 Delivering a Desired Charge within a Probability Interval

The purpose of this section is to test charging constraints of the noise shaping filter outlined in Section 3.6. The charging constraint outlined in Section 3.6 is that average charge q_d should be attained within a specified probability interval p. The specified average charge was 40000 Watts with a confidence interval of 0.97. Figure 4.18 shows the results of the 250 simulations.
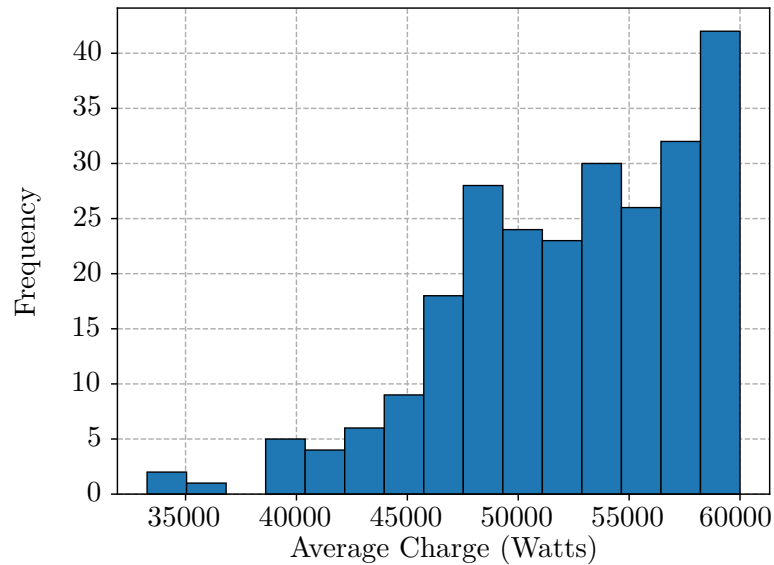
Fig. 4.18: Histogram plot testing that 97% of simulations had an expected charge above 40000 Watts without sensor noise. This figure demonstrates that of the 250 simulations, 96.8% of the simulations were above 40000 Watts.

Figure 4.18 shows that the probability of receiving an expected charge of 40000 Watts or more is 96.8% as expected.

4.4 Noise Shaping Filter Results with Sensor Noise

This section shows that the added noise of the vehicle sensors effects the analysis of the noise shaping filter, and it can not be neglected.

When sensor noise is added to the EKF observer on the GPS, steering angle sensor, and velocity sensor, new noise is added to the control input beyond what is analyzed for the noise shaping filter in Section 3.6.4. To verify the added system noise, the test from Section 4.3.4 is repeated with the sensor noise profile from Section 4.1.1. The results show that only 91.6% of the simulations successfully received 40kW or more when 97% were expected to receive at least 40kW. A histogram of the results can be seen in Figure 4.19.
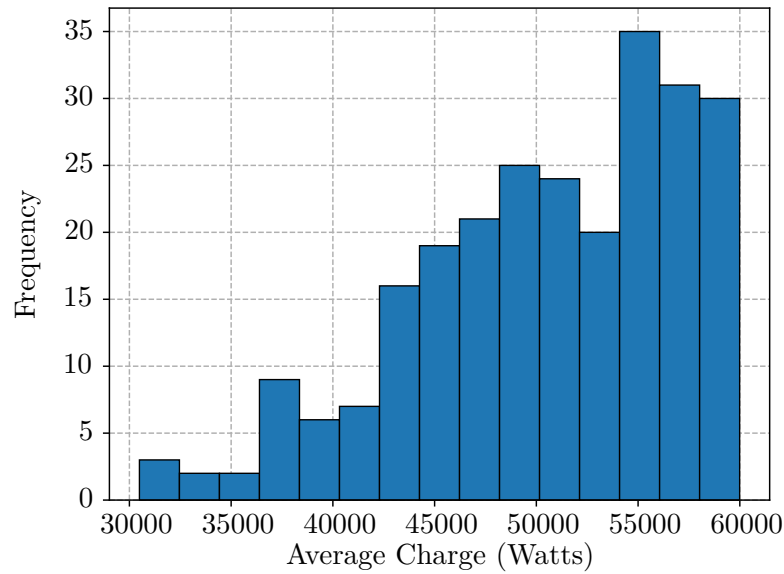
Fig. 4.19: Histogram plot testing that 97% of simulations had an expected charge above 40000 Watts with sensor noise introduced. This figure demonstrates that of the 250 simulations, 91.6% of the simulations were above 40000 Watts.

Figure 4.19 verifies that an additional analysis of the noise shaping filter with the presence of sensor noise is warranted. Therefore, Section 4.4.1 will define new equations for calculating K.

4.4.1 Nonlinear Charging Profile and Probability Interval with Sensor Noise

This section shows how a nonlinear charging profile for calculating K can be obtained for the noise shaping filter with vehicle sensor noise is included. Using the same procedure outlined in Section 3.6.4, a new equation for calculating K based on a desired charge with a probability interval was developed by running 250 Monte Carlo Simulation with sensor noise turned on for incremental values of K ranging from 0.1 to one. The new fit data is plotted next to the noise shaping results from Section 4.3.4 to compare the results. Figure 4.20 compares the required K value to obtain an average expected charge within a probability interval of 0.97 with and without sensor noise.
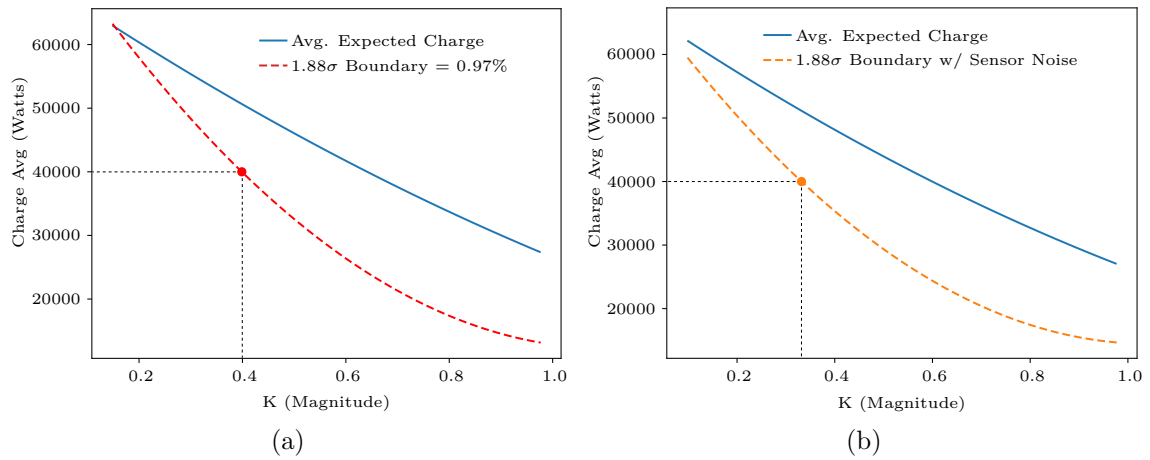
Fig. 4.20: (a) Plot of calculating the required noise shaping filter gain K without added sensor noise to ensure 40kW average charge within 97% probability, which cooresponds to 1.88 standard deviations from the average expected charge. (b) Plot of calculating the required noise shaping filter gain K including sensor noise to ensure 40kW average charge within 97% probability.

As seen in Figure 4.20, the magnitude of K must is smaller when sensor noise is included to account for the additional control noise. To verify the results of the expected average charge with sensor noise,the test from Section 4.3.4 was reproduced using the new value of K. The resulting histogram of average charge can be seen in Figure 4.21.
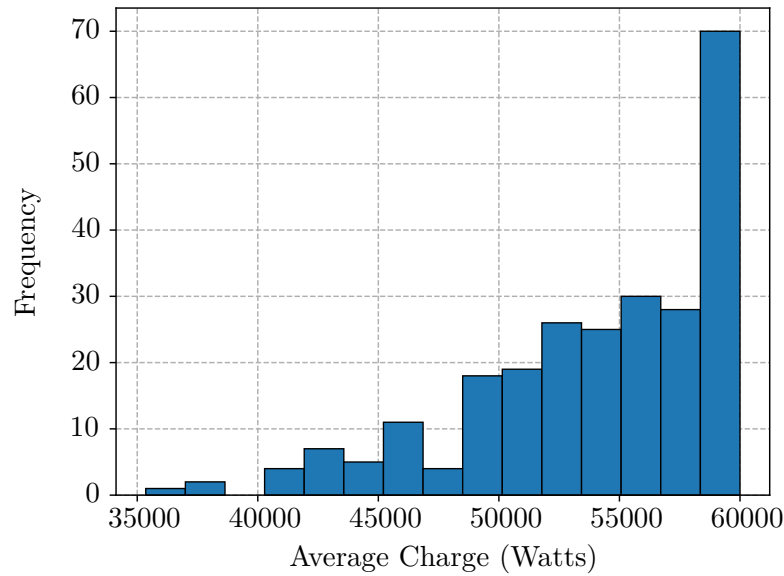
Fig. 4.21: Histogram plot testing that 97% of simulations had an expected charge above 40000 Watts with sensor noise introduced. This figure demonstrates that of the 250 simulations, 98.6% of the simulations were above 40000 Watts.

when the sensor noise was accounted for Figure 4.21 shows that with sensor noise on the EKF enabled, the expected average charge of a dynamic charging region can still be achieved.

To further characterize the effect of the sensor noise sources, each noise source was isolated for 250 Monte Carlo simulations. The variance of the steering angle error was sized using the steering angle sensor data-sheet from Methode Electronics [36] assuming a $\pm 30°$ maximum curvature vehicle limit, which corresponds to a sensor three sigma value of about $0.03°$. The velocity sensor was set to have a variance of $0.1 m/s$. The RTK GPS was set to have a variance of $0.03m$ with an update every of 1 Hz.

The effect of each sensor noise source on the standard deviation of the vehicle position error from the center of the trajectory can be seen in Figure 4.22.
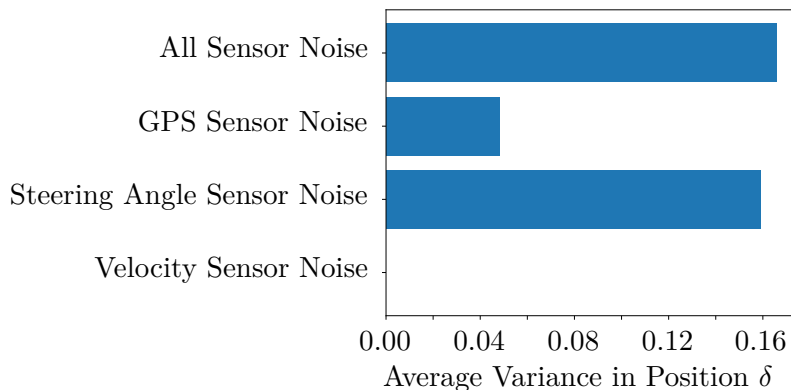
Fig. 4.22: Bar chart displaying the isolated effect of the sensor noise on each of the variance of the error δ from the center of the vehcile path. The sizing for the noise can be seen in Table 4.1 and Table 4.2.

Figure 4.22 shows that the sensor noise on the steering angle is the driving noise factor. Therefore, a more accurate steering angle sensor should be utilized to improve results.

4.5 Destination Arrival with a Desired State of Charge

This section tests that the path planner adequately sizes the output of the noise shaping filter based on a desired end charge Q_{wH} in watt-hours as discussed in Section 3.4.4.

Assuming the vehicle profile from Table 4.6 with an initial battery charge of 15kwH and a desired end charge of 15.3kwH, the simulated vehicle traveled a 1900 meter track with two 400-meters charging regions. The WPT charging regions were centered at 500 meters and 1300 meters of the path respectively, and the grade of the path changed from 3% to 2% at 900 meters as depicted in Figure 4.23.
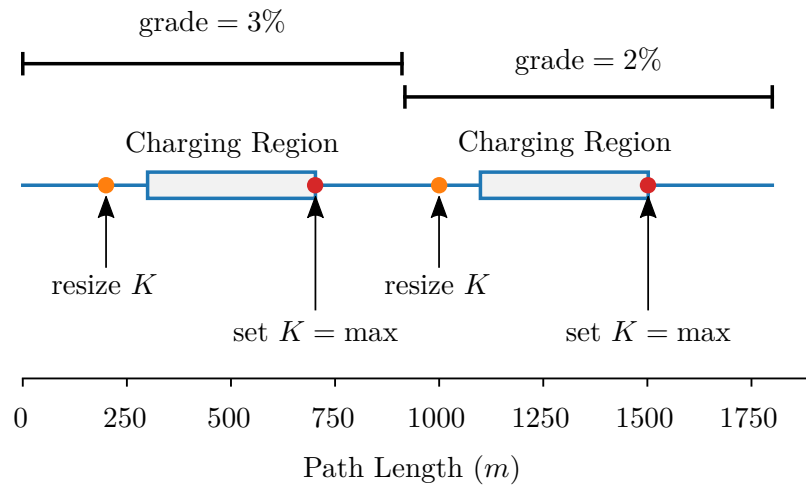
Fig. 4.23: Significant elements of the vehicle simulation path to show that the sizing of the noise shaping filter results in the desired end state of charge. The orange dots indicate when the vehicle re-calculates desired average charge for the noise shaping filter, and the red dots indicate when the shaping filter is set to maximum control variation.
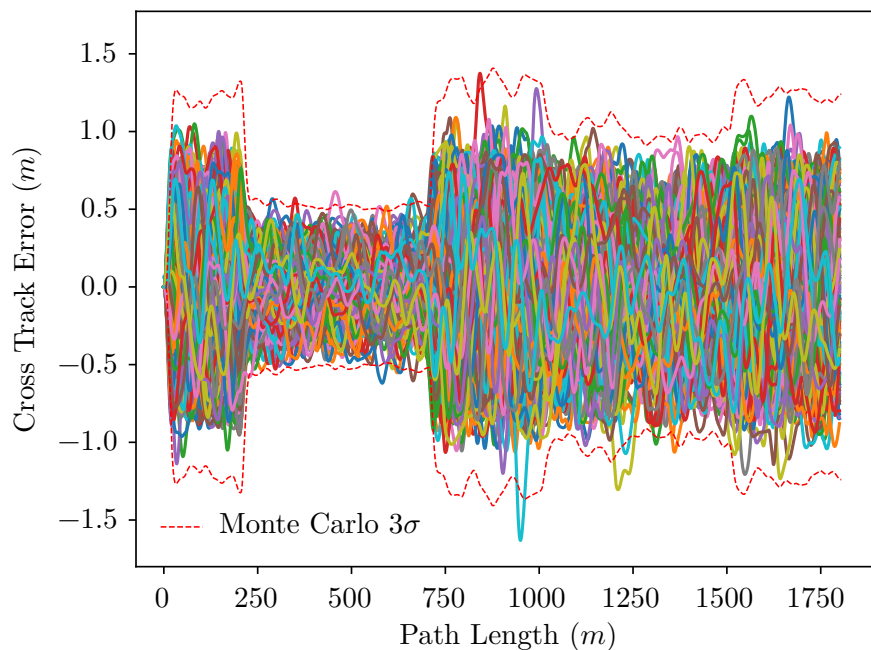
Fig. 4.24: Monte Carlo plot displaying the cross track error versus path length of the simulated vehicle to its destination at 1900 meters. The variance of the vehicle cross-track error changes as a function of the gain of the noise shaping filer which is recalculated at 200 meters and 1000 meters. The maximum control noise variation is set at the end of the charging pads, which occurs at 700 meters and 1500 meters.

Figure 4.23 shows that there is a change in path grade between the two charging regions. This change is used to test the ability of the path planner to adequately decrease the noise sizing to accommodate the reduction of average expected power consumption. The orange dots in Figure 4.23 symbolize when the path planner calculates a new control variation sizing based on the average power usage of the previous 10 seconds, and the red dots symbolize when a maximum path variation is set after a charging region is complete.

A Monte Carlo simulation of 250 runs was completed, and the results can be seen in Figure 4.24. Figure 4.24 visually shows how the path planner achieved the desired end state of charge without a prior knowledge of the path grade. At 200 meters, the first calculation for the desired average charge was set based on the 3% grade assumed from averaging the previous 10 seconds of power consumption. The calculation was intentionally made 10 seconds prior to the beginning of the charging station to allow the variance of the control variation to tighten before the beginning of the charging region. At 900 meters, the road grade was reduced to 2%, which resulted in less power drawn from the battery. Therefore, when the desired charge was again computed at 700 meters, the path planner determined that less charge was needed to arrive at the destination than previously solved for, so the noise sizing was increase.

The test desired to achieve a final battery state of 15.3kWh with 97% probability, and the test resulted in 96%, as seen in the histogram of Figure 4.25.
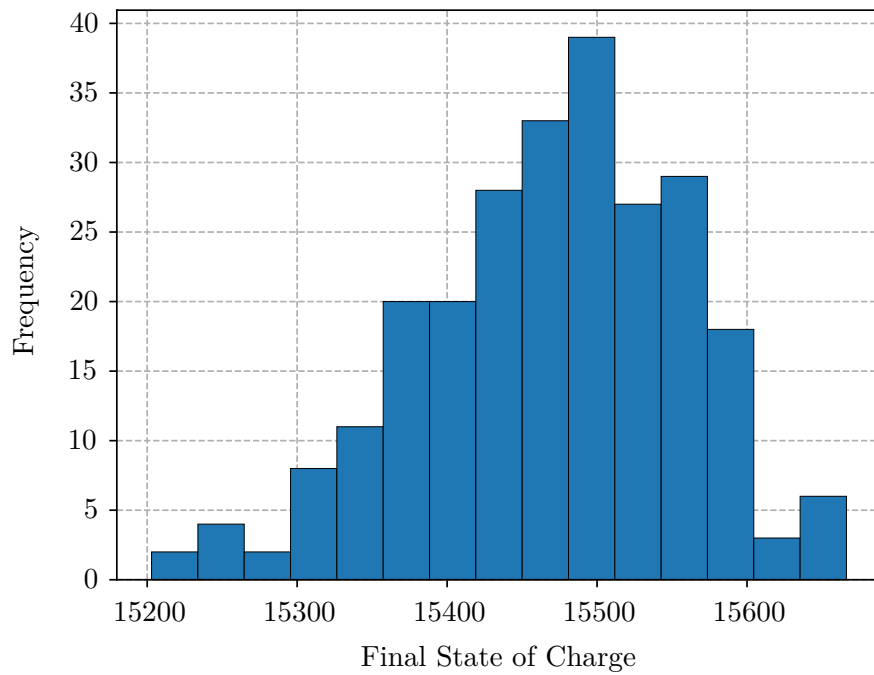
Fig. 4.25: Histogram plot showing the final battery state of charge when the vehicle arrived at its destination. Of the 250 simulations, 96% were expected to be above 15300 watt-hours, and the simulation resulted in 95.6% above 15300 watt-hours.

Because the test verifies an expected number of simulations with a desired end state of charge, the path planner correctly sizes the output of the noise shaping filter for a destination desired state of charge.

CHAPTER 5

CONCLUSION

5.1 Conclusion

A noise shaping filter that reduces road wear by injecting noise into a vehicle's control inputs has been presented. Using the analyzed properties of the noise shaping filter, the control input variation can be shaped to ensure position and acceleration constraints, and ensure that a vehicle arrives at a destination with a desired battery charge q_d within a probability interval p. The constraints that were met and verified by the noise shaping filter include:

- **Position Constraint:** Position from the center of the lane δ must be less than or equal to $\delta_{\max}$ meters.

- **Acceleration Constraint:** Vehicle acceleration inputs α must be less than or equal to $\alpha_{\max}\, m/s^2$.

- **Acceleration Frequency Constraint:** Acceleration changes must be less than or equal to $f_{\alpha\max}$ Hertz.

- **Controller Constraint:** Filter must produce variations in position, velocity, and acceleration to interface with the vehicle's controller.

- **Average Charge Constraint:** Average charge q_d must be attained within a specified probability interval p.

Because the results from Section 4.3.3 verify the simulated compliance with the outlined criteria, the noise shaping filter can be utilized to add an analytical amount of variation to a vehicle's trajectory. This research will aid in extending the road life of heavily trafficked dynamic charging WPT regions as the number of autonomous dynamically charging vehicles

increases. Current applications of this research also extends to reducing the road wear caused by heavy autonomous mining equipment and autonomous farming equipment.

This research contributes to the field of controls by presenting a zero-analytical tracking error controller for a Continuous Curvature Path (CCPath). To ensure tracking, the CCPath takes into account the curvature and steering rate limits imposed by a vehicle's velocity. The zero tracking error controller is achieved by creating an ϵ-Tracking path for a reference control point on a vehicle. This contribution offers a linear feedback control law that can track a vehicle trajectory and add a desired variation from the noise shaping filter.

This research contributes to the navigation field by developing an Extended Kalman Filter (EKF) that uses RTK GPS, a steering sensor, and a velocity sensor for state estimation. The EKF was developed to analyze how sensor noise effects the noise shaping filter properties.

To verify the accuracy of the noise shaping filter analysis, Monte Carlo simulations were performed on the noise shaping filter with and without simulated vehicle sensor noise. It was determined that the sensor noise can not be neglected when sizing parameters for the noise shaping filter due to the added path variation caused by the sensor noise. Therefore, the noise shaping filter analysis was repeated including the additional sensor noise, and consistent expected charging results were achieved.

The next natural stage for this research is to bound the variance of jerk added to the control inputs produced by the noise shaping filter. One proposed method to bound jerk, is to use a band-pass filter with a 60db/decade roll-off that can be integrated three times to produce jerk, acceleration, velocity, and position variation. Additionally, the vehicle controller should be extended to satisfy jerk constraints, and a modified path planner could be extend to produce a path of G^3 continuity.

Future work also includes characterizing which shaping filter parameters will minimize road wear. This research assumes that the control variation with a maximum position cut-off frequency minimizes road wear while decreasing the standard deviation of expected charge, but a formal analysis could be performed.

For safe integration on a vehicle, future work also include hardware implementation and verification for the sections outlined in Chapter 4.

REFERENCES

[1] J. Cobb, "December 2017 Dashboard," 2018. [Online]. Available: https://www.hybridcars.com/december-2017-dashboard/

[2] WAVE, "WAVE Announces Wireless Charging with AVTA at Lancaster City Park and Palmdale Transportation Center," Tech. Rep.

[3] News, "50 kW Deployments." [Online]. Available: https://waveipt.com/news/

[4] J. Kim, J. Kim, S. Kong, H. Kim, I. Suh, N. P. Suh, D. Cho, J. Kim, and S. Ahn, "Coil design and shielding methods for a magnetic resonant wireless power transfer system," *Proceedings of the IEEE*, vol. 101, no. 6, pp. 1332–1342, June 2013.

[5] J. Shin, S. Shin, Y. Kim, S. Ahn, S. Lee, G. Jung, S. Jeon, and D. Cho, "Design and implementation of shaped magnetic-resonance-based wireless power transfer system for roadway-powered moving electric vehicles," *IEEE Transactions on Industrial Electronics*, vol. 61, no. 3, pp. 1179–1192, March 2014.

[6]

[7]

[8] Z. Bi, T. Kan, C. C. Mi, Y. Zhang, Z. Zhao, and G. A. Keoleian, "A review of wireless power transfer for electric vehicles: Prospects to enhance sustainable mobility," *Applied Energy*, vol. 179, pp. 413–425, 2016. [Online]. Available: http://www.sciencedirect.com/science/article/pii/S0306261916309448

[9] Y. S. Byun and Y. C. Kim, "Localization based on magnetic markers for an all-wheel steering vehicle," *Sensors (Switzerland)*, 2016.

[10] M. Cornick, J. Koechling, B. Stanley, and B. Zhang, "Localizing Ground Penetrating RADAR: A Step Towards Robust Autonomous Ground Vehicle Localization," Ph.D. dissertation, MIT Lincoln Laboratory, 2016.

[11] L. Chu, G. Ping Ong, T. F. Fwa, and G. P. Ong, "Evaluating Hydroplaning Potential of Rutted Highway Pavements Disruption Modeling for Public Transportation Systems View project Sustainable Transportation Planning and Policy in Malaysia View project Evaluating Hydroplaning Potential of Rutted Highway Pa," *Journal of the Eastern Asia Society for Transportation Studies*, vol. 11, 2015. [Online]. Available: https://www.researchgate.net/publication/317868902

[12] J. N. Ivan, N. Ravishanker, E. Jackson, B. Aronov, and S. Guo, "A Statistical Analysis of the Effect of Wet-Pavement Friction on Highway Traffic Safety," *Journal of Transportation Safety & Security*, 2012.

[13] S. F. Said and H. Hakim, "Effects of transversal distribution of heavy vehicles on rut formation in bituminous layers," Swedish National Road and Transport Research Institute, Tech. Rep., 2018.

[14] Hjort Mattias, Mattias Haraldsson, and Jansen Jan, "Road Wear from Heavy Vehicles – an overview," NVF committee Vehicles and Transports, Tech. Rep., 2008.

[15] T. Fraichard and A. Scheuer, "From Reeds and Shepp's to continuous-curvature paths," *IEEE Transactions on Robotics*, 2004.

[16] A. M. Lekkas, *Anastasios M. Lekkas Guidance and Path-Planning Systems for Autonomous Vehicles*, 2014.

[17] Y. Chen, Y. Cai, J. Zheng, and D. Thalmann, "Accurate and Efficient Approximation of Clothoids Using Bézier Curves for Path Planning," *IEEE Transactions on Robotics*, 2017.

[18] M. Brezak and I. Petrović, "Path smoothing using clothoids for differential drive mobile robots," in *IFAC Proceedings Volumes (IFAC-PapersOnline)*, 2011.

[19] J. Eriksson and L. Svensson, "Tuning for Ride Quality in Autonomous Vehicle Application to Linear Quadratic Path Planning Algorithm," Ph.D. dissertation, Uppsala Universitet, 2015. [Online]. Available: http://www.teknat.uu.se/student

[20] A. S. Kilinç and T. Baybura, "Determination of Minimum Horizontal Curve Radius Used in the Design of Transportation Structures, Depending on the Limit Value of Comfort Criterion Lateral Jerk," Uşak University, Tech. Rep., 2012.

[21] J. Villagra, V. Milanés, J. Pérez, and J. Godoy, "Smooth path and speed planning for an automated public transport vehicle," *Robotics and Autonomous Systems*, 2012.

[22] J. F. Golding, "A motion sickness maximum around the 0.2 Hz frequency range of horizontal translational oscillation," *Aviation Space and Environmental Medicine*, 2001. [Online]. Available: https://www.researchgate.net/publication/12056741

[23] J. M. Snider, "Automatic Steering Methods for Autonomous Automobile Path Tracking," Ph.D. dissertation, Carnegie Mellon University, 2009.

[24] D. Shin, S. Singh, and W. Whittaker, "Path Generation for a Robot Vehicle Using Composite Clothoid Segments," *IFAC Proceedings Volumes*, 1992.

[25] E. Abbott and D. Powell, "Land-vehicle navigation using GPS," *Proceedings of the IEEE*, 1999.

[26] M. Salama, A. Abd, E. Tawab, and I. I. Mahmoud, "Particle / Kalman Filter for Efficient Robot Localization Model Predictive Control View project WSNs for Nuclear Material Detection and Localization View project Imbaby Ismail Mahmoud Egyptian Atomic Energy Authority Particle/Kalman Filter for Efficient R," *Article in International Journal of Computer Applications*, vol. 106, no. 2, pp. 975–8887, 2014. [Online]. Available: https://www.researchgate.net/publication/268444252

[27] G. Wan, X. Yang, R. Cai, H. Li, H. Wang, and S. Song, "Robust and Precise Vehicle Localization based on Multi-sensor Fusion in Diverse City Scenes," 2017.

[28] Y. S. Byun, R. G. Jeong, and S. W. Kang, "Vehicle position estimation based on magnetic markers: Enhanced accuracy by compensation of time delays," *Sensors (Switzerland)*, 2015.

[29] K. Young, C. Wang, L. Y. Wang, and K. Strunz, "Electric vehicle battery technologies," in *Electric Vehicle Integration into Modern Power Networks*, 2013.

[30] EngineeringToolbox, "Rolling Resistance Testing," 2011. [Online]. Available: https://www.engineeringtoolbox.com/rolling-friction-resistance-d_1303.html

[31] N. R. Kapania and J. C. Gerdes, "An Autonomous Lanekeeping System for Vehicle Path Tracking and Stability at the Limits of Handling," Tech. Rep., 2014.

[32] R. Olfati-Saber, "Near-Identity Diffeomorphisms and Exponential-Tracking and-Stabilization of First-Order Nonholonomic SE(2) Vehicles," Tech. Rep.

[33] S. M. LaValle, "Planning algorithms," *Planning Algorithms*, vol. 9780521862, pp. 1–826, 2006.

[34] Y. Kanayama and B. I. Hartman, "Smooth local path planning for autonomous vehicles," in *Proceedings, 1989 International Conference on Robotics and Automation*, May 1989, pp. 1265–1270 vol.3.

[35] Fueleconomy, "Gas Mileage of 2012 Ford Focus." [Online]. Available: https://www.fueleconomy.gov/feg/bymodel/2012_Ford_Focus.shtml

[36] Methode Electronics, "Steering Angle Sensor for Automotive Applications," apr 2007. [Online]. Available: http://fr.methode.com/Documents/TechnicalLibrary/Steering_Angle_Sensor_Data_Sheet.pdf

APPENDICES

APPENDIX A

Appendix

A.1 Navigation Model Linearization

The following derivation is for Section 3.2.2, which defines the navigation filter linearized states for covariance propagation.

Given the nonlinear differential equation:

$$\dot{\underline{x}} = \underline{f}\left(\underline{x}, \underline{\tilde{y}}, \underline{w}, t\right) \tag{A.1}$$

The goal for linearization is to convert the differential equation to the form of Equation A.2, to be able to propagate the covariance using Equation A.3.

$$\delta\dot{\underline{x}} = F\left(\underline{x}, \underline{\tilde{y}}, t\right)\delta\underline{x} + G\left(\underline{x}, \underline{\tilde{y}}, t\right)\underline{w} \tag{A.2}$$

$$\dot{P} = FP + PF^T + GQG^T \tag{A.3}$$

To linearize the nonlinear differential equations for covariance propagation, Equations A.6 through A.15 define variation equations for each state in the system, Equation A.5 establishes a nominal differential equation, Equation A.23 substitutes the variation equations into the system, and Equation A.24 uses a Taylor series approximation to eliminate nonlinearities. Finally, A.27 reduces the equations to a linear form with F and G matrices.

Define the navigation filter design model

$$
\begin{bmatrix} \dot{x}_1 \\ \dot{x}_2 \\ \dot{\psi} \\ \dot{b}_v \\ \dot{b}_\phi \end{bmatrix} = \begin{bmatrix} (\tilde{v} - b_v - n_v)\cos(\psi) \\ (\tilde{v} - b_v - n_v)\sin(\psi) \\ \frac{\tilde{v}-b_v-n_v}{L}\tan\left(\tilde{\phi} - b_\phi - n_\phi\right) \\ -\frac{1}{\tau_v}b_v + w_v \\ -\frac{1}{\tau_\phi}b_\psi + w_\phi \end{bmatrix} \tag{A.4}
$$

Define the nominal differential equation

$$
\begin{bmatrix} \dot{\hat{x}}_1 \\ \dot{\hat{x}}_2 \\ \dot{\hat{\psi}} \\ \dot{\hat{b}}_v \\ \dot{\hat{b}}_\phi \end{bmatrix} = \begin{bmatrix} \left(\tilde{v} - \hat{b}_v\right)\cos\left(\hat{\psi}\right) \\ \left(\tilde{v} - \hat{b}_v\right)\sin\left(\hat{\psi}\right) \\ \frac{\tilde{v}-\hat{b}_v}{L}\tan\left(\tilde{\phi} - \hat{b}_\phi\right) \\ -\frac{1}{\tau_v}\hat{b}_v \\ -\frac{1}{\tau_\phi}\hat{b}_\phi \end{bmatrix} \tag{A.5}
$$

Define the error states

$$ x_1 = \hat{x}_1 + \delta x_1 \tag{A.6} $$

$$ x_2 = \hat{x}_2 + \delta x_2 \tag{A.7} $$

$$ \psi = \hat{\psi} + \delta\psi \tag{A.8} $$

$$ b_v = \hat{b}_v + \delta b_v \tag{A.9} $$

$$ b_\phi = \hat{b}_\phi + \delta b_\phi \tag{A.10} $$

$$ \dot{x}_1 = \dot{\hat{x}}_1 + \delta\dot{x}_1 \tag{A.11} $$

$$ \dot{x}_2 = \dot{\hat{x}}_2 + \delta\dot{x}_2 \tag{A.12} $$

$$ \dot{\psi} = \dot{\hat{\psi}} + \delta\dot{\psi} \tag{A.13} $$

$$ \dot{b}_v = \dot{\hat{b}}_v + \delta\dot{b}_v \tag{A.14} $$

$$ \dot{b}_\phi = \dot{\hat{b}}_\phi + \delta\dot{b}_\phi \tag{A.15} $$

Redefine the design model with small angle approximation to separate the state terms from the noise terms that are inside the tangent operator.

$$
\begin{bmatrix} \dot{x}_1 \\ \dot{x}_2 \\ \dot{\psi} \\ \dot{b}_v \\ \dot{b}_\phi \end{bmatrix} = \begin{bmatrix} (\tilde{v} - b_v - n_v)\cos(\psi) \\ (\tilde{v} - b_v - n_v)\sin(\psi) \\ \frac{\tilde{v}-b_v-n_v}{L}\left(\tilde{\phi} - b_\phi - n_\phi\right) \\ -\frac{1}{\tau_v}b_v + w_v \\ -\frac{1}{\tau_\phi}b_\phi + w_\phi \end{bmatrix}
\tag{A.16}
$$

Group system terms by state and noise variables

$$
\begin{bmatrix} \dot{x}_1 \\ \dot{x}_2 \\ \dot{\psi} \\ \dot{b}_v \\ \dot{b}_\phi \end{bmatrix} = \begin{bmatrix} (\tilde{v} - b_v)\cos(\psi) - \cos(\psi)n_v \\ (\tilde{v} - b_v)\sin(\psi) - \sin(\psi)n_v \\ \frac{\tilde{v}-b_v-n_v}{L}\left(\tilde{\phi} - b_\phi\right) + \frac{1}{L}\left(-\tilde{v}n_\phi + b_v n_\phi + n_v n_\phi\right) \\ -\frac{1}{\tau_v}b_v + w_v \\ -\frac{1}{\tau_\phi}b_\phi + w_\phi \end{bmatrix}
\tag{A.17}
$$

Discard second order noise term

$$
\begin{bmatrix} \dot{x}_1 \\ \dot{x}_2 \\ \dot{\psi} \\ \dot{b}_v \\ \dot{b}_\phi \end{bmatrix} = \begin{bmatrix} (\tilde{v} - b_v)\cos(\psi) - \cos(\psi)n_v \\ (\tilde{v} - b_v)\sin(\psi) - \sin(\psi)n_v \\ \frac{\tilde{v}-b_v-n_v}{L}\left(\tilde{\phi} - b_\phi\right) + \frac{1}{L}\left(-\tilde{v}n_\phi + b_v n_\phi\right) \\ -\frac{1}{\tau_v}b_v + w_v \\ -\frac{1}{\tau_\phi}b_\phi + w_\phi \end{bmatrix}
\tag{A.18}
$$

Continue grouping like terms

$$
\begin{bmatrix} \dot{x}_1 \\ \dot{x}_2 \\ \dot{\psi} \\ \dot{b}_v \\ \dot{b}_\phi \end{bmatrix} = \begin{bmatrix} (\tilde{v} - b_v)\cos(\psi) - \cos(\psi)\,n_v \\ (\tilde{v} - b_v)\sin(\psi) - \sin(\psi)\,n_v \\ \frac{\tilde{v}-b_v}{L}\left(\tilde{\phi} - b_\phi\right) + \frac{1}{L}\left(-\tilde{v}n_\phi + b_v n_\phi\right) - \frac{1}{L}n_{\tilde{v}}\left(\tilde{\phi} - b_\phi\right) \\ -\frac{1}{\tau_v}b_v + w_v \\ -\frac{1}{\tau_\phi}b_\phi + w_\phi \end{bmatrix}
\tag{A.19}
$$

$$
\begin{bmatrix} \dot{x}_1 \\ \dot{x}_2 \\ \dot{\psi} \\ \dot{b}_v \\ \dot{b}_\phi \end{bmatrix} = \begin{bmatrix} (\tilde{v} - b_v)\cos(\psi) - \cos(\psi)\,n_v \\ (\tilde{v} - b_v)\sin(\psi) - \sin(\psi)\,n_v \\ \frac{\tilde{v}-b_v}{L}\left(\tilde{\phi} - b_\phi\right) + \frac{1}{L}\left((-\tilde{v} + b_v)n_\phi - (\tilde{\phi} - b_\phi)n_v\right) \\ -\frac{1}{\tau_v}b_v + w_v \\ -\frac{1}{\tau_\phi}b_\phi + w_\phi \end{bmatrix}
\tag{A.20}
$$

Place in form of state variables and noise variables

$$
\begin{bmatrix} \dot{x}_1 \\ \dot{x}_2 \\ \dot{\psi} \\ \dot{b}_v \\ \dot{b}_\phi \end{bmatrix} = \begin{bmatrix} (\tilde{v} - b_v)\cos(\psi) \\ (\tilde{v} - b_v)\sin(\psi) \\ \frac{\tilde{v}-b_v}{L}\left(\tilde{\phi} - b_\phi\right) \\ -\frac{1}{\tau_v}b_v \\ -\frac{1}{\tau_\phi}b_\phi \end{bmatrix} + \begin{bmatrix} -\cos(\psi)\,n_v \\ -\sin(\psi)\,n_v \\ -\frac{1}{L}(\tilde{\phi} - b_\phi)n_v + \frac{1}{L}(-\tilde{v} + b_v)n_\phi \\ w_v \\ w_\phi \end{bmatrix}
\tag{A.21}
$$

$$
\begin{bmatrix} \dot{x}_1 \\ \dot{x}_2 \\ \dot{\psi} \\ \dot{b}_v \\ \dot{b}_\phi \end{bmatrix} = \begin{bmatrix} (\tilde{v} - b_v)\cos(\psi) \\ (\tilde{v} - b_v)\sin(\psi) \\ \frac{\tilde{v}-b_v}{L}\left(\tilde{\phi} - b_\phi\right) \\ -\frac{1}{\tau_v}b_v \\ -\frac{1}{\tau_\phi}b_\phi \end{bmatrix} + \begin{bmatrix} -\cos\psi & 0 & 0 & 0 \\ -\sin\psi & 0 & 0 & 0 \\ \frac{1}{L}(b_\phi - \tilde{\phi}) & \frac{1}{L}(b_v - \tilde{v}) & 0 & 0 \\ 0 & 0 & 1 & 0 \\ 0 & 0 & 0 & 1 \end{bmatrix} \begin{bmatrix} n_v \\ n_\phi \\ w_v \\ w_\phi \end{bmatrix}
\tag{A.22}
$$

Substitute variations into equations

$$
\dot{\underline{x}} + \delta\dot{\underline{x}} = \underline{f}\left(\hat{\underline{x}} + \delta\underline{x}, \tilde{\underline{y}}, t\right) + G(\underline{x}, \tilde{\underline{y}}, t)\underline{w}
\tag{A.23}
$$

Use Taylor series approximation

$$\dot{\hat{\underline{x}}} + \delta\dot{\underline{x}} = \underline{f}(\hat{\underline{x}}, \tilde{\underline{y}}, t) + \frac{\partial f}{\partial \underline{x}}\bigg|_{\hat{x}} \delta\underline{x} + G(\underline{x}, \tilde{\underline{y}}, t)\underline{w} + H.O.T \tag{A.24}$$

Substitute definition of nominal path, and simply

$$\dot{\hat{\underline{x}}} + \delta\dot{\underline{x}} = \dot{\hat{\underline{x}}} + \frac{\partial f}{\partial \underline{x}}\bigg|_{\hat{x}} \delta\underline{x} + G(\underline{x}, \tilde{\underline{y}}, t)\underline{w} + H.O.T \tag{A.25}$$

$$\delta\dot{\underline{x}} = \frac{\partial f}{\partial \underline{x}}\bigg|_{\hat{x}} \delta\underline{x} + G(\underline{x}, \tilde{\underline{y}}, t)\underline{w} \tag{A.26}$$

Place in linear form

$$
\begin{bmatrix} \delta\dot{x}_1 \\ \delta\dot{x}_2 \\ \delta\dot{\psi} \\ \delta\dot{b}_v \\ \delta\dot{b}_\phi \end{bmatrix}
=
\begin{bmatrix}
0 & 0 & -(\tilde{v} - b_v)\sin\hat{\psi} & -\cos\hat{\psi} & 0 \\
0 & 0 & (\tilde{v} - b_v)\cos\hat{\psi} & -\sin\hat{\psi} & 0 \\
0 & 0 & 0 & \frac{1}{L}\left(\tilde{\phi} - b_\phi\right) & -\frac{\tilde{v}-b_v}{L} \\
0 & 0 & 0 & -\frac{1}{\tau_v} & 0 \\
0 & 0 & 0 & 0 & -\frac{1}{\tau_\phi}
\end{bmatrix}
\begin{bmatrix} \delta x_1 \\ \delta x_2 \\ \delta\psi \\ \delta b_v \\ \delta b_\phi \end{bmatrix}
$$
$$
+
\begin{bmatrix}
-\cos\hat{\psi} & 0 & 0 & 0 \\
-\sin\hat{\psi} & 0 & 0 & 0 \\
\frac{1}{L}(-\tilde{\phi} + b_\phi) & \frac{1}{L}(-\tilde{v} + b_v) & 0 & 0 \\
0 & 0 & 1 & 0 \\
0 & 0 & 0 & 1
\end{bmatrix}
\begin{bmatrix} n_v \\ n_\phi \\ w_v \\ w_\phi \end{bmatrix}
\tag{A.27}
$$

Equation A.27 is now in the desired linearized form of Equation A.2 with an F and G matrix.

A.1 Measurement Linearization

Equation A.28 is used to propagate the Kalman filter co-variance matrix P^+, where the Kalman Gain is defined in the a posteriori by Equation A.29, and $\mathbf{R}_p$ can be calculated using Equation A.30.

$$\mathbf{P}^+ = \mathbf{P}^- - \mathbf{K}\mathbf{H}\mathbf{P}^- \tag{A.28}$$

$$\mathbf{K} = \mathbf{P}^-\mathbf{H}^{\mathbf{T}}\left(\mathbf{H}\mathbf{P}^-\mathbf{H}^{\mathbf{T}} + \mathbf{R_p}\right)^{-\mathbf{1}} \tag{A.29}$$

$$\mathbf{R}_p\delta[n-m] = \mathrm{E}\big[\mathbf{v}[n]\mathbf{v}[m]^T\big] \tag{A.30}$$

The $\mathbf{H}$ matrix must be in a linearized form for the Kalman Gain a posteriori Equation, and it is computed by finding Equation A.31.

$$\delta\mathbf{z}[k] = \mathbf{H}(\hat{\mathbf{x}}[k], k)\delta\mathbf{x}[k] + \nu[k] \tag{A.31}$$

The nonlinear form is written as

$$\tilde{\mathbf{z}}[k] = h(\mathbf{x}[k], k) + \nu[k] \tag{A.32}$$

where the function $h(\mathbf{x}[k], k)$ maps the vehicle location $[x, y]^T$ into the measurement frame. The GPS location may not be positioned directly above the rear axle, so the measurement model includes a lever-arm transformation where L_{ref} is the distance from the back axle to

the GPS antenna.

$$\tilde{\mathbf{z}}[k] = h(\mathbf{x}[k], k) + \nu[k]$$

$$\tilde{\mathbf{z}}[k] = \begin{bmatrix} x[k] \\ y[k] \end{bmatrix} + \begin{bmatrix} \cos\left(\psi[k]\right) & -\sin\left(\psi[k]\right) \\ \sin\left(\psi[k]\right) & \cos\left(\psi[k]\right) \end{bmatrix} \begin{bmatrix} L_{\text{ref}} \\ 0 \end{bmatrix} + \underline{\nu}[k]$$

$$\tilde{\mathbf{z}}[k] = \begin{bmatrix} x[k] \\ y[k] \end{bmatrix} + \begin{bmatrix} L_{\text{ref}}\cos\left(\psi[k]\right) \\ L_{\text{ref}}\sin\left(\psi[k]\right) \end{bmatrix} + \underline{\nu}[k]$$

$$\tilde{\mathbf{z}}[k] = \begin{bmatrix} x[k] + L_{\text{ref}}\cos\left(\psi[k]\right) \\ y[k] + L_{\text{ref}}\sin\left(\psi[k]\right) \end{bmatrix} + \underline{\nu}[k] \tag{A.33}$$

The perturbations are defined as

$$\mathbf{x}[k] = \hat{\mathbf{x}}[k] + \delta\mathbf{x}[k] \tag{A.34}$$

$$\tilde{\mathbf{z}}[k] = \hat{\mathbf{z}}[k] + \delta\mathbf{z}[k] \tag{A.35}$$

so, let nominal measurement is defined by

$$\hat{\mathbf{z}} \equiv h\left(\hat{\mathbf{x}}[k], k\right) \tag{A.36}$$

Combining Equations A.35, A.36, and A.32 yields

$$\hat{\mathbf{z}}[k] + \delta\mathbf{z}[k] = \tilde{\mathbf{z}}[k] \tag{A.37}$$

$$h\left(\hat{\mathbf{x}}[k], k\right) + \delta\mathbf{z}[k] = h\left(\mathbf{x}[k], k\right) + \underline{\nu}[k] \tag{A.38}$$

$$h\left(\hat{\mathbf{x}}[k], k\right) + \delta\mathbf{z}[k] = h\left(\hat{\mathbf{x}}[k] + \delta\mathbf{x}[k], k\right) + \underline{\nu}[k] \tag{A.39}$$

$$h\left(\hat{\mathbf{x}}[k], k\right) + \delta\mathbf{z}[k] = h\left(\hat{\mathbf{x}}[k], k\right) + \left.\frac{\partial h}{\partial \mathbf{x}}\right|_{\hat{\mathbf{x}}} \delta\mathbf{x} + \underline{\nu}[k] \tag{A.40}$$

$$\delta\mathbf{z}[k] = \left.\frac{\partial h}{\partial \mathbf{x}}\right|_{\hat{\mathbf{x}}} \delta\mathbf{x} + \underline{\nu}[k] \tag{A.41}$$

Because the measurements must be in the form of Equation A.31, the measurement sensitivity matrix is found by taking the partial derivative of $h(\mathbf{x}[k], k)$.

$$
\frac{\partial h}{\partial \underline{\mathbf{x}}}\bigg|_{\hat{\underline{\mathbf{x}}}} = \left[\begin{array}{ccccc} \frac{\partial h_1}{\partial x} & \frac{\partial h_1}{\partial y} & \frac{\partial h_1}{\partial \psi} & \frac{\partial h_1}{\partial b_v} & \frac{\partial h_1}{\partial b_\phi} \\ \frac{\partial h_2}{\partial x} & \frac{\partial h_2}{\partial y} & \frac{\partial h_2}{\partial \psi} & \frac{\partial h_2}{\partial b_v} & \frac{\partial h_2}{\partial b_\phi} \end{array}\right]\bigg|_{\hat{\underline{\mathbf{x}}}}
\tag{A.42}
$$

$$
= \left[\begin{array}{ccccc} 1 & 0 & -L_{\text{ref}}\sin\left(\psi[k]\right) & 0 & 0 \\ 0 & 1 & L_{\text{ref}}\cos\left(\psi[k]\right) & 0 & 0 \end{array}\right]\bigg|_{\hat{\underline{\mathbf{x}}}}
\tag{A.43}
$$

$$
\hat{\mathbf{H}}_p = \left[\begin{array}{ccccc} 1 & 0 & -L_{\text{ref}}\sin\left(\hat{\psi}[k]\right) & 0 & 0 \\ 0 & 1 & L_{\text{ref}}\cos\left(\hat{\psi}[k]\right) & 0 & 0 \end{array}\right]
\tag{A.44}
$$

APPENDIX B

Appendix

B.1 Second Order Low-pass System Properties

Laplace Representation

$$G_l(s) = \frac{K\omega_l^2}{s^2 + 2\zeta\omega_l s + \omega_l^2}$$

System Magnitude

Let $\alpha = \omega_l^2$ and $\beta = 2\zeta\omega_l$

$$G_l(s) = \frac{K\alpha}{s^2 + \beta s + \alpha}$$

Substitute $s = j\omega$,

$$G_l(j\omega) = \frac{K\alpha}{(j\omega)^2 + (j\omega)\beta + \alpha}$$

$$G_l(j\omega) = \frac{K\alpha}{-\omega^2 + j\beta\omega + \alpha}$$

The equation for finding the magnitude is:

$$|x + jy| = \sqrt{x^2 + y^2}$$

Now, find the magnitude by taking the magnitude of the top and bottom separately.

$$|G_l(j\omega)| = \frac{|K\alpha|}{|-\omega^2 + j\beta\omega + \alpha|}$$

$$= \frac{K\alpha}{\sqrt{(\alpha - \omega^2)^2 + (\beta\omega)^2}}$$

$$= \frac{K\alpha}{\sqrt{(\alpha - \omega^2)(\alpha - \omega^2) + \beta^2\omega^2}}$$

$$= \frac{K\alpha}{\sqrt{\omega^4 - 2\alpha\omega^2 + \alpha^2 + \beta^2\omega^2}}$$

$$= \frac{K\alpha}{\sqrt{\omega^4 + (\beta^2 - 2\alpha)\omega^2 + \alpha^2}}$$

substitute α and β back into equations

$$|G_l(j\omega)| = \frac{K\omega_l^2}{\sqrt{\omega^4 + \left((2\zeta\omega_l)^2 - 2\omega_l^2\right)\omega^2 + \left(\omega_l^2\right)^2}}$$

$$|G_l(j\omega)| = \frac{K\omega_l^2}{\sqrt{\omega^4 + 2\omega_l^2(2\zeta^2 - 1)\omega^2 + \omega_l^4}}$$

Finding the magnitude squared

$$|G_l(j\omega)|^2 = \frac{K^2\omega_l^4}{\omega^4 + 2\omega_l^2(2\zeta^2 - 1)\omega^2 + \omega_l^4}$$

If $\zeta = \frac{1}{\sqrt{2}}$,

$$|G_l(j\omega)|^2 = \frac{K^2\omega_l^4}{\omega^4 + \omega_l^4}$$

Cut-off Frequency

To find the cut-off frequency at the value ρ, let $\gamma = 2\omega_l^2 \left(2\zeta^2 - 1\right)$ for convenience. Then,

$$\rho = \frac{K\omega_l^2}{\sqrt{\omega_c^4 + \gamma\omega_c^2 + \omega_l^4}}$$

$$\sqrt{\omega_c^4 + \gamma\omega_c^2 + \omega_l^4} = \frac{1}{\rho}K\omega_l^2$$

$$\omega_c^4 + \gamma\omega_c^2 + \omega_l^4 = \left(\frac{1}{\rho}K\omega_l^2\right)^2$$

$$\omega_c^4 + \gamma\omega_c^2 + \omega_l^4 = \frac{1}{\rho^2}K^2\omega_l^4$$

Let $\kappa = \frac{1}{\rho^2}K^2$

Completing the square to solve for ω_c:

$$\omega_c^4 + \gamma\omega_c^2 + \omega_l^4 = \frac{1}{\rho^2}K^2\omega_l^4$$

$$\omega_c^4 + \gamma\omega_c^2 = \frac{1}{\rho^2}K^2\omega_l^4 - \omega_l^4$$

$$\omega_c^4 + \gamma\omega_c^2 + \frac{1}{4}\gamma^2 = \frac{1}{\rho^2}K^2\omega_l^4 - \omega_l^4 + \frac{1}{4}\gamma^2$$

$$\left(\omega_c^2 + \frac{1}{2}\gamma\right)^2 = \frac{1}{\rho^2}K^2\omega_l^4 - \omega_l^4 + \frac{1}{4}\gamma^2$$

$$\omega_c^2 + \frac{1}{2}\gamma^2 = \pm\sqrt{\frac{1}{\rho^2}K^2\omega_l^4 - \omega_l^4 + \frac{1}{4}\gamma^2}$$

$$\omega_c^2 = -\frac{1}{2}\gamma^2 \pm \sqrt{\frac{1}{\rho^2}K^2\omega_l^4 - \omega_l^4 + \frac{1}{4}\gamma^2}$$

$$\omega_c = \sqrt{\frac{1}{2}\gamma^2 \pm \sqrt{\frac{1}{\rho^2}K^2\omega_l^4 - \omega_l^4 + \frac{1}{4}\gamma^2}}$$

Make substitutions back in for γ,

$$\omega_c = \sqrt{\frac{1}{2}\left(2\omega_l^2\left(2\zeta^2 - 1\right)\right)^2 + \sqrt{\frac{1}{\rho^2}K^2\omega_l^4 - \omega_l^4 + \frac{1}{4}\left(2\omega_l^2\left(2\zeta^2 - 1\right)\right)^2}}$$

$$\omega_c = \sqrt{\sqrt{\frac{1}{\rho^2}K^2\omega_l^4 - \omega_l^4}}$$

$$\omega_c = \left(\frac{1}{\rho^2}K^2\omega_l^4 - \omega_l^4\right)^{1/4}$$

B.2 Second Order High-pass System Properties

Laplace Representation

$$G_h(s) = \frac{Ks^2}{s^2 + 2\zeta\omega_h s + \omega_h^2}$$

System Magnitude

Let $\alpha = \omega_h^2$ and $\beta = 2\zeta\omega_h$,

$$G_h(s) = \frac{Ks^2}{s^2 + \beta s + \alpha}$$

Substitute $s = j\omega$,

$$G_h(j\omega) = \frac{K\left(j\omega\right)^2}{\left(j\omega\right)^2 + \left(j\omega\right)\beta + \alpha}$$

$$G_h(j\omega) = \frac{-\omega^2}{-\omega^2 + j\beta\omega + \alpha}$$

Now, find the magnitude by taking the magnitude of the top and bottom separately

$$
\begin{aligned}
|G_l(j\omega)| &= \frac{\left|-K\omega^2\right|}{\left|-\omega^2 + j\beta\omega + \alpha\right|} \\
&= \frac{K\omega^2}{\sqrt{(\alpha - \omega^2)^2 + (\beta\omega)^2}} \\
&= \frac{\omega^2}{\sqrt{(\alpha - \omega^2)(\alpha - \omega^2) + \beta^2\omega^2}} \\
&= \frac{\omega^2}{\sqrt{\omega^4 - 2\alpha\omega^2 + \alpha^2 + \beta^2\omega^2}} \\
&= \frac{\omega^2}{\sqrt{\omega^4 + (\beta^2 - 2\alpha)\omega^2 + \alpha^2}}
\end{aligned}
$$

Substitute α and β back into equations

$$
|G_h(j\omega)| = \frac{K\omega^2}{\sqrt{\omega^4 + \left((2\zeta\omega_h)^2 - 2\left(\omega_h^2\right)\right)\omega^2 + \left(\omega_h^2\right)^2}}
$$

$$
|G_h(j\omega)| = \frac{K\omega^2}{\sqrt{\omega^4 + 2\omega_h^2\left(2\zeta^2 - 1\right)\omega^2 + \omega_h^4}}
$$

Finding the magnitude squared yields

$$
|G_h(j\omega)|^2 = \frac{K^2\omega^4}{\omega^4 + 2\omega_h^2\left(2\zeta^2 - 1\right)\omega^2 + \omega_h^4}
$$

If $\zeta = \frac{1}{\sqrt{2}}$,

$$
|G_l(j\omega)|^2 = \frac{K^2\omega^4}{\omega^4 + \omega_h^4}
$$

Cutoff Frequency

To find the cut-off frequency at the value ρ, let $\gamma = 2\omega_l^2 \left(2\zeta^2 - 1\right)$ for convenience. Then,

$$\rho = \frac{K\omega_c^2}{\sqrt{\omega_c^4 + \gamma\omega_c^2 + \omega_h^4}}$$

$$\sqrt{\omega_c^4 + \gamma\omega_c^2 + \omega_h^4} = \frac{1}{\rho}K\omega_c^2$$

$$\omega_c^4 + \gamma\omega_c^2 + \omega_h^4 = \left(\frac{1}{\rho}K\omega_c^2\right)^2$$

$$\omega_c^4 + \gamma\omega_c^2 + \omega_h^4 = \frac{1}{\rho^2}K^2\omega_c^4$$

Let $\kappa = \frac{1}{\rho^2}K^2$

$$\omega_c^4 + \gamma\omega_c^2 + \omega_h^4 = \kappa\omega_c^4$$

$$\omega_c^4 - \kappa\omega_c^4 + \gamma\omega_c^2 + \omega_h^4 = 0$$

$$\omega_c^4\left(1 - \kappa\right) + \gamma\omega_c^2 + \omega_h^4 = 0$$

$$\omega_c^4 + \frac{\gamma\omega_c^2}{\left(1 - \kappa\right)} + \frac{\omega_h^4}{\left(1 - \kappa\right)} = 0$$

Let $\zeta = \frac{\omega_h^4}{\left(1-\kappa\right)}$, and $\Omega = \frac{\gamma}{\left(1-\kappa\right)}$

$$\omega_c^4 + \Omega\omega_c^2 + \zeta = 0$$

$$\omega_c^4 + \Omega\omega_c^2 + \frac{1}{4}\Omega^2 = \frac{1}{4}\Omega^2 - \zeta$$

$$\left(\omega_c^2 + \frac{1}{2}\Omega\right)^2 = \frac{1}{4}\Omega^2 - \zeta$$

$$\omega_c^2 + \frac{1}{2}\Omega = \sqrt{\frac{1}{4}\Omega^2 - \zeta}$$

$$\omega_c^2 = \sqrt{\frac{1}{4}\Omega^2 - \zeta} - \frac{1}{2}\Omega$$

$$\omega_c = \sqrt{\sqrt{\frac{1}{4}\Omega^2 - \zeta} - \frac{1}{2}\Omega}$$

Now substitute back in all variables

$$\omega_c = \sqrt{\sqrt{\zeta + \frac{1}{4}\Omega^2} - \frac{1}{2}\Omega}$$

$$\omega_c = \sqrt{\sqrt{\frac{\omega_h^4}{(1-\kappa)} + \frac{1}{4}\left(\frac{2\omega_h^2\left(2\zeta^2-1\right)}{(1-\kappa)}\right)^2} - \frac{1}{2}\left(\frac{2\omega_h^2\left(2\zeta^2-1\right)}{(1-\kappa)}\right)}$$

$$\omega_c = \left(\frac{\omega_h^4}{(1-\kappa)}\right)^{1/4}$$

$$\omega_c = \left(\frac{\omega_h^4}{\left(1 - \frac{1}{\rho^2}K^2\right)}\right)^{1/4}$$

$$\omega_c = \omega_h\left(1 - \frac{1}{\rho^2}K^2\right)^{-1/4}$$

B.3   Band-pass Filter Properties

Laplace Representation

Using the following property of magnitudes

$$G(s) = K \cdot G_l(s) \cdot G_h(s)$$

$$= K\frac{\omega_l^2}{s^2 + 2\zeta\omega_l s + \omega_l^2}\frac{s^2}{s^2 + 2\zeta\omega_h s + \omega_h^2}$$

$$= \frac{K\omega_l^2 s^2}{\left(s^2 + 2\zeta\omega_l s + \omega_l^2\right)\left(s^2 + 2\zeta\omega_h s + \omega_h^2\right)}$$

$$= \frac{K\omega_l^2 s^2}{s^4 + 2\omega_h\zeta s^3 + 2\omega_l\zeta s^3 + \omega_h^2 s^2 + 4\omega_h\omega_l\zeta^2 s^2 + \omega_l^2 s^2 + 2\omega_h^2\omega_l s + 2\omega_h\omega_l^2 s + \omega_h^2\omega_l^2}$$

$$= \frac{K\omega_l^2 s^2}{s^4 + \left(2\omega_h\zeta + 2\omega_l\zeta\right)s^3 + \left(\omega_h^2 + 4\omega_h\omega_l\zeta^2 + \omega_l^2\right)s^2 + \left(2\omega_h^2\omega_l + 2\omega_h\omega_l^2\right)s + \omega_h^2\omega_l^2}$$

Make the following substitutions

$$a_1 = 2\omega_h\zeta + 2\omega_l\zeta$$

$$a_2 = \omega_h^2 + 4\omega_h\omega_l\zeta^2 + \omega_l^2$$

$$a_3 = 2\omega_h^2\omega_l + 2\omega_h\omega_l^2$$

$$a_4 = \omega_h^2\omega_l^2$$

$$b_2 = \omega_l^2$$

Then,

$$G(s) = \frac{Kb^2s^2}{s^4 + a_1s^3 + a_2s^2 + a_3s + a_4}$$

System Magnitude

$$|G(s)| = |K \cdot G_l(s) \cdot G_h(s)| = |K| \cdot |G_l(s)| \cdot |G_h(s)|$$

Substituting $s = j\omega$

$$|G(j\omega)| = |K \cdot G_l(j\omega) \cdot G_h(j\omega)| = |K| \cdot |G_l(j\omega)| \cdot |G_h(j\omega)|$$

Substituting solutions from Section B.1 and B.2

$$|G(j\omega)| = K\frac{\omega_l^2}{\sqrt{\omega^4 + 2\omega_l^2(2\zeta^2 - 1)\omega^2 + \omega_l^4}} \frac{\omega^2}{\sqrt{\omega^4 + 2\omega_h^2(2\zeta^2 - 1)\omega^2 + \omega_h^4}}$$

$$= \frac{K\omega_l^2\omega^2}{\sqrt{\left(\omega^4 + 2\omega_l^2(2\zeta^2 - 1)\omega^2 + \omega_l^4\right)\left(\omega^4 + 2\omega_h^2(2\zeta^2 - 1)\omega^2 + \omega_h^4\right)}}$$

Let $\zeta = \frac{1}{\sqrt{2}}$

$$|G(j\omega)| = \frac{K\omega_l^2\omega^2}{\sqrt{\left(\omega^4 + \omega_l^4\right)\left(\omega^4 + \omega_h^4\right)}}$$

Which yields a magnitude squared of

$$|G(j\omega)|^2 = \frac{K^2\omega_l^4\omega^4}{\left(\omega^4 + \omega_l^4\right)\left(\omega^4 + \omega_h^4\right)}$$

Peak of Band-pass Filter

The peak of the band-pass filter is at the intersection of the low-pass filter and high pass filter. Let $\gamma_l = 2\omega_l^2\left(2\zeta^2 - 1\right)$

$$f_{\text{intersect}} = \frac{K\omega_l^2}{\sqrt{\omega_c^4 + \gamma_l\omega_c^2 + \omega_l^4}}$$

High pass filter. Let $\gamma_h = 2\omega_h^2\left(2\zeta^2 - 1\right)$

$$f_{\text{intersect}} = \frac{K\omega_c^2}{\sqrt{\omega_c^4 + \gamma_h\omega_c^2 + \omega_h^4}}$$

Calculate intersection point

$$\frac{K\omega_l^2}{\sqrt{\omega_c^4 + \gamma_l\omega_c^2 + \omega_l^4}} = \frac{K\omega_c^2}{\sqrt{\omega_c^4 + \gamma_h\omega_c^2 + \omega_h^4}}$$

$$\frac{\left(\omega_l^2\right)^2}{\omega_c^4 + \gamma_l\omega_c^2 + \omega_l^4} = \frac{\left(\omega_c^2\right)^2}{\omega_c^4 + \gamma_h\omega_c^2 + \omega_h^4}$$

Let $\alpha_l = \omega_l^4$, and $\alpha_2 = \omega_h^4$

$$\frac{\alpha_l}{\omega_c^4 + \gamma_l \omega_c^2 + \omega_l^4} = \frac{\omega_c^4}{\omega_c^4 + \gamma_h \omega_c^2 + \alpha_2}$$

$$\alpha_l \left(\omega_c^4 + \gamma_h \omega_c^2 + \alpha_2\right) = \omega_c^4 \left(\omega_c^4 + \gamma_l \omega_c^2 + \alpha_2\right)$$

$$\alpha_l \omega_c^4 + \alpha_l \gamma_h \omega_c^2 + \alpha_l \alpha_2 = \omega_c^8 + \gamma_l \omega_c^6 + \alpha_2 \omega_c^4$$

$$\omega_c^8 + \gamma_l \omega_c^6 + \alpha_2 \omega_c^4 - \alpha_l \omega_c^4 - \alpha_l \gamma_h \omega_c^2 = \alpha_l \alpha_2$$

$$\omega_c^8 + \gamma_l \omega_c^6 + \left(\alpha_2 - \alpha_l\right) \omega_c^4 - \alpha_l \gamma_h \omega_c^2 = \alpha_l \alpha_2$$

let $\xi = (a_2 - a_1)$, $\kappa = \alpha_l \gamma_h$, and $\phi = \alpha_1 \alpha_2$

$$\omega_c^8 + \gamma_l \omega_c^6 + \left(\alpha_2 - \alpha_l\right) \omega_c^4 - \alpha_l \gamma_h \omega_c^2 = \alpha_l \alpha_2$$

$$\omega_c^8 + \gamma_l \omega_c^6 + \xi \omega_c^4 - \kappa \omega_c^2 = \phi$$

The solution to ω_c is an eighth order polynomial with a numeric solution, but it does not appear to have a trivial algebraic solution. An alternative method to find the intersecting frequency of the low-pass filter and high-pass filter is to leverage the symmetry of the system. The intersection of the two filters in the logarithmic domain is the logarithmic midpoint of the two cut-off frequencies of the bode plot as seen in Figure B.1.
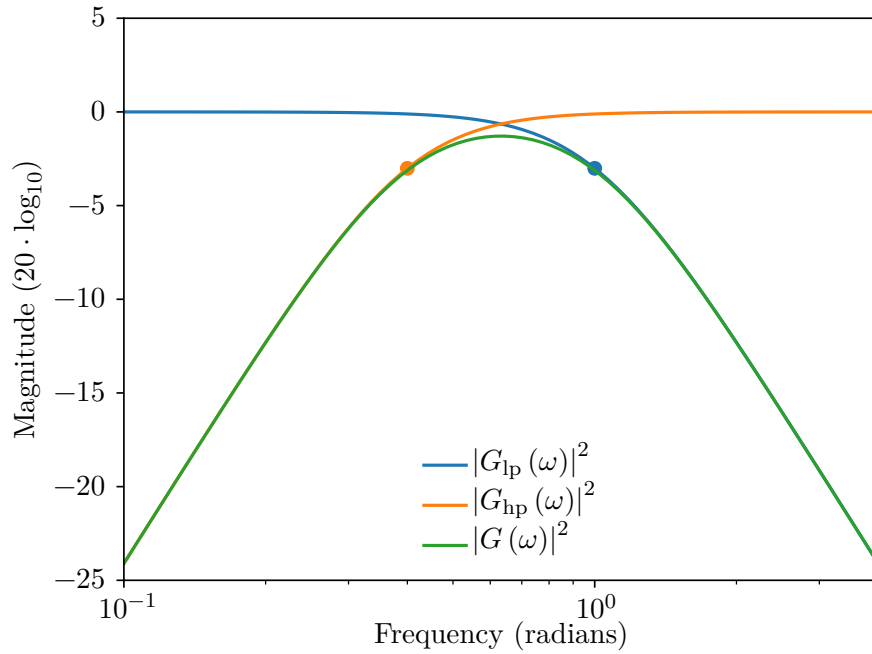
Fig. B.1: Depiction that the logrithmic midpoint between ω_l and ω_h is the ineterection frequency.

The graphical midpoint of a bode-plot can be calculated as

$$
\begin{aligned}
\text{midpoint} &= 10^{\frac{\log_{10}(a) + \log_{10}(b)}{2}} \\
&= 10^{\frac{1}{2} \log_{10}(a)} \cdot 10^{\frac{1}{2} \log_{10}(b)} \\
&= 10^{\log_{10}\left(a^{\frac{1}{2}}\right)} \cdot 10^{\log_{10}\left(b^{\frac{1}{2}}\right)} \\
&= a^{\frac{1}{2}} \cdot b^{\frac{1}{2}} \\
&= \sqrt{ab}
\end{aligned}
$$

where a is the high-pass filter cut-off frequency and b is the low-pass filter cut-off frequency. Therefore the intersecting frequency is located at

$$
\omega_{\text{intersect}} = \sqrt{\omega_l \omega_h}
$$

and the maximum value of the band-pass filter with $\zeta = \frac{1}{\sqrt{2}}$ is

$$
|G(j\omega)|^2_{\max} = |G(\omega_{\text{intersect}})|^2
$$

$$
= \frac{K^2\omega_l^4 \left(\left(\omega_l\omega_h\right)^{1/2}\right)^4}{\left(\left(\left(\omega_l\omega_h\right)^{1/2}\right)^4 + \omega_l^4\right)\left(\left(\left(\omega_l\omega_h\right)^{1/2}\right)^4 + \omega_h^4\right)}
$$

$$
= \frac{K^2\left(\omega_l^2\omega_h^2\right)\omega_l^4}{\left(\omega_l^2\omega_h^2 + \omega_l^4\right)\left(\omega_l^2\omega_h^2 + \omega_h^4\right)}
$$

$$
= \frac{K^2\left(\omega_l^2\omega_h^2\right)\omega_l^4}{\omega_l^4\omega_h^4 + \omega_l^2\omega_h^2\omega_h^4 + \omega_l^2\omega_h^2\omega_l^4 + \omega_l^4\omega_h^4}
$$

$$
= \frac{K^2\left(\omega_l^2\omega_h^2\right)\omega_l^4}{\omega_l^2\omega_h^2\left(\omega_l^2\omega_h^2 + \omega_h^4 + \omega_l^4 + \omega_l^2\omega_h^2\right)}
$$

$$
= \frac{K^2\omega_l^4}{\omega_h^4 + 2\omega_l^2\omega_h^2 + \omega_l^4}
$$

$$
= \frac{K^2\omega_l^4}{\left(\omega_h^2 + \omega_l^2\right)^2}
$$

System Cut-off frequency

To find the cut-off frequency at the value ρ, let $\zeta = \frac{1}{\sqrt{2}}$. Then,

$$|G(j\omega)| = \frac{K\omega_l^2\omega^2}{\sqrt{\left(\omega^4 + \omega_l^4\right)\left(\omega^4 + \omega_h^4\right)}}$$

$$\rho = \frac{K\omega_l^2\omega_c^2}{\sqrt{\left(\omega_c^4 + \omega_l^4\right)\left(\omega_c^4 + \omega_h^4\right)}}$$

$$\rho^2 = \frac{\left(K\omega_l^2\omega_c^2\right)^2}{\left(\omega_c^4 + \omega_l^4\right)\left(\omega_c^4 + \omega_h^4\right)}$$

$$\rho^2 = \frac{K^2\omega_l^4\omega_c^4}{\omega_c^8 + \omega_h^4\omega_c^4 + \omega_l^4\omega_c^4 + \omega_l^4\omega_h^4}$$

$$\rho^2 = \frac{K^2\omega_l^4\omega_c^4}{\omega_c^8 + \left(\omega_h^4 + \omega_l^4\right)\omega_c^4 + \omega_l^4\omega_h^4}$$

$$\omega_c^8 + \left(\omega_h^4 + \omega_l^4\right)\omega_c^4 + \omega_l^4\omega_h^4 = \frac{1}{\rho^2}K^2\omega_l^4\omega_c^4$$

$$\omega_c^8 + \left(\omega_h^4 + \omega_l^4\right)\omega_c^4 - \frac{1}{\rho^2}K^2\omega_l^4\omega_c^4 = -\omega_l^4\omega_h^4$$

$$\omega_c^8 + \left(\omega_h^4 + \omega_l^4 - \frac{1}{\rho^2}K^2\omega_l^4\right)\omega_c^4 = -\omega_l^4\omega_h^4$$

Let $\alpha = \omega_h^4 + \omega_l^4 - \frac{1}{\rho}K^2\omega_l^4$, and $\beta = \omega_l^4\omega_h^4$

$$\omega_c^8 + \alpha\omega_c^4 + \beta = 0$$

Completing the square

$$\omega_c^8 + \alpha\omega_c^4 = -\beta$$

$$\omega_c^8 + \alpha\omega_c^4 + \frac{1}{4}\alpha^2 = \frac{1}{4}\alpha^2 - \beta$$

$$\left(\omega_c^4 + \frac{1}{2}\alpha\right)^2 = \frac{1}{4}\alpha^2 - \beta$$

$$\omega_c^4 = \sqrt{\frac{1}{4}\alpha^2 - \beta} - \frac{1}{2}\alpha$$

$$\omega_c = \left(\sqrt{\frac{1}{4}\alpha^2 - \beta} - \frac{1}{2}\alpha\right)^{1/4}$$

Note that $K = \frac{(\omega_h^2 + \omega_l^2)}{\omega_l^2}$ in order to scale the band-pass filter to 0dB before finding the cut-off frequency.

Solving for ω_l and ω_h given a -3dB cut-off frequency

With a given $\omega_h = \kappa\omega_l$ and $K = \frac{(\omega_h^2 + \omega_l^2)}{\omega_l^2}$. K is set to scale the system up to 0dB

$$|G(j\omega)| = \frac{K\omega_l^2\omega^2}{\sqrt{\left(\omega^4 + \omega_l^4\right)\left(\omega^4 + \omega_h^4\right)}}$$

$$\rho = \frac{\frac{(\omega_h^2 + \omega_l^2)}{\omega_l^2}\omega_l^2\omega_c^2}{\sqrt{\left(\omega_c^4 + \omega_l^4\right)\left(\omega_c^4 + \omega_h^4\right)}}$$

$$\rho^2 = \frac{\left(\left(\omega_h^2 + \omega_l^2\right)\omega_c^2\right)^2}{\left(\omega_c^4 + \omega_l^4\right)\left(\omega_c^4 + \omega_h^4\right)}$$

$$\rho^2 = \frac{\left(\left(\kappa^2\omega_l^2 + \omega_l^2\right)\omega_c^2\right)^2}{\left(\omega_c^4 + \omega_l^4\right)\left(\omega_c^4 + \omega_h^4\right)}$$

$$\rho^2 = \frac{\left(\omega_c^2\left(\kappa^2 + 1\right)\omega_l^2\right)^2}{\left(\omega_c^4 + \omega_l^4\right)\left(\omega_c^4 + \omega_h^4\right)}$$

$$\rho^2 = \frac{\omega_c^4\left(\kappa^2 + 1\right)^2\omega_l^4}{\omega_c^8 + \kappa^4\omega_l^4\omega_c^4 + \omega_l^4\omega_c^4 + \omega_l^4\kappa^4\omega_l^4}$$

$$\rho^2\left(\omega_c^8 + \kappa^4\omega_l^4\omega_c^4 + \omega_l^4\omega_c^4 + \omega_l^4\kappa^4\omega_l^4\right) = \omega_c^4\left(\kappa^2 + 1\right)^2\omega_l^4$$

$$\omega_c^8 + \kappa^4\omega_l^4\omega_c^4 + \omega_l^4\omega_c^4 + \omega_l^4\kappa^4\omega_l^4 = \frac{\omega_c^4\left(\kappa^2 + 1\right)^2}{\rho^2}\omega_l^4$$

$$\omega_c^8 + \left(\kappa^4\omega_c^4\right)\omega_l^4 + \left(\omega_c^4\right)\omega_l^4 + \kappa^4\omega_l^8 = \frac{\omega_c^4\left(\kappa^2 + 1\right)^2}{\rho^2}\omega_l^4$$

$$\left(\kappa^4\omega_c^4 + \omega_c^4 - \frac{\omega_c^4\left(\kappa^2 + 1\right)^2}{\rho^2}\right)\omega_l^4 + \kappa^4\omega_l^8 = -\omega_c^8$$

$$\kappa^4\omega_l^8 + \omega_c^4\left(\kappa^4 + 1 - \frac{\left(\kappa^2 + 1\right)^2}{\rho^2}\right)\omega_l^4 = -\omega_c^8$$

$$\omega_l^8 + \omega_c^4\left(1 + \frac{1}{\kappa^4} - \frac{\left(\kappa^2 + 1\right)^2}{\kappa^4\rho^2}\right)\omega_l^4 = -\frac{\omega_c^8}{\kappa^4}$$

Let $\Omega = \omega_c^4 \left(1 + \frac{1}{\kappa^4} - \frac{(\kappa^2+1)^2}{\kappa^4 \rho^2}\right)$, then

$$\omega_l^8 + \Omega \omega_l^4 = -\frac{\omega_c^8}{\kappa^4}$$

$$\omega_l^8 + \Omega \omega_l^4 + \frac{1}{4}\Omega^2 = -\frac{\omega_c^8}{\kappa^4} + \frac{1}{4}\Omega^2$$

$$\left(\omega_l^4 + \frac{1}{2}\Omega\right)^2 = -\frac{\omega_c^8}{\kappa^4} + \frac{1}{4}\Omega^2$$

$$\omega_l^4 + \frac{1}{2}\Omega = -\sqrt{-\frac{\omega_c^8}{\kappa^4} + \frac{1}{4}\Omega^2}$$

$$\omega_l^4 = -\sqrt{-\frac{\omega_c^8}{\kappa^4} + \frac{1}{4}\Omega^2} - \frac{1}{2}\Omega$$

$$\omega_l = \left(-\sqrt{-\frac{\omega_c^8}{\kappa^4} + \frac{1}{4}\Omega^2} - \frac{1}{2}\Omega\right)^{1/4}$$

B.4 Double Integrated Band-pass Filter

Laplace Representation

Using the following property of magnitudes

$$G(s) = K \cdot G_l(s) \cdot G_h(s) \cdot G_i(s)$$

$$= K\frac{\omega_l^2}{s^2 + 2\zeta\omega_l s + \omega_l^2}\frac{s^2}{s^2 + 2\zeta\omega_h s + \omega_h^2} \cdot \frac{1}{s^2}$$

$$= \frac{K\omega_l^2}{\left(s^2 + 2\zeta\omega_l s + \omega_l^2\right)\left(s^2 + 2\zeta\omega_h s + \omega_h^2\right)}$$

$$= \frac{K\omega_l^2}{s^4 + 2\omega_h\zeta s^3 + 2\omega_l\zeta s^3 + \omega_h^2 s^2 + 4\omega_h\omega_l\zeta^2 s^2 + \omega_l^2 s^2 + 2\omega_h^2\omega_l s + 2\omega_h\omega_l^2 s + \omega_h^2\omega_l^2}$$

$$= \frac{K\omega_l^2}{s^4 + \left(2\omega_h\zeta + 2\omega_l\zeta\right)s^3 + \left(\omega_h^2 + 4\omega_h\omega_l\zeta^2 + \omega_l^2\right)s^2 + \left(2\omega_h^2\omega_l + 2\omega_h\omega_l^2\right)s + \omega_h^2\omega_l^2}$$

Make the following substitutions

$$a_1 = 2\omega_h\zeta + 2\omega_l\zeta$$

$$a_2 = \omega_h^2 + 4\omega_h\omega_l\zeta^2 + \omega_l^2$$

$$a_3 = 2\omega_h^2\omega_l + 2\omega_h\omega_l^2$$

$$a_4 = \omega_h^2\omega_l^2$$

$$b = \omega_l^2$$

Then,

$$G(s) = \frac{Kb}{s^4 + a_1 s^3 + a_2 s^2 + a_3 s + a_4}$$

System Magnitude

First identifying the magnitude of the integrator

$$\left|\frac{1}{s^2}\right| = \frac{1}{\omega^2}$$

Using the following property of magnitudes

$$|H(j\omega)| = |G(j\omega)|\left|\frac{1}{(j\omega)}\right|$$

$$= |G(j\omega)|\frac{1}{\omega^2}$$

Substituting $G(j\omega)$ magnitude from Section B.3

$$|H(j\omega)| = \frac{K\omega_l^2\omega^2}{\sqrt{\left(\omega^4 + 2\omega_l^2\left(2\zeta^2 - 1\right)\omega^2 + \omega_l^4\right)\left(\omega^4 + 2\omega_h^2\left(2\zeta^2 - 1\right)\omega^2 + \omega_h^4\right)}}\frac{1}{\omega^2}$$

$$|H(j\omega)| = \frac{K\omega_l^2}{\sqrt{\left(\omega^4 + 2\omega_l^2\left(2\zeta^2 - 1\right)\omega^2 + \omega_l^4\right)\left(\omega^4 + 2\omega_h^2\left(2\zeta^2 - 1\right)\omega^2 + \omega_h^4\right)}}$$

Which yields a magnitude squared of

$$|H(j\omega)|^2 = \frac{\left(K\omega_l^2\right)^2}{\left(\omega^4 + 2\omega_l^2\left(2\zeta^2 - 1\right)\omega^2 + \omega_l^4\right)\left(\omega^4 + 2\omega_h^2\left(2\zeta^2 - 1\right)\omega^2 + \omega_h^4\right)}$$

$$|H(j\omega)|^2 = \frac{K^2\omega_l^4}{\left(\omega^4 + 2\omega_l^2\left(2\zeta^2 - 1\right)\omega^2 + \omega_l^4\right)\left(\omega^4 + 2\omega_h^2\left(2\zeta^2 - 1\right)\omega^2 + \omega_h^4\right)}$$

Recall that $\zeta = \frac{1}{\sqrt{2}}$, so

$$|H(j\omega)|^2 = \frac{K^2\omega_l^4}{\left(\omega^4 + \omega_l^4\right)\left(\omega^4 + \omega_h^4\right)}$$